

Occurrence, release and alteration of chromite nanoparticles

by

Neal McClenaghan

A thesis submitted in partial fulfillment of
the requirements for the degree of
Master of Science (MSc) in Geology

The Faculty of Graduate Studies
Laurentian University
Sudbury, Ontario, Canada

© Neal McClenaghan, 2020

THESIS DEFENCE COMMITTEE/COMITÉ DE SOUTENANCE DE THÈSE
Laurentian University/Université Laurentienne
Office of Graduate Studies/Bureau des études supérieures

Title of Thesis Titre de la thèse	Occurrence, release and alteration of chromite nanoparticles		
Name of Candidate Nom du candidat	McClenaghan, Neal		
Degree Diplôme	Master of Science		
Department/Program Département/Programme	Geology	Date of Defence Date de la soutenance	April 29, 2021

APPROVED/APPROUVÉ

Thesis Examiners/Examineurs de thèse:

Dr. Graeme Spiers
(Co-Supervisor/Co-directeur(trice) de thèse)

Dr. Michael Schindler
(Co-Supervisor/Co-directeur(trice) de thèse)

Dr. Joy Gray-Munro
(Committee member/Membre du comité)

Dr. Dogan Paktunc
(External Examiner/Examineur externe)

Approved for the Office of Graduate Studies
Approuvé pour le Bureau des études supérieures
Tammy Eger, PhD
Vice-President, Research (Office of Graduate Studies)
Vice-rectrice à la recherche (Bureau des études supérieures)

ACCESSIBILITY CLAUSE AND PERMISSION TO USE

I, **Neal McClenaghan**, hereby grant to Laurentian University and/or its agents the non-exclusive license to archive and make accessible my thesis, dissertation, or project report in whole or in part in all forms of media, now or for the duration of my copyright ownership. I retain all other ownership rights to the copyright of the thesis, dissertation or project report. I also reserve the right to use in future works (such as articles or books) all or part of this thesis, dissertation, or project report. I further agree that permission for copying of this thesis in any manner, in whole or in part, for scholarly purposes may be granted by the professor or professors who supervised my thesis work or, in their absence, by the Head of the Department in which my thesis work was done. It is understood that any copying or publication or use of this thesis or parts thereof for financial gain shall not be allowed without my written permission. It is also understood that this copy is being made available in this form by the authority of the copyright owner solely for the purpose of private study and research and may not be copied or reproduced except as permitted by the copyright laws without written authority from the copyright owner.

Abstract

Many environmental risk assessments are based on the total concentration of elements in natural waters/ soils, ignoring that a significant proportion of elements is associated with nanoparticles. TEM analysis of the silicate minerals from a chromitite sample from the Mum and Alice June claims, California confirmed that Cr-rich silicates contained an abundance of chromite nanoparticles. Subsequently, the colloidal fraction of a Cr-rich silicate leaching experiment revealed that the chromite nanoparticles persist through the weathering of their host silicate, confirming that chromite nanoparticles can be a significant form of Cr in the environment. The oxidation of chromite nanoparticles in the presence of Mn-oxides (best known environmental oxidiser of Cr³⁺) was tested with 6 batch experiments at pH 5 over a 9-month period. These experiments reveal that the dominant redox reaction between chromite nanoparticles and Mn-oxides is the oxidation of Fe²⁺ (rather than Cr³⁺) by Mn³⁺.

Keywords: Chromite, Hausmannite, Chamosite, Clinocllore, Colloid, Nanoparticles, Transmission Electron Microscopy, Aggregation, Adsorption

Co-Authorship statement

Chapter 1 of this thesis is meant to provide background information of the main topics discussed in this study. It includes past and current literature and an introduction into the mineral instrumental technique used in this study. Micheal Schindler assisted with the outline and offered edits, however I am the sole author of this chapter. I am the first author of chapter 2 and Micheal Schindler is the second author. Furthermore, a shorter version of chapter 2 was created and submitted to American mineralogist and can be found in appendix B.

Acknowledgements

I would like to start by thanking my supervisor, Dr Schindler, for his constant support and guidance. I experience many new challenges researching concepts in chemistry and nanoscience I was unfamiliar with, your patience and support were greatly appreciated. I also want to thank you for the level of enthusiasm you always had for this project as it helped not only increase my own appreciation for the project but it increased my appreciation for all the processes capable of occurring on the nanoscale.

I would like to thank my committee members Dr Spiers and Dr Gray-Munro. I appreciate the many insights you have provided me, as well as helping me acquire all the necessary materials to conduct my research. I would also like to thank Paul Guerin and Dr Jugo for their assistance with the synthesis of the chromite nanoparticle, Abdul Khan at the Manitoba Institute of Materials for his assistance with the TEM studies and the MECP laboratories in Etobicoke and especially Teresa Switzer and Tadesse Godeto for their assistance with chemical analysis.

Finally, I would like to thank all of my outstanding family and friends. Every single one of you has never stopped supporting me and has always encouraged me to reach my goals.

Table of Contents

Thesis Defense Committee	ii
Abstract	iii
Co-authorship statement	iv
Acknowledgements	v
Table of Contents	vi
List of Abbreviations	ix
Chapter 1	1
1.1 Cr in the environment	1
1.1.1 sources of Cr in the environment.....	1
<i>1.1.1.1 Anthropogenic source</i>	1
<i>1.1.1.2 Natural sources</i>	2
1.1.2 Cr mineralogy and behavior in soils and water	3
1.2 Nanoparticles in the environment.....	4
1.2.1 Unique properties of nanoparticles.....	4
1.2.2 Transport and aggregation of nanoparticles.....	5
1.3 Transmission electron microscopy	7
1.3.1 Electron imaging.....	8
1.3.2 STEM, CTEM, AEM.....	9
1.3.3 Scattering and diffraction.....	11
References	18
Chapter 2	22
2.1 Introduction.....	23
2.1.1 Geochemical and mineralogical background information on the environmental fate of chromium and chromite in a low-T environment.....	24
2.1.2 Detailed objectives.....	28
2.2 Materials and methods.....	29

2.2.1 Leaching experiments of Cr-rich clinocllore powders from the Black Thor deposit	33
2.2.2 Reagents for the long-term batch experiments	34
2.2.3 Set up of the long-term batch experiments.....	36
2.2.4 Analysis of Cr in the solute and colloidal fractions after the batch experiments	37
2.2.5 Powder x-ray powder diffraction, x-ray fluorescence spectroscopy and loss of ignition	39
2.2.6 Preparation of TEM samples	39
2.2.7 Scanning electron microscopy and transmission electron microscopy.....	40
2.3 Results.....	41
2.3.1 Silicate hosted chromite nanoparticles in the chromite ore from the Mum and Alice June claims.....	41
2.3.2 Mineralogical features in the silicate-enriched fraction of the chromitite ore and leachate after the leaching experiment.....	43
2.3.3 Size and chemical composition of synthesized chromite nanoparticles.....	45
2.3.4 Chemical and mineralogical features of colloidal fraction in the suspensions after 6 months of the long-term batch experiments.....	47
2.3.5 Chemical trends among the nano- to micrometer-size particles.....	48
2.3.6 Textural, chemical and mineralogical features of chromite-hausmannite nanoparticle aggregates	49
2.3.7 Textural chemical and mineralogical features of secondary Cr-hydroxide phases	51
2.3.8 Interaction of chromite nanoparticles with chamosite and organic matter.....	54
2.3.9 chemical composition of suspensions after filtering.....	56
2.4 Discussion.....	58
2.4.1 Formation of chromite nanoparticles during greenschist metamorphism.....	58
2.4.2 Release of chromite nanoparticles during the weathering of Mg-silicates.....	60
2.4.3 Aggregation of nanoparticles and their attachment onto mineral surfaces.....	61
2.4.4 Dissolution reprecipitation processes on the surface of hausmannite	62
2.4.5 Reaction pathways during the interaction of hausmannite and chromite nanoparticles.	64
2.4.6 The composition of the suspensions after the long-term experiments.....	65

2.4.7 The formation of hexavalent.....	66
2.4.8 Recommendation for future studies on chromite nanoparticles in the presence of Mn-oxides.....	68
2.5 Implications.....	69
References.....	72
Appendix A.	81
Appendix B.	85

List of abbreviations

AEM	Analytical Electron Mycroscopy
CTEM	Convential Transmission Electron Mycroscopy
DLVO	Derjaguin-Landau-Verwey-Overbeak
DOM	Dissolved Organic Matter
EELS	Electron Energy Loss Spectroscopy
EDS	Energy Dispersive X-ray spectroscopy
EDTA	Ethylenediaminetetraacetic Acid
FFT	Fast Fourier Transformations
HAADF	High Angle Annular Dark Field
ICP-MS	Inductively Coupled-Plasma Mass Spectrometry
ICP-	Inductively Coupled-Plasma Optical Emission
OES	Spectrometry
LOI	Loss On Ignition
PCS	Pore Controled Solubility
ORP	Oxidation-Reduction Potential
SAED	Selected Area Electron Diffraction
SEM	Scanning Electron Microscopy
STEM	Scanning-Transmission Electron Microscopy
TEM	Transmission Electron Microscopy
UV-VIS	Ultraviolet-visible spectroscopy
XRD	X-ray Diffraction
XRF	X-ray Fluorescence

Chapter 1

1.1 Cr in the environment

Chromium's (Cr) atomic number is 24 and it belongs to the transition metal group in the periodic table. Chromium exist in four different stable isotopes (^{50}Cr , ^{52}Cr , ^{53}Cr , ^{54}Cr) with ^{52}Cr being the most abundant (83.789% abundance) and can exist in multiple oxidation states ranging from -2 to +6 (Choppala et al., 2013). However, Cr^{3+} and Cr^{6+} are the predominant oxidation states present in the environment. Cr^{3+} is non-toxic, many Cr^{3+} minerals are relatively insoluble and Craqueous species are relatively immobile. In contrast, Cr^{6+} is toxic and carcinogenic, many Cr^{6+} -bearing compounds are highly soluble and Cr^{6+} aqueous species are highly mobile (Fendorf, 1995, Oze et al., 2004; Salem et al., 1989).

1.1.1 Sources of Cr in the environment

Cr can enter the environment through naturally occurring and anthropogenic pathways, and is present in numerous environmental domains including surface water, groundwater, soil and sediment (Choppala et al., 2013).

1.1.1.1 Anthropogenic sources

Cr is a common contaminant in natural waters and soils and the ubiquitous occurrence of Cr in some natural systems is, in part, due to it's uses as an important industrial metal in a variety of diverse products and processes. Every year large quantities of Cr are mined and used for a variety of different applications including metallurgy, tanning of animal hides, inhibition of water corrosion, textile dyes and mordants, pigments, ceramic glazes, refractory bricks and pressure treated lumber (Olivera, 2012). It was estimated that, in 1993 over 170 000 tons of Cr

waste from these industries was discharged into the environment annually worldwide (Gadd and White, 1993). Cr can enter the atmosphere primarily as a result of burning fossil fuels, production of steel, stainless steel welding and Cr manufacturing (Guertin et al., 2004). Whereas anthropogenic emission to water and soils are primarily sourced from industrial processes such as electroplating, tanning, water treatment or disposal of coal ash (Guertin et al., 2004).

1.1.1.2 Natural sources

Cr is found throughout the environment including water, soil, air and biota. It has an estimated crustal abundance of 100 mgkg^{-1} , which makes it the 21st most abundant element in the earth's crust (Barnhart, 1997). On average the Cr concentration in the continental crust has been reported as being 125 mgkg^{-1} , and generally ranges from 80-200 mgkg^{-1} (NAS, 1974). The abundance of Cr in soils is, for the most part, dependent on parent materials. Granitic igneous, limestone and sandstones generally contain very low Cr levels (20 to 35 mgkg^{-1}), whereas Mafic to Ultramafic rocks contain, on average, the highest Cr levels with average concentrations of 220 mgkg^{-1} to 1800 mgkg^{-1} respectively. The higher Cr levels found in mafic and ultramafic rocks is primarily due to the extremely low solubility of Cr in mafic magmas because a lower solubility will result in the precipitation of Cr bearing phases (Cr-spinel and pyroxene) out of the melt at temperatures similar to other mafic minerals (such as olivine) (Shiraki, 1997). Serpentine soils are formed from the weathering of ultramafic rocks and their metamorphic derivatives and as such the highest Cr concentrations are found in serpentine soils and can reach levels as high as 80,600 mg kg^{-1} , whereas non serpentine soils generally range from 7 to 221 mgkg^{-1} (Oze et al., 2004).

1.1.2 Cr mineralogy and behavior in soils and waters

Cr can be incorporated into a wide variety of different minerals such as

Chromite (FeCr_2O_4), Eskolaite (Cr_2O_3), Bracewellite (CrOOH), Uvarovite ($\text{Ca}_2\text{Cr}_2(\text{SiO}_4)_2$), Crocoite (PbCrO_4), pyroxene ($\text{NaCrSi}_2\text{O}_6$) etc... (Liu et al., 2017). However, Chromite, Cr-bearing magnetite, pyroxenes, chlorites and serpentine group minerals have been cited as the primary source for Cr in ultramafic rocks and their metamorphic derivatives. Therefore, the release of Cr into natural waters and soils is controlled by the rate at which the previously listed minerals weather. Here, minerals of the chlorite and serpentine group are more susceptible to weathering than Cr-bearing oxides such as chromite and magnetite (Fandeur et al., 2009; Hseu and Iizuka 2013; Oze et al., 2004)

The speciation of Cr in soils is controlled by a combination of the geochemistry and biochemistry of the soil and water. The three most important reactions that affect the distribution of Cr in soil and water are oxidation-reduction, sorption-desorption and dissolution-precipitation. Under most natural conditions, Cr^{3+} is the most stable form of Cr in soil and water. Cr^{3+} adsorbs and is strongly retained onto soil particles, which in combination with the low solubility of Cr^{3+} -bearing minerals causes it to be very immobile and to depict a low bioavailability. In contrast, Cr^{6+} is a strong oxidant and is only stable at high redox potentials in the absence of any reducing agent (Choppala et al., 2013). Cr^{6+} is highly mobile in soils that are dominated by clay minerals, due to the repulsion between negative-charged chromate species and surfaces of clay particles under near neutral pH conditions (Choppala et al., 2013; Richard and Bourg, 1991).

1.2 Nanoparticles in the environment

Nanoparticles are nanometer sized (1-100nm) crystalline to amorphous solid particles.

Nanoparticles are found throughout Earth's chemical and physical chemical compartments, and the global transport of nanoparticles plays an important role in many inorganic and biological processes (Hochella et al., 2012). Nanoparticles depict variations in the atomic structure as a function of size relative to larger particles of the same material, which has an influence on their physical and chemical properties (Hochella et al., 2008). The impact of nanoparticles on processes in the interior and surface of the Earth are due, in part or in whole, to their unique properties.

1.2.1 Unique properties of nanoparticles

Nanoparticles frequently behave very different from materials on the bulk scale. In other words, the behavior of a nanoparticle cannot necessarily be predicted from the behavior of their larger counterparts on the bulk scale (Hochella et al., 2012). These variations in behavior are most likely due to changes in the atomic structure, surface topography, electronic structure, and crystal shape as a function of size in the nano size regime. As one can expect, changes in the properties of a particle will result in different chemical interactions between the particle and its surrounding environment. Redox reactions are a good example of the impact of size dependent behavior of nanoparticles as redox reactions are one of the fundamental reactions in the environment and display the magnitude at which their behavior on the nanoscale is affected (Hochella et al., 2008; Tratnyek and Macalady, 2000). For example, Madden and Hochella (2005) showed that 7 nm hematite ($\alpha\text{-Fe}_2\text{O}_3$) crystals catalyzed the oxidation of Mn^{2+} one to one and a half orders of magnitude faster than 37-nm hematite crystals.

Solubility can also be a size dependent property at the nanoscale, which is significant because mineral solubility is considered to be an essential property for predicting the stability of minerals and dissolved species. Size dependent solubility has been modeled with a modified version of the Kelvin equation for spherical particles (eq 1).

$$\frac{S}{S_0} = \exp \left[\frac{2\gamma\bar{V}}{RT r} \right] \quad (1)$$

- S: solubility of fine grains (mol/kg)
- S₀: solubility of bulk material (mol/kg)
- r: particle radius (m)
- V: molecular volume (m³/ mol)
- R: gas constant (mJ/mol K)
- T: temperature (K)
- γ: surface free energy (mJ/m²)

This equation shows that as the radius of the grain decreases, the solubility of that grain will increase exponentially relative to the measured solubility of the bulk material (Hochella, 2002).

1.2.2 Transport and aggregation of nanoparticles

Due to their high surface area to volume ratio, nanoparticles are easily and efficiently transported over long distances through fluvial, alluvial and aeolian processes (Hochella et al., 2005; Plathe et al. 2010). As they are so easily transported, nanoparticles contribute a significant

portion of the mass transport that occurs on earth. The sorption of metals and organics on to minerals surfaces is an important variable in determining how metals and organics are transported in the environment (Hochella et al., 2012). Nanoparticles, on a per mass basis, are calculated to sorb more metals and organics than larger particles. The combination of being easily transported and the ability of nanoparticles to sorb other molecules is what makes them so important to the global transport of mass.

Modern research on nanoparticle behavior indicates that their global transport will be significantly affected by their aggregation behavior. Aggregation occurs when physical processes cause nanoparticle surfaces to come into contact with each other and short-range thermodynamic interactions keep the particles attached (Hochella et al., 2012; Hotze et al., 2010). For particles in the nano size regime (<100nm), Brownian motion dominant force control the long-range interactions of individual particles and their collision. When collision occurs, the particles can either attached or be repelled. The forces that control these interactions have been explained with the DLVO theory (Hotze et al., 2010). According to the DLVO theory, two major parameters will dominate the interaction between particles: van der Waals attractive forces and the charge of electrostatic double layer. The charge created by the electrostatic double layer is heavily influence by the chemistry of the surrounding media. A low ionic strength increases the thickness of the double layer whereas a high ionic strength compresses the double layer (Hotze et al., 2010). When the attractive forces due to the Van der Waals forces are greater than the repulsive forces due to similar charges of the electric double layer, aggregation is favored.

In environments where nanoparticles are allowed to aggregate, they become far less mobile. For example, when rivers transport nanoparticles into the ocean the majority of nanoparticles aggregate and begin to settle. This phenomenon is a result of the mixing of

low ionic strength fresh water carrying nanoparticles with high ionic strength seawater water, which results in the decrease in thickness and charge of the electrostatic double layer and thus in a decrease in the repulsive forces between the particles (Hochella et al., 2012).

Crystal growth has long been believed to occur through the addition of individual monomers, however it is now recognized that crystallization can also occur through the addition of larger molecules such as nanoparticles (De Yoreo et al., 2015; Mirabello et al., 2020). There are a number of conditions that must be met for crystal growth via particle attachment (CPA): 1) a number of nanoparticles of similar chemistry must exist in the system 2) the sum of attractive and repulsive forces has to favor the aggregation of particles; 3) the resulting larger crystal has to have a lower surface free energy than that of the nanoparticles. As many particles that occur in the nano size regime are considered metastable, the process of crystal growth through particle attachment commonly increases the stability of the phases in the system (Caraballo et al., 2013; De Yoreo et al., 2015; Xu et al., 2010).

1.3 Transmission electron microscopy

TEMs comprise a variety of different instruments which all make use of the particle and wave like characteristics of electrons (Wave-particle duality) and have a variety of different uses (Kadin, 2018). TEM's take advantage of the very small Broglie wavelength of electrons, which allows the imaging of features on the nanometer scale and to record electron diffraction patterns at very small two-theta angles (see below).

These unique applications of TEMs make them a valuable tool in the study and characterization of environmental processes at the nanoscale.

1.3.1 Electron imaging

Electrons are a form of ionizing radiation, which has enough energy to detach electrons from the outer shell of an atom or molecule. One of the reasons that ionizing radiation is so useful is that it is capable of producing a variety of secondary signals such as backscattered electrons, secondary electrons and X-rays (Fig 1). Although these secondary signals can be used to obtain various chemical and structural information, the imaging of the sample with the direct beam of transmitted electrons is the primary use of TEMs. This is achieved through the use of a filament (often a tungsten filament or LaB₆ filament) in a vacuum chamber which emits electrons upon exposure to thermal energy (thermionic filament) or an electric field (field emission filament). When thermionic filaments are heated to a sufficient temperature the free electrons inside the filament acquire enough thermal energy to exceed the natural barrier (work function) that prevents them from escaping. Field emission filaments function by applying an intense electric field to the material which lowers the work function barrier enough for electrons to escape. Field emission filaments are produced with a fine tip giving them a much smaller source size. They also have very high current densities and brightness that when all combined means that the beam is very spatially coherent and has a small energy spread. Therefore, if the TEM requires a very bright coherent source then a field emission filament is the best option. However, a major drawback of a field emission filament is the small source size as it makes it difficult to illuminate larger areas of the sample without losing too much current density.

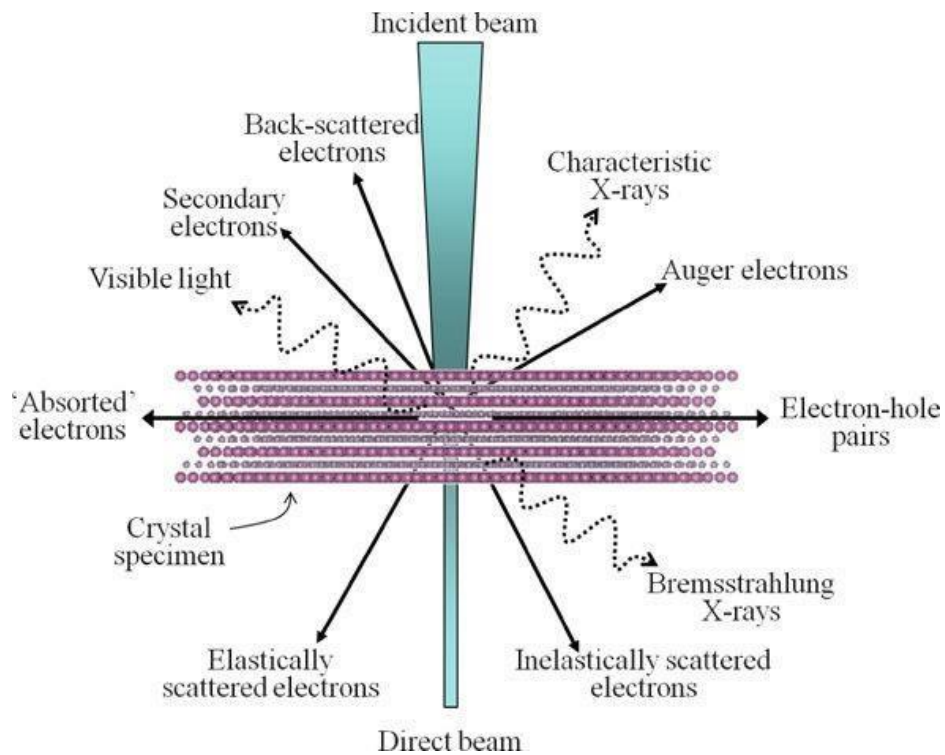


Figure 1: Signals generated when a high-energy beam of electrons interacts with a thin specimen. Most of these electron signals are detectable through the use of different TEMs. Reprinted from Semiconductor research: experimental techniques (p 25)

1.3.2 STEM, CTEM and AEM

There are multiple uses for electron beams and scattered electrons in microscopes. The most prevalent modes of operation used on a TEM are: conventional transmission electron microscopy (CTEM), scanning transmission electron microscopy (STEM), and analytical electron microscopy (AEM). CTEMs function by accelerating the emitted electrons through an electromagnetic field with electromagnetic lenses focusing the electrons into a narrow beam. The electron beam subsequently is transmitted through a sample with a thickness commonly below 100 nm. After being transmitted through the sample the electrons are detected by a phosphor screen, CCD or film and produce an image. The resulting image produced from the interaction of

the electron beam and the sample will reflect the electron density and thickness of the material. TEMs can produce images through bright field imaging or dark field imaging. In bright field imaging the electrons transmitted through the sample are collected, thus the areas with the highest electron density will appear the darkest. On the other hand, dark field imaging collects scattered electrons, Hence the areas with the greatest ability to scatter electrons (high electron density) will appear the brightest while the areas where there is no scattering will appear dark. When using STEM, the conventional electron beam is focused onto a fine spot and then the beam is scanned over the sample in a raster-based pattern and the various signal are collected and form an image (Rosenauer et al, 2014). AEM refers to the collecting of spectroscopic data from the numerous different signals generated from the incident electron beam (Botton, 2007). Most modern TEMS are equipped with all the necessary equipment to utilise all three methods (CTEM, STEM, AEM) and switch between them as needed. The main use of the STEM is to form what is known as Z-contrast images, which are images formed from mapping the intensity of high angle scattered electrons (Wang et al., 2013). The images created with Z-contrast are a map of the scattering ability of the atoms present in the sample. Because the images generated are formed from the high angle scattered electron from the atomic nuclei the results will be dependent on the atomic number (Z) squared. Other information that can be obtained with STEM are known as energy dispersive X-ray spectroscopy (EDS) and electron energy loss spectroscopy (EELS). Both of these techniques provide chemical data from the sample and are also classified as AEM techniques. EELS analysis functions by exposing a thin sample, of a known thickness, to a beam of electrons with a known range of kinetic energies, some of the electrons will be inelastically scattered at a slight angle to the incident beam (signifying that they have lost some energy). Quantifying the energy distribution of the electrons after interacting with the sample can

be used to gain information on a given area as the change in energy is related to the local environment of electrons that interacted with the incident beam. EDS relies on the fundamental principle that each element has a unique atomic structure which will give off unique x-ray peaks when the atoms are excited by the electron beam. EDS is initiated by the bombardment of the sample with electrons where incident electrons can excite inner shell electron which results in their ejections and the filling of the resulting vacancies by outer shell electrons. As electrons are moving from a higher energy to a lower energy shell, the difference in energy between these two shells will be released as characteristic X-rays. The emitted characteristic X-rays have an energy that is unique to the element it originated from and specific electron transition from an outer shell to an inner shell. The intensity of characteristic X-rays can then be measured and the TEM operator can determine which elements are present in the sample.

1.3.3 Scattering and diffraction

Electron scattering is a fundamental process in electron microscopy. No electron image of the sample can form if no electrons are scattered by the sample and any non scattering object would be invisible under a TEM (Williams and Carter, 1996). Electrons that do not deviate far from the incident beam are of greatest interest in TEM as they provide the majority of information from a sample. Figure 2 depicts the scattering of electrons based on an interaction with a singular atom for simplicity. Because of the importance of the angle of scattering it is important to discuss the concept of a “differential cross section”. This term describes the angular distribution of scattering from an atom and can be modeled by the following equation, with the variables listed below as well.

- θ is the scattering angle
- $d\theta$ is the incremental increase in scattering angle
- $d\Omega$ is the incremental increase in solid angle

$$d\Omega = 2\pi \sin\theta d\theta$$

The characteristics of the scattering event is controlled by the characteristics of the atom such as electron energy and atomic number/weight. When considering a sample rather than a single atom other factors become important such as thickness, density and crystallinity.

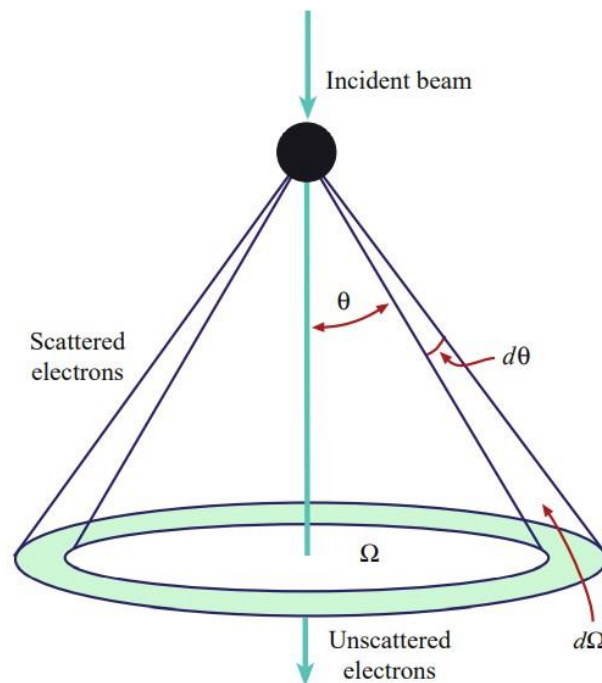


Figure 2: Electron scattering by an isolated atom. The electrons are scattered through a semi angle θ and total solid angle scattering is Ω . Reprinted from the transmission electron microscope (p 23)

One of the most important uses for the scattered electrons is the recording of diffraction patterns. Electron diffraction is a fundamental analytical technique employed by TEMs that utilises the wave nature of electrons to obtain information on the crystal structure, lattice repeat distance and specimen shape. The equation for the wavelength of the propagating electrons at a given accelerating voltage is given below, with the variables listed below as well.

- Wavelength (λ)
- Planks constant (h)
- Mass (m)
- Accelerating voltage (eV)

$$\lambda = \frac{h}{\sqrt{2meV}}$$

Diffraction patterns are produced when a thin crystalline specimen is subjected to a parallel beam of high energy electrons. Due to the sample typically being 100 nm or less thick, the electrons will pass through the sample and will either remain undeviated or will scatter at an angle to the incident electron beam. The end result is generally a non-uniform distribution of electrons which contain all the structural and chemical data of the specimen (Williams and Carter, 1996) The spacing between atoms in a solid is about a hundred times larger than the wavelength of the electrons in the incident beam (for example, electrons have a wavelength of 2.7 pm in an electron beam of 200 kV, the voltage used in the TEM studies of this thesis).

Electron diffraction follows Bragg's law, which states that an incident electron on a crystal surface will reflect back with a scattering angle similar to the incident angle (the angle between

incident ray and the crystal plane), and will reflect most strongly when the interplanar spacings (d-spacings) equals a whole number of the wavelengths. The equation for Bragg's law is given below, with the variables listed below as well.

- λ is the wavelength of the electron
- d is the interplanar spacings
- θ is the incident angle • n is a whole number

$$n\lambda=2d\sin\theta$$

This relationship between incident electrons and crystal lattice spacing is very important as TEMs are capable of adjusting wavelengths of the incident electrons (λ) and one can measure θ experimentally. Therefore, using Bragg's law the user can determine the interplanar spacings of the sample which allows him to identify the sample using crystallographic data bases such as the American Mineralogist Crystal Structure data base (Williams and Carter, 1996). The most relevant minerals in this thesis are chromite, minerals of the chlorite group and hausmannite with prominent d-spacings at 2.51, 14.3, 2.49 Å, respectively. On the basis of the latter d-spacings and the wavelengths of the electrons at 200 kV, the most common angles of diffraction were in the range of 0.3094 and 0.0538 °2 θ

Another important parameter is the camera length because the camera length must be known to calculate the lattice d-spacings in the electron diffraction pattern. The camera length is the distance from the sample to the projected image as shown in figure 3. This distance is necessary to obtain precise measurements from a diffraction pattern because the projection process enlarges

the distance between the reflections in the diffraction pattern. With the precise camera length, the d-spacings can be calculated with the following equation

- d is the spacing between lattice planes
- L is the camera length
- λ is the wavelength of the electrons
- R is the measured distance between the spot and the center of the diffraction pattern

$$L\lambda = Rd$$

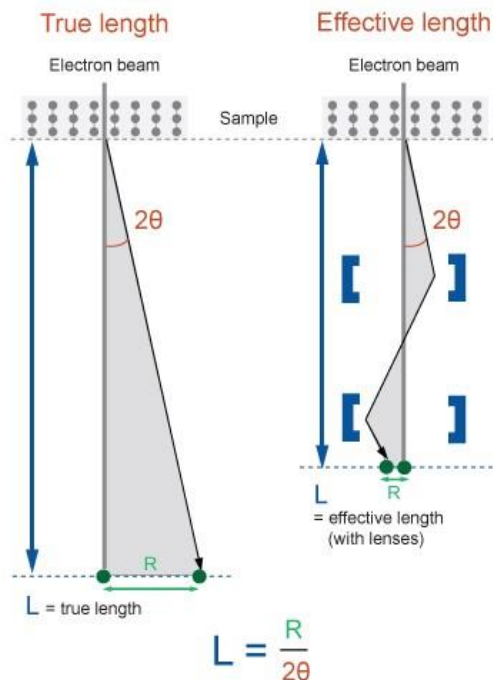


Figure 3: The diffraction pattern (formed in the back focal plane) forms the projected image on the screen and can be recorded, hence the term 'camera length' since this is where the camera is positioned. Reprinted from <https://myscope.training>.

Figure 4 shows a TEM diffraction pattern of chromite. The area marked X in the center of the image represents the electrons that passed directly through the foil and the surrounding spots and

lines represent the various diffracted electrons that are scattered from the different crystal planes (Williams and Carter, 1996). The crystallinity of the sample itself plays a major role in the resultant diffraction pattern. Crystalline materials are composed of periodically arranged atoms that will scatter the electrons in certain directions, this will create high intensity peaks that represent the lattice planes of the individual crystals. If there are many different crystals being subjected to the electron beam then there will be many high intensity peaks forming rings; the distance between each ring represents the different lattice planes of the crystals. In the case of a sample that doesn't have any periodicity and the atoms are randomly distributed (amorphous), the electrons will be scattered in many different directions creating a diffraction pattern with no discernable peaks or rings (Williams and Carter, 1996). Figure 5 displays an example of an amorphous diffraction pattern.

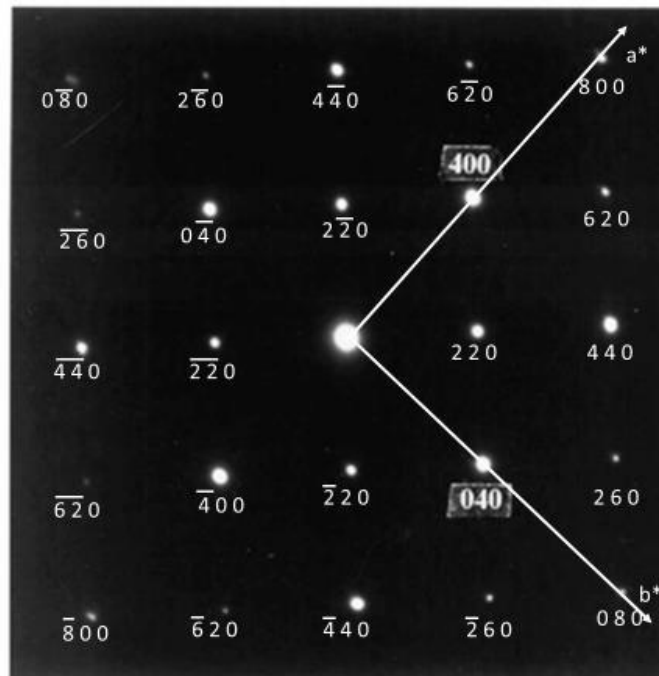


Figure 4: Chromite SAED pattern in the a/b plane ($hk0$). The systematic absences for the space group $F4/d\ 3\ 2/m$ in this plane are odd numbered h and k indices such that $h, k = 2n$ and $h+k = 4n$.

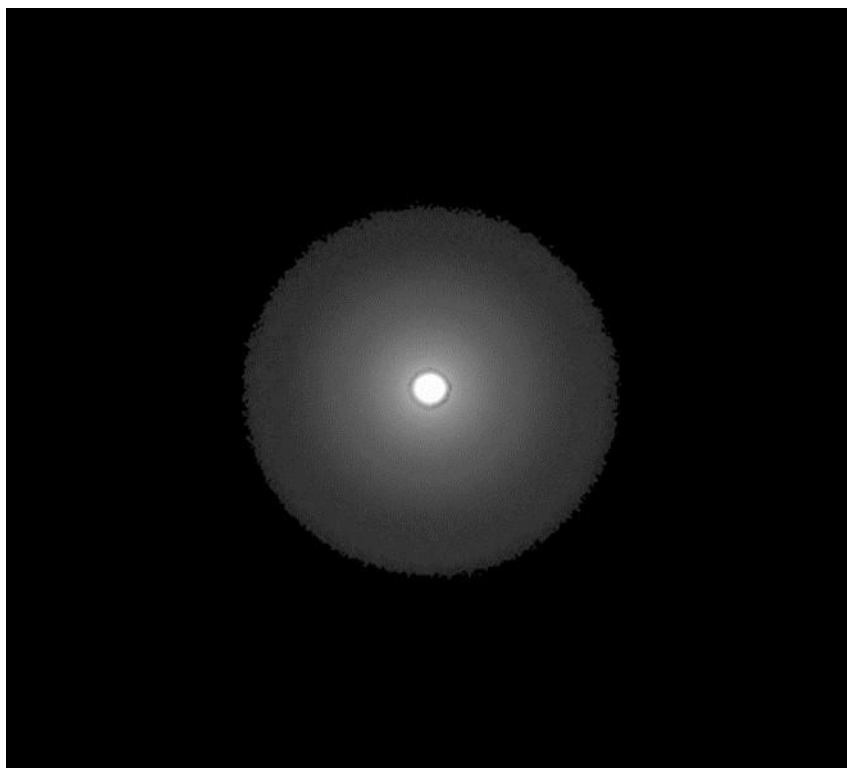


Figure 5: TEM diffraction pattern of an amorphous Cr-(hydr)oxide

References

- Barnhart, J. (1997) Occurrences, uses, and properties of chromium. *Regulatory toxicology and pharmacology*, 26, S3-S7.
- Botton, G. (2007) Analytical electron microscopy. In *Science of Microscopy* (pp. 273-405). Springer, New York, NY.
- Caraballo, M. A., Rimstidt, J. D., Macías, F., Nieto, J. M., and Hochella Jr, M. F. (2013) Metastability, nanocrystallinity and pseudo-solid solution effects on the understanding of schwertmannite solubility. *Chemical Geology*, 360, 22-31.
- Choppala, G., Bolan, N., and Park, J. H. (2013) Chromium contamination and its risk management in complex environmental settings. *Advances in Agronomy*, 120, 29-172. Academic Press.
- De Yoreo, J. J., Gilbert, P. U., Sommerdijk, N. A., Penn, R. L., Whitlam, S., Joester, D., Zhang, H., Rimer, J.F., Navrotsky, A., Banfield, J.F., Wallace, A.F. Michel, M.F., Meldrum, F.C., Cölfen, H., and Dove, P.M. (2015) Crystallization by particle attachment in synthetic, biogenic, and geologic environments. *Science*, 349, 498-506.
- Fendorf, S.E. (1995) Surface reactions of chromium in soils and waters. *Geoderma* 67, 55-71.
- Gadd, G. M., and White, C. (1993) Microbial treatment of metal pollution—a working biotechnology?. *Trends in biotechnology*, 11, 353-359.
- Guertin, J., Jacobs, J. A., & Avakian, C. P. Eds. (2004). *Chromium (VI) handbook*. CRC press.
- Hochella, M. F. (2002) Nanoscience and technology: the next revolution in the Earth sciences. *Earth and Planetary Science Letters*, 203, 593-605.
- Hochella, M. F., Moore, J. N., Putnis, C. V., Putnis, A., Kasama, T., and Eberl, D. D. (2005)

- Direct observation of heavy metal-mineral association from the Clark Fork River Superfund Complex: Implications for metal transport and bioavailability. *Geochimica et cosmochimica acta*, 69, 1651-1663.
- Hochella, M.F., Lower, K.S., Maurice, P.A., Penn, R.L., Sahai, N., Sparks, D.L., Twining, B.S. (2008) Nanominerals, mineral nanoparticles, and earths systems. *Science*, 319, 1631-1635.
- Hochella, M.F., Aruguete, D., Kim, B., and Madden, A.S. (2012) Naturally Occurring Inorganic Nanoparticles: General Assessment and a Global Budget for One of Earth's Last Unexplored Major Geochemical Components. *Nature's Nanostructures*, 1.
- Hotze, E. M., Phenrat, T., and Lowry, G. V. (2010) Nanoparticle aggregation: challenges to understanding transport and reactivity in the environment. *Journal of Environmental Quality*, 39, 1909-1924.
- Hseu, Z., Iizuka, Y. (2013) Pedogeochemical characteristics of chromite in a paddy soil derived from serpentinites. *Geoderma*, 202, 126-133.
- Kadin, A. M. (2006) Wave-particle duality and the coherent quantum domain picture. *Princeton Junction*, 1-13.
- Liu, C., Hystad, G., Golden, J. J., Hummer, D. R., Downs, R. T., Morrison, S. M., Ralph, J.P., and Hazen, R. M. (2017) Chromium mineral ecology. *American Mineralogist*, 102, 612619.
- Madden, A. S., and Hochella Jr, M. F. (2005) A test of geochemical reactivity as a function of mineral size: Manganese oxidation promoted by hematite nanoparticles. *Geochimica et Cosmochimica Acta*, 69, 389-398.

- Mirabello, G., Ianiro, A., Bomans, P. H., Yoda, T., Arakaki, A., Friedrich, H., de With, G., and Sommerdijk, N. A. (2020) Crystallization by particle attachment is a colloidal assembly process. *Nature Materials*, 19, 391-396.
- National Academy of Sciences (NAS), (1974) Chromium. National Academy of Sciences, USA.
- Oliveira, H. (2012) Chromium as an environmental pollutant: insights on induced plant toxicity. *Journal of Botany*, vol. 2012
- Oze, C., Fendorf, S., Bird, D.K., and Coleman R.G. (2004) Chromium geochemistry in serpentinized ultramafic rocks and serpentine soils from the Franciscan complex of California. *American Journal of Science*, 304, 67-101.
- Plathe, K. L., Von der Kammer, F., Hassellöv, M., Moore, J., Murayama, M., Hofmann, T., & Hochella, M. F. (2010) Using FIFFF and aTEM to determine trace metal–nanoparticle associations in riverbed sediment. *Environmental Chemistry*, 7, 82-93.
- Richard, F. C., and Bourg, A. C. (1991) Aqueous geochemistry of chromium: a review. *Water research*, 25, 807-816
- Rosenauer, A., Krause, F. F., Müller, K., Schowalter, M., and Mehrtens, T. (2014) Conventional transmission electron microscopy imaging beyond the diffraction and information limits. *Physical review letters*, 113, 096101.
- Salem, F. Y., Parkerton, T. F., Lewis, R. V., Huang, J. H., and Dickson, K. L. (1989) Kinetics of chromium transformations in the environment. *Science of the Total Environment*, 86, 25-41.
- Shiraki, K. (1997) Geochemical behavior of chromium. *Resource geology*, 47, 319-330.
- Tratnyek, P. G., and Macalady, D. L. (2000) Oxidation-reduction reactions in the aquatic environment. *Handbook of Property Estimation Methods for Chemicals: Environmental and Health Sciences* Lewis, 383-415.

- Wang, Z., Jones, K. M., Norman, A. G., Moseley, J., Repins, I. L., Noufi, R., Yan, Y., and AlJassim, M. M. (2013) Electron microscopy study of individual grain boundaries in Cu₂ZnSnSe₄ thin films. Photovoltaic Specialists Conference, 39, 1681-1684.
- Williams, D. B., and Carter, C. B. (1996) The transmission electron microscope. Springer, Boston, MA.
- Xu, R., Pang, W., Huo, Q. Eds. (2010) Modern inorganic synthetic chemistry. Elsevier, Amsterdam.

Chapter 2

Abstract

The discovery of chromite nanoparticles in silicates of ultramafic rocks may change our approach on the environmental risk assessment of mine waste associated with chromitite mining. This study shows for the first time that the alteration of Cr-rich silicates results in the release of chromite nanoparticles and that their interaction with oxidizing Mn-oxide nanoparticles results in the dissolution of chromite and Mn-oxide nanoparticles and in the precipitation of Fe³⁺- and Cr³⁺-hydroxides. During these processes, the formation of hexavalent Cr is suppressed by reductive Fe²⁺-surface sites on chromite nanoparticles and Fe²⁺-bearing silicates and by functional groups on organic matter. Transmission electron microscopy (TEM) in combination with ultra-microtomy, centrifugation, chromatography, ICP-MS and UV-VIS were used to characterize the occurrence of chromite nanoparticles, their release and alteration and the formation of hexavalent Cr aqueous species. TEM analysis of clinocllore grains from a chromitite sample of the Mum and Alice June claims ore deposits (California) reconfirms the occurrence of chromite nanoparticles in Cr-rich silicates with chromitite. The chromite nanoparticles form in minerals of the chlorite and serpentinite group most likely during greenschist metamorphism via a coupled dissolution-reprecipitation process. Alteration of clinocllore grains containing chromite nanoparticles results in the release of the nanoparticles and their attachment to Al-silicate colloids. Chromite nanoparticles with the endmember composition FeCr₂O₄ are synthesized and their interaction with Mn-oxide nanoparticles (hausmannite, Mn₃O₄), Fe²⁺-silicates (chamosite, [(Fe_{3.9}Mg_{0.62}Al_{0.48}) Al(Si₃Al)O₁₀(OH)₈] and organic matter is studied over a period of six to nine months in suspensions of pH = 5. The

interaction of chromite and hausmannite nanoparticles is facilitated by the aggregation of the nanoparticles and coupled adsorption-dissolution-precipitation processes. Processes on the surfaces of the hausmannite nanoparticles involve the adsorption of Cr^{3+} and Fe^{2+} -species, the reductive dissolution of the substrate (reduction of Mn^{3+} to Mn^{2+} by Fe^{2+} species) and its replacement by amorphous or nanocrystalline Cr^{3+} -bearing Fe^{3+} -hydroxides. Processes on the surfaces of the chromite nanoparticles include the adsorption of Mn-species, the oxidative dissolution of the substrate (oxidation of Fe^{2+} and perhaps Cr^{3+} by Mn^{3+} species), its replacement by an amorphous or nanocrystalline Mn-bearing Cr^{3+} -hydroxide matrix and the formation of the Cr^{3+} -hydroxides bracewellite and grimaldite within the latter matrix. Analyses of the suspensions indicate only minor amounts of hexavalent Cr in the suspensions ($< 5 \mu\text{g kg}^{-1}$) suggesting that the majority of the released Cr species adsorb to mineral surfaces or reprecipitate with Cr- and Fehydroxide phases.

2.1 Introduction

Chromium (Cr) is found throughout the earth's domains and is the 17th most abundant element in the earth's mantle (Oliveira, 2012). Chromium is one of the most important industrial metals and has been increasingly used in many different industries such as leather tanning, metallurgy and electroplating (Barnhart, 1997; Oliveira, 2012). The higher demand for Cr has led to an increase in mining and exploration activities for Cr resources globally (U.S. Geological Survey, 2020), including the new development of a large chromite mine in the "Ring of Fire" region of northern Ontario, Canada.

The most prevalent pathways for Cr to be released into the environment are related to Cr bearing wastes and spills (Fendorf, 1995). One of these potential pathways is the release of

chromite nanoparticles during the weathering of ultramafic waste rock during mining activities (Schindler et al. 2017). The objectives of this study are to further investigate the occurrence of chromite nanoparticles in Cr-rich silicates of ultramafic rocks; their release during the weathering of the silicates and their alteration in the presence of a strong oxidant (Mn-oxide nanoparticles) and reductants such as chamosite, a Fe²⁺-rich mineral of the chlorite group and organic matter.

2.1.1 Geochemical and mineralogical background information on the environmental fate of Chromium and chromite in a low-T environment

Minerals of the spinel group such as chromite and Cr-bearing magnetite are the most common Cr-bearing minerals, with chromite being the primary ore mineral for Cr (Hseu and Iizuka, 2013; Oze et al., 2004). Economically relevant chromite deposits generally occur as podiform deposit, stratiform deposits or irregular stratiform deposits (Mosier et al., 2012, Schulte et al., 2012). Podiform deposits are small magmatic chromitite autoliths found within the ultramafic section of ophiolite complexes (Mosier et al., 2012). Stratiform deposits are mafic to ultramafic layered intrusions with cyclical laterally continuous chromitite seams (Schulte et al., 2012). Both podiform and stratiform deposits are economically significant sources of Cr with large chromite ore deposits such as “Ring of Fire” and Bushveld being stratiform deposits (Schulte et al., 2012).

Soils formed from chemical and mechanical weathering of ultramafic rocks and their metamorphosed equivalent are known as serpentinite soils (Oze et al., 2004; Oze et al., 2007). These soils are typically enriched in Cr (up to 80 600 mg/kg Cr) as compared to soils formed from other rocks types (7-21 mg/kg Cr). The concentration and distribution of Cr in serpentinite

soils can be highly variable. It depends foremost on the concentrations of Cr in the parent rock but is also controlled by climate, biota and formation time of the soil/regolith (Oze et al., 2004).

The valences of Cr range from Cr^{2+} to Cr^{6+} with Cr^{3+} and Cr^{6+} being the most stable valences under surface conditions on Earth (Fendorf and Zasoski, 1992). Trivalent Cr is nontoxic, chromite-bearing minerals have commonly a low solubility and Cr^{3+} aqueous species have a relative low mobility. Hexavalent Cr is a known toxicant and carcinogen, chromate-bearing minerals have often (but not always) a higher solubility than chromite-bearing minerals and chromate aqueous species have a higher mobility than their Cr^{3+} counterparts (Fendorf and Zasoski, 1992; Oliveira, 2012). In ultramafic rocks, Cr is dominantly present as Cr^{3+} and the release of Cr^{3+} from ultramafic rocks into the environment is considered less environmentally hazardous than the release of Cr^{6+} by anthropogenic processes unless the former oxidizes to the latter ion (Fendorf and Zasoski, 1992; Godgul and Sahu, 1995). Hexavalent Cr^{6+} in natural solutions commonly occur in proximity to ultramafic rocks such as those found in ophiolite complexes (Ball and Izbicki, 2004; Manning et al., 2015; Morrison et al., 2015; Robles-Camacho and Armienta, 2000).

The only known naturally occurring oxidizing agents of Cr^{3+} are Mn-oxides (Fendorf and Zasoski, 1992; Weaver and Hochella, 2003). Studies on the oxidation of Cr^{3+} by Mn-oxides indicate that (1) Cr^{3+} oxidation rates around pH=5 are very rapid, but as Cr^{3+} concentration and pH increase the reactions become limited; (2) products of the redox reaction are commonly Mn^{2+} and Cr^{6+} which both do not limit the oxidation of Cr^{3+} through a shift in the redox potential or equilibrium; (3) Mn-oxides with the greatest and longest lasting oxidizing ability are those that contain both Mn^{3+} and Mn^{2+} (Fendorf and Zasoski, 1992; Weaver and Hochella, 2003). Oze et al. (2007) examined the abundance of Cr_{total} and hexavalent Cr in solution after interaction of

micrometer-size chromite grains with birnessite (MnO₂). The authors found that the rate for the formation of hexavalent Cr increases as pH decreases and can be described by $d[\text{Cr}^{6+}]/dt = k' \{\text{Chromite}\}^{0.7}$ (1) where $k'_=$ is $(1.6pH^2 - 25pH + 97)$ nM liter^{0.7} m^{-1.4} h⁻¹. The authors also studied the formation of hexavalent Cr in three serpentinite soils in the presence of chromite and in the presence and absence of birnessite. Here, the authors showed that the addition of birnessite significantly increased the production of Cr⁶⁺ in all three soils. The observations by Oze et al. (2007) are in accord with observations by Fandeur et al. (2009) who identified a close association of Cr⁶⁺ to Mn-oxides in a lateritic regolith that developed on ultramafic rocks in New Caledonia (with up to 20 wt % total Cr).

In many types of Cr-rich soil, Cr⁶⁺ can be reduced by various substances including organic matter, Fe²⁺ and sulfides (Fendorf and Zasoski, 1992). A comparative study of the reduction of Cr⁶⁺ by humic acids and Fe²⁺ showed for example that humic acid is a stronger reductant of Cr⁶⁺ than Fe²⁺ (Jiang et al., 2014). Furthermore, Hausladen and Fendorf (2017) show that organic carbon can suppress the oxidation of Cr³⁺ to Cr⁶⁺ even in the presence of Mn oxides.

Recently, Schindler *et al.* (2017) showed that chromite nanoparticles occur within clinocllore and lizardite grains in chromitite ore from the Black Thor chromium deposit in central Canada and the Mistake mine, part of the Franciscan ophiolite complex, California, USA. The chromite nanoparticles are 3-5 nm in diameter and occur in random orientations throughout the host silicates. Schindler et al (2017, 2018) also conducted dissolution experiments under acidic conditions (pH = 2.5) to investigate the chemical weathering of chromite and clinocllore in chromitite from the Black Thor chromium deposit. These experiments indicate that amorphous silica is the primary alteration product of clinocllore under acidic conditions and that the latter alteration product does not contain any chromite nanoparticles. This is a significant observation

because silicates are more susceptible to chemical weathering than chromite and their weathering would result in the release of chromite nanoparticles as opposed to Cr^{3+} aqueous species.

Schindler et al. (2018) showed furthermore that the concentration of Cr /chromite nanoparticles in solutions decreases when MnO_2 nanoparticles are added to the solution. Schindler *et al.* (2017, 2018) did not determine whether (a) chromite nanoparticles were still in solution during or after the dissolution experiment and (b) the depletion of Cr in the presence of MnO_2 nanoparticles was the result of (a) aggregation of chromite- MnO_2 nanoparticles or (b) adsorption of Cr-aqueous species onto the surfaces of MnO_2 nanoparticles. In either case, the potential release of chromite nanoparticles into the environment has a significant impact on the environmental fate of Cr^{3+} and its potential oxidation to Cr^{6+} . This is because the reactivity and overall fate of Cr in the environment will be governed by the unique properties of nanoparticles such as melting temperature, ability to adhere to surfaces, solubility and ability to catalyse reactions (Aliofkhazraei et al., 2016). The latter three properties are the result of (a) an increasing surface area to volume ratio and (b) change in the surface/near surface atomic structure with decreasing particle size (Kumar, 2012; Hochella et al., 2008). These properties can increase the rate of chemical reactions by many orders of magnitude including those of oxidation, reduction and dissolution reactions (Hochella et al., 2008; Kaptay, 2012). Furthermore, gravitational settling has little to no impact on the soil and water mobility of nanoparticles, whereas Brownian motion, adsorption mechanisms and acid-base processes on the surface of the nanoparticles become far more important and will affect the number and types of nanoparticle-nanoparticle interactions and their degree of aggregation (Hotze et al. 2010; Kumar, 2012).

2.1.2 Detailed objectives

An understanding of the fate of chromite nanoparticles in the environment requires knowledge about their interactions with other nanoparticles, mineral surfaces and redox-sensitive components in the soil environment such as Mn-oxides and organic matter (Theng et al., 2008). Oze et al. (2007) showed that the interaction of chromite and birnessite particles in suspensions results in the formation of hexavalent Cr even in the presence of Fe²⁺-bearing minerals within serpentinite. However, the underlying mechanisms for this interaction with respect to the formation of hexavalent Cr and other phases and ions remain unclear.

Hence, the objectives of this study are to examine the occurrence and release of chromite nanoparticles and their alteration in the presence of minerals and components most likely present in serpentinite soils. These goals will be achieved through conducting three distinct analytical and experimental approaches:

- I. Scanning electron microscopy and a combination of ultra-microtoming, transmission electron microscopy (TEM) and Scanning TEM (STEM)-energy dispersive spectroscopy (EDS) in order to examine the abundance and distribution of Cr and chromite nanoparticles within silicates of chromitites (from locations other than those studied by Schindler et al. 2017 and 2018).
- II. Leaching of a silicate-enriched fraction of a chromitite in combination with TEM-STEMEDS analyses in order to determine whether chromite nanoparticles are released upon the weathering of their silicate hosts;
- III. Long-term (six to nine months) batch experiments in combination with TEM-STEM-EDS in order to characterize the alteration of synthesized chromite nanoparticles in the presence of other components most likely present in serpentinite soils such as Mn-oxide

nanoparticles, chamosite (an Fe^{2+} -rich mineral of the chlorite group) and organic matter. Here, the long-term batch experiments will be conducted under geochemical conditions similar to those in the eutric brunisolic soils surrounding the chromite ore deposits at the “Ring of Fire” which have contact pH-values of $\text{pH} = 4.5$ to 5.0 on the surface and $\text{pH} > 5.5$ at greater depth (Smith et al. 2011); *i.e.* they will be conducted at a constant pH of 5 which is also the pH at which the highest oxidation rate of Cr^{3+} to Cr^{6+} occurs (Bulmer and Lavkulich, 1994; Fendorf and Zasoski, 1992). Hausmannite (Mn_3O_4) nanoparticles will be added to each experiment as Mn-oxides often occur in the nano-size regime within soils (Post, 1999; Theng et al., 2008) and contain Mn^{3+} ions which are more effective oxidants for $\text{Cr}^{3+} \rightarrow \text{Cr}^{6+}$ than e.g. Mn^{4+} (Weaver and Hochella, 2003). Chamosite and organic matter will be also added to some of the experiments in order to study the alteration of chromite nanoparticles in the presence of surfaces containing reducing Fe^{2+} - surface sites (chamosite) or functional groups (organic matter).

2.2 Materials and Methods

Ultramafic rocks from chromite ore deposits in Ontario, Quebec, Newfoundland, and California were obtained from numerous sources including the Ontario Geological Survey, the collection at the Department of Earth Sciences at Laurentian University and the Royal Ontario Museum in Toronto. Table 1 lists the origin of the samples, the type of ore deposit, the mineral hosting potential chromite nanoparticles and the Cr-concentrations in these silicates. X-ray powder diffraction (XRD) and Scanning Electron microscopy (SEM) were used to identify silicate and (hydr)oxide minerals in the chromite-bearing ore and to determine the Crconcentrations in these minerals (see below). Silicate minerals are either lizardite, a mineral of

the serpentite group (asbestos-type mineral), or clinochlore, a mineral of the chlorite group (Table 1). The hydroxide mineral brucite is similar to clinochlore and lizardite a low-T alteration product of ultramafic silicate minerals such as amphiboles, pyroxenes and olivines (Klein et al., 2013).

TABLE 1. Characterized chromitite ore samples, the location and type of their respective ore deposit and the hosts and concentrations of Cr in the ore (excluding chromite)

Sample ID	Location of ore deposit	Type of chromite ore deposit	Host of Cr/chromite nanoparticles	Range of Cr concentrations in hosts
M31456	Mum and Alice June claim, California	Ophiolite	Brucite, $Mg(OH)_2$	1-4 at%
M31456	Mum and Alice June claim, California	Ophiolite	Clinochlore $Mg_5Al(AlSi_3O_{10})(OH)_8$	0.5-2 at%
M29852	Asbestos, Quebec	Ultramafic intrusion	Lizardite, $Mg_3Si_2O_5(OH)_4$	< 0.5 at%
M7560	Black lake, Quebec	Ultramafic intrusion	Lizardite, $Mg_3Si_2O_5(OH)_4$	< 0.5 at%
M41446	Crushed Stone Newfoundland	Ophiolite	Lizardite, $Mg_3Si_2O_5(OH)_4$	<0.9 at%
M9431	Lewis Hill, Newfoundland	Ophiolite	Lizardite, $Mg_0_3Si_2O_5(OH)_4$	<0.2 at%
Sample from Schindler et al. 2017	Black Thor deposit “Ring of Fire”	Ultramafic intrusion	Clinochlore, $Mg_5Al(AlSi_3O_{10})(OH)_8$	1-3 at%
Sample from Schindler et al. 2017	Mistake Mine, Fresno, California	Ophiolite	Lizardite $Mg_3Si_2O_5(OH)_4$	1 at%
Sample from Schindler et al. 2017	Mistake Mine, Fresno, California	Ophiolite	Clinochlore $Mg_5Al(AlSi_3O_{10})(OH)_8$	3 at%

Samples examined in detail were high grade chromitite ore samples from the Black Thor chromite deposit, Ontario, Canada and from the Mum and Alice June claims mine in California, USA (Fig. 1). The Black Thor chromite deposit is a sill like intrusion found within the “Ring of Fire” intrusive suite, located in the Neoproterozoic McFaulds Lake greenstone belt (Laarman, 2013). The intrusion hosting the Black Thor deposit consists of cyclically layered ultramafic rocks, beginning with olivine rich lithologies (dunite to peridotite) and progressing upward to more pyroxene rich lithologies (olivine pyroxenite, feldspathic pyroxenite and gabbro). The Black Thor deposit is the most extensive chromite zone in the intrusion and occurs as large thickly bedded chromitite layers at the transition from olivine rich to pyroxene rich lithologies (Weston and Shinkle, 2013; Laarman, 2013; see Schindler et al. 2017, 2018). The Mum and Alice June claims are part of a podiform chromite deposit located about 4 km south of Jacksonville, California (Fig. 1). The deposit consists of small pods and lenticular masses of nearly pure chromite, aggregates of interlayered thin lenses of massive chromite and disseminated chromite all hosted by a serpentinized dunite (Cater, 1948).



FIGURE 1. Topographic map of California with the location of the Mum and Alice June claims indicated with a red dot.

2.2.1 Leaching experiments of Cr-rich clinochlore powders from the Black Thor deposit

A fine-grained silicate rich powder was prepared from the Black Thor chromite samples containing initially ~80% chromite and ~20% clinochlore (on the basis of SEM examination). The chromite samples were crushed using a ring mill which resulted in a powder consisting of grains ranging from 10 μm - 100 μm . A silicate-rich fraction (~30% chromite and ~70% clinochlore (on the basis of SEM examination) was obtained through a heavy-mineral fractionation technique (Wilfley Table). Two-hundred milligram of the latter silicate-enriched fraction was subsequently leached with 50 ml sulfuric acid solutions of pH = 2 and pH = 5. After 3 months continuous shaking in test tubes, 10 mL of the leachate were extracted and parts of their colloidal fractions were deposited on TEM grids via centrifugation (see below).

2.2.2 Reagents for the long-term batch experiments

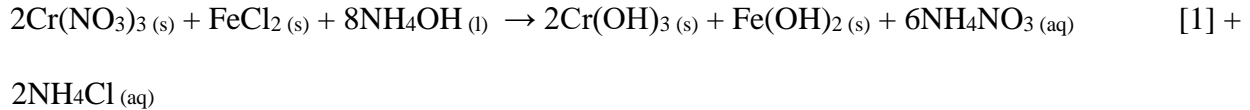
The interaction of chromite nanoparticles with hausmannite nanoparticles was studied in the absence and presence of chamosite and organic rich soil (Table 2). Chamosite samples from the Michigamme mine, Michigan, USA were purchased from “Rogers Minerals” and crushed in a ring mill to a powder containing predominantly silt sized grains. Chamosite $[(\text{Fe}_{3.9}\text{Mg}_{0.62}\text{Al}_{0.48})\text{Al}(\text{Si}_3\text{Al})\text{O}_{10}(\text{OH})_8]$ is a Fe-rich endmember of the clinocllore-chamosite solid solution and a common mineral in serpentinites and ultramafic rocks (Siebecker et al., 2018). Organic rich podzolic soil (contact pH = 5.5) was sampled in a wooded area close to the township of Massey, Ontario (49°19'58.36"N, -82°02'57.24"W). After removal of the larger debris (leaves, sticks) the soil was crushed with a mortar and pestle to a silt-size powder. Hausmannite (Mn_3O_4) nanoparticles were purchased from the company “US Research Nanomaterials, Inc”. Their precharacterization with TEM indicated an average particle size with diameters of $50 \pm 5\text{nm}$. Table S1 and Figures S1-S3 list the chemical compositions and powder diffraction pattern of the chamosite powder, organic-rich soil and hausmannite nanoparticles.

TABLE 2. Long-term batch experiments (6 to 9 months) between chromite nanoparticles (0.01 molL^{-1}) and Mn-oxide nanoparticles (Mn_3O_4 , hausmannite) in the presence and absence of organic-rich soils and chamosite

500 mL Flask #	Cr : Mn	Clinochlore	Organic-rich soil
1	1:1	0	0
2	1:5	0	0
3	1:1	10g	0
4	1:5	10g	0
5	1:1	0	10g
6	1:5	0	10g

The chromite nanoparticles for these experiments were synthesised with sizes similar to those observed in the Cr-rich silicates. The synthesis followed a modified variation of the coprecipitation method used by Matulkova et al. (2015) and Edrissi et al (2011). Stoichiometric amounts of $\text{Cr}(\text{NO}_3)_3 \cdot 9\text{H}_2\text{O}$ and FeCl_2 (Cr : Fe = 2:1) were dissolved into 50 ml of distilled water. This solution was then mixed with 100 ml of distilled water containing glycerol as a capping agent (5% in distilled water) under constant stirring. Ammonium hydroxide precipitating agent was added dropwise until the pH was adjusted to pH = 11-12. The precipitates were then centrifuged and washed with distilled water several times and then dried at around 40°C . Lastly, the precipitates were calcinated in a vacuum sealed glass tube ($< 100 \text{ mTorr}$) at 600°C for 2 hours.

Coprecipitation [1] and calcination [2] reaction can be formulated as follows:



Powders of chromite nanoparticles from two syntheses were mixed and treated in an ethanolbased ultra-sonic bath for 2 hours in order to reduce the size of the nanoparticle aggregates.

2.2.3 Set up of the long-term batch experiments

Six long-term (six to nine months) batch experiments were set up to examine the interaction between chromite and hausmannite nanoparticles in the presence and absence of chamosite and organic-rich soil. The experiments were conducted in 500 mL flasks with a Crconcentration of 0.01 mol/L and Cr: Mn molar ratios of either 1: 1 or 1: 5 (Table 2). Two of these experiments included 10 g chamosite powder and two included 10 g of the organic-rich soil (Table 2). The pH-values in the long-term batch experiments were adjusted to a pH value of pH = 5.0 with sulfuric acid and at a later stage with a 0.1 molL⁻¹ KH₂PO₄ solution (after one month) and a 0.05 molL⁻¹ solution of potassium hydrogen phthalate solution (after every month until the end of the experiment).

Over the course of the experiments, the Eh-pH values were monitored with a YSI ORP probe and a pH meter. Probe and pH meter contain standard hydrogen electrodes which were calibrated against pH solutions of pH 4, 7 and 10 and a K-iodide standard. The standard deviation of individual measurement pH and Eh measurements is circa ± 0.2 units, based on repeated measurements of the standard solutions.

After 6- and 9-months continuous shaking of the 500 ml flasks, 10 mL of the suspensions were extracted and deposited on TEM grids via centrifugation and filtered and analysed for their chemical composition, respectively (see below).

2.2.4 Analysis of Cr in the solute and colloidal fractions after the batch experiments

After a duration of nine months, 10 mL from each batch experiment were filtered with a 0.45 μm Whatman filter cartridge using a 10 mL Luer Lock Syringe. The solutions were treated with an *aqua regia* digest (following method E3470 of the Ministry of the Environment, Conservation and Parks laboratory services branch, MECP) and analysed for major and trace elements with a Perkin Elmer Optima 4300 DV ICP-OES.

The concentrations of Cr^{3+} and Cr^{6+} in the leachate without (the majority of) nanoparticles were determined using a modified version of the method 6800 of the MECP laboratory services branch:

1. After filtering, 50 mL of each sample were mixed with 0.29 g NaCl (0.1 molL^{-1} NaCl solution) in order to promote the aggregation of the remaining chromite- and hausmannite nanoparticles and to desorb any adsorbed Cr^{3+} and Cr^{6+} aqueous species from the surfaces of the solid material.
2. The solutions were subsequently centrifuged at 5000 rpm for 4 hours, which should have deposited particles or aggregates of nanoparticles with diameters larger than 35 nm;
3. The solutions were then diluted by a factor ten and 100 μL of each solution was added to 9.9 mL of a 2 mmolL^{-1} EDTA solution of pH 5 (in order to complex Cr^{3+} and thus preventing its oxidation);

4. These solutions were spiked with a Cr-50 enriched Cr^{3+} -solution containing $100 \mu\text{L}^{-1}$ Cr and a Cr-53-enriched Cr^{6+} -solution containing $100 \mu\text{L}^{-1}$ Cr; an analytical step that allows to monitor any potential changes in the Cr^{3+} and Cr^{6+} concentrations over time;
5. The spiked solutions were heated at 70°C for 40 min and then transferred to a chromatography vial for analysis with an Analytik Jena 820MS ICP-MS with a CRI skimmer cone and a standard sampler cone.

Additionally, 50 ml from each batch experiment were analysed (without the addition of NaCl) at the ALS environmental laboratories. The solutions were treated and preserved with NaOH and an ammonium sulfate/ammonium hydroxide buffer. Subsequent chromatography using a Thermo Scientific Dionex Aquion IC resulted in the separation of CrO_4^{2-} anions from other Cr-bearing species and chromite nanoparticles. The CrO_4^{2-} -bearing solution was treated with diphenylcarbazide (DPC), a colour reagent, which resulted in the simultaneous oxidation of diphenylcarbazide to diphenylcarbazone, the reduction of Cr^{6+} to Cr^{3+} and the chelation of Cr^{3+} by diphenylcarbazone. The concentrations of the latter chelate was determined with the following process known as UV-VIS, A Beam of light with a wavelength of 530nm passes through the chelate in a cuvette, the sample in the cuvette absorbs an amount of this beam of light. The intensity of light that is transmitted through the chelate is measure with a spectrophotometer and compared to a reference measurement of the incident light source. The measured intensity of light that is transmitted by the chelate is then used to calculate the concentration of Cr^{6+} in solution using Beer–Lambert's law.

2.2.5 Powder X-ray powder diffraction, X-ray Fluorescence Spectroscopy and Loss of Ignition

Powder X-ray powder diffraction patterns of chromitite samples and reagents used in the experiments listed above were recorded with an automated Philips PW 1729 X-ray diffractometer and a Bruker D 5000 system using Co K α (1.79 Å) and Cu radiation (1.54 Å), respectively. X-ray diffraction patterns from powdered samples were collected at a voltage of 40 kV and current of 30 mA over a scan range of 5-65° 2 θ and with a step size of 0.02° 2 θ and a dwell time of 2 s per step.

The loss on ignition (LOI) for the chamosite powder was assessed prior to analysis by X-ray fluorescence. The LOI gives the proportion of volatile elements or compounds in a sample (H, H₂O, S, N) and was determined by heating the sample to 100°C under nitrogen atmosphere, and to 1000°C under oxygen atmosphere, until a constant wt. % was reached. The sample was subsequently fused with a borate flux to produce a glass bead for characterization by X-ray Fluorescence Spectroscopy (XRF). The glass bead was subsequently analyzed with a Panalytical Axios Advanced XRF spectrometer.

2.2.6 Preparation of the TEM samples

TEM examinations on the occurrence of chromite nanoparticles in Cr-rich clinocllore were conducted on a sample from the Mum and Alice June claims mine (Fig. 1, Table 1). Electron transparent sections were prepared using a diamond knife of a Leica Ultracut, RMC MT6000 ultramicrotome at the Nanoscale Biomedical Imaging Facility at SickKids, Toronto, Ontario. The ultra-microtome sections were subsequently placed on Copper grids.

Synthesized chromite nanoparticles and purchased hausmannite nanoparticles were deposited onto Cu TEM grids (400 mesh lacey carbon, 100 μ m) through the use of an ethanolbased emulsion. The colloidal fractions of the solutions after the leaching experiment and the long-term batch experiments were also deposited on TEM grids. Here, Cu TEM grids (400 mesh lacey carbon, 100 μ m) were fixed to an epoxy support at the bottom of 15ml centrifuge tubes and then filled with the leachates extracted from the test tubes. The tubes were centrifuged using a Sorvall ST16 centrifuge equipped with a TX-400 swing bucket rotor for 8 hours at 5000 RPM which, according to stokes equation, will deposit all spherical particles with densities and diameters greater than 4.54 g cm⁻³ (density of chromite) and 30 nm onto the TEM grids, respectively.

2.2.7 Scanning electron microscopy and Transmission Electron Microscopy

Scanning electron microscopy on polished chromitite grains embedded in epoxy pucks (Table 1) was conducted with a JEOL 6400 SEM, which was operated with an accelerating voltage of 20 kV and a beam current of 1 nA, in combination with energy dispersive X-ray spectrometry (EDS).

The ultra-microtome sections and TEM grids with deposited colloids/nanoparticles were examined with a field emission Transmission Electron Microscope FEI Talos F200x at the Manitoba Institute of Materials. An accelerating voltage of 200 kV in bright and dark field mode was used with a 16MB ceta camera and Fischicone annular dark field (HAADF) detector to acquire images and SAED.

2.3 Results

The results of the nano-mineralogical study on the Cr-rich clinochlore grains from the Mum and Alice June claims will be addressed first followed by those on the colloidal fractions in the suspension after (a) the leaching experiment of the silicate-enriched chromite ore sample and (b) 6 months duration of the long-term batch experiments.

2.3.1 Silicate hosted chromite nanoparticles in the chromite ore from the Mum and Alice June claims

The Cr concentrations in the silicates of the chromitites ranges from < 0.2 to 4 at% (Table 1). The highest Cr concentrations occur in brucite and clinochlore grains in the sample from the Mum and Alice June claims, California, with Cr-concentrations ranging from 1-4% and 0.5-2%, respectively. Closer inspection of the SEM-EDS chemical maps reveals that the areas with the highest concentrations of Cr occur along the grain boundary between brucite and quartz (Fig. 2a, b). In contrast none of the other ore samples contain silicates with Cr concentrations greater than 0.9 at% (Table 1).

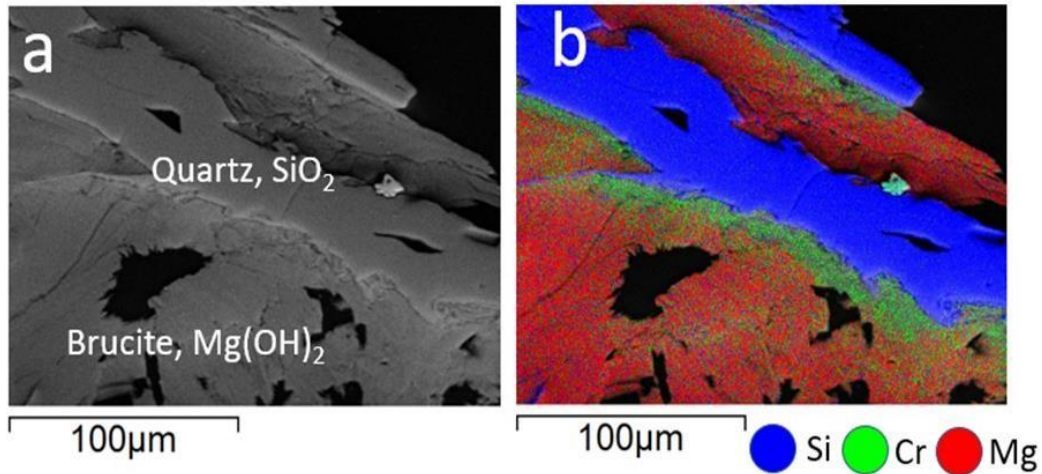


FIGURE 2. (a) SEM-BSE and (b) SEM-EDS chemical distribution map for Si (blue), Cr (green) and Mg (red) of an intergrowth between brucite and quartz in the sample from the Mum and Alice June claims (M31456).

In contrast to the Focused Ion Beam technique, ultra-microtoming an assemblage of mineral grains does not necessarily yield to a site-specific extraction of a TEM sample. Hence, ultra-microtome sections cut from the clinochlore-brucite-quartz-chromite mineral assemblage (Fig. 2a, b) resulted only in the extraction of areas composed of clinochlore and chromite (Fig. 3a). These areas are characterized by long thin needles of clinchlore with dimensions in the range of 200 nm – 5 µm. High resolution TEM images indicate the presence of Mg-depleted chromite nanoparticles along the boundaries of the clinochlore grains (Fig 3a-c). The nanoparticles range in size from 3 to 10 nm and depict characteristic lattice fringes with dspacings of 2.1 Å (400) (Fig. 3d and e).

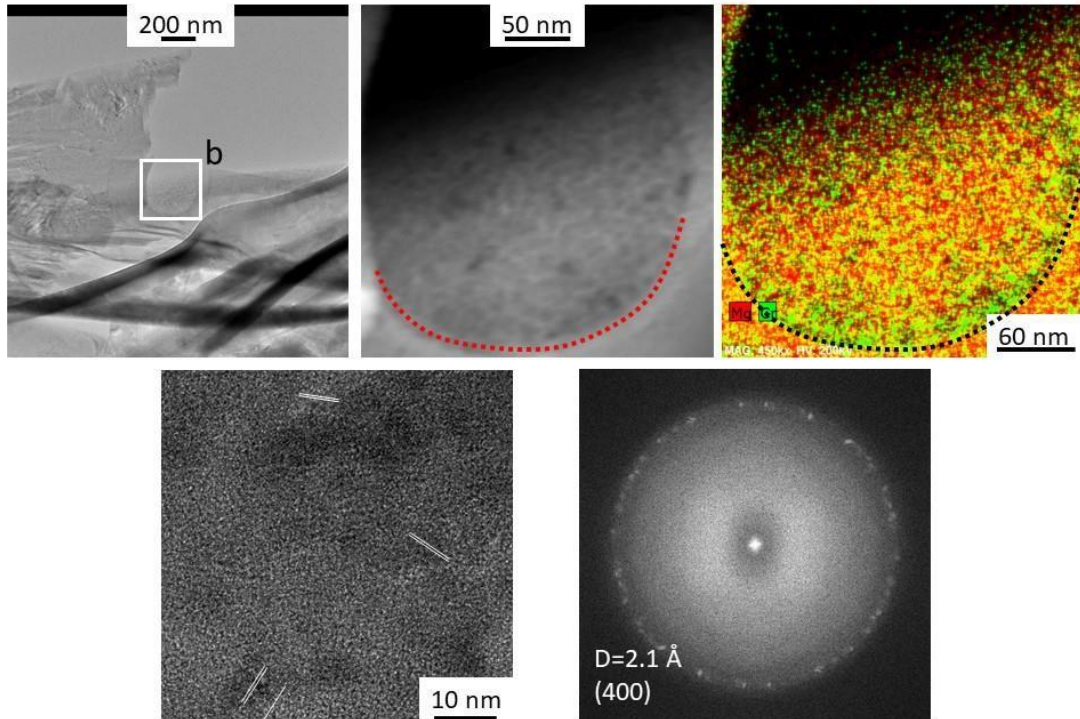


FIGURE 3. (a) TEM image of clinochlore fibers (chl) in a microtome section cut from a clinochlore-brucite-quartz-chromite assemblage; the location of the thinner area shown in (b) and (c) is indicated with a white square; (b) TEM and (c) STEM-EDS chemical distribution map for Mg (red) and Cr (green) of an area within a clinochlore fiber containing chromite nanoparticles; (d) high-resolution TEM image and (e) FFT pattern of a selected area within the area shown in (c) and (d); the FFT pattern (e) indicate characteristic lattice fringes for chromite with d-spacings of 2.1 Å (400).

2.3.2 Mineralogical features in the silicate-enriched fraction of the chromitite ore and in the leachate after the leaching experiment

Scanning electron microscopy studies of the silicate enriched fraction of the chromitite ore after 3 months of the leaching experiments indicate that the chromite grains are barely chemically altered whereas those of clinochlore grains can be extensively etched (Fig. 4a). TEM examinations of the colloidal fraction in the leachates of pH 2 and 5 did not unequivocally identify individual chromite nanoparticles on the TEM grid. Chromite nanoparticles were identified in clinochlore fragments and on the surface of an Al-rich colloid with an elemental Al : Si : Cr : Fe ratio of 10 : 2 : 1 : 1 and no detectable concentrations of Mg. The elongated colloid is

circa 140 nm x 25 nm in size contains circa 6 at% Cr. The chromite nanoparticles on the surface of the colloid have similar chemical composition (depleted in Mg), diameters (3 – 8 nm) and lattice fringes (d-spacings of $d = 2.9 \text{ \AA}$ (220) and 2.1 (400) \AA) as those observed in unaltered clinocllore grains (Fig 4b-d). Chemical distribution maps for Si and Al suggest that either adsorbed silica species or an amorphous Al-silicate precipitate is heterogeneously distributed on the surface of the Al-rich colloid (inlet in Fig. 4c).

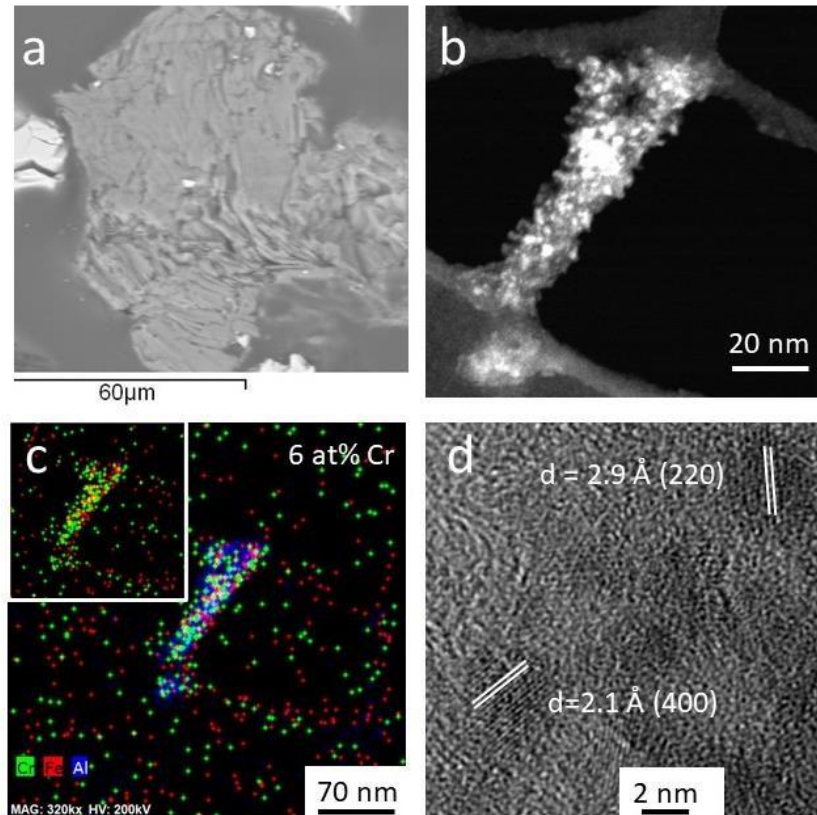


FIGURE 4. (a) SEM-BSE image of a highly etched clinchlore grain (chl) after leaching of a silicate-enriched chromitite powder with a solution of pH=5; (b) STEM and (c) STEM-EDS chemical distribution maps for Cr (green), Fe (red) of an Al-rich colloid in the leachate of pH = 5, for clarity reason, a chemical distribution map for only Si (red) and Al (blue) is shown as an inlet; (d) high resolution TEM image of the chromite nanoparticles on the surface of the Al-rich colloid with characteristic lattice fringes of chromite with d-spacings of 2.1 Å (400) and 2.9 Å (220).

2.3.3 Size and chemical composition of the synthesized chromite nanoparticles

TEM images of the synthesized chromite nanoparticles show the occurrence of individual nanoparticles and aggregates of nanoparticles (Fig. 5a). The chromite nanoparticles have diameters between 5 and 15 nm (Fig 5a) and are thus similar in size as the chromite nanoparticles in the Cr-rich silicates. STEM-EDS chemical distribution maps for Fe (red) and Cr (green) (Fig 5b) indicate a near homogeneous distribution of both elements (average Cr : Fe atomic ratio: 1.8 : 1). High resolution TEM images of the synthesised nanoparticles (Fig 5c), the corresponding

FFT pattern (Fig 5d) and X-ray powder diffraction of the synthesis product (Fig 5e) depict characteristic chromite d-spacings of $d=4.8$ (111), $d=2.9$ (220), $d=2.5$ (311), $d=2.0$ (400) Å.

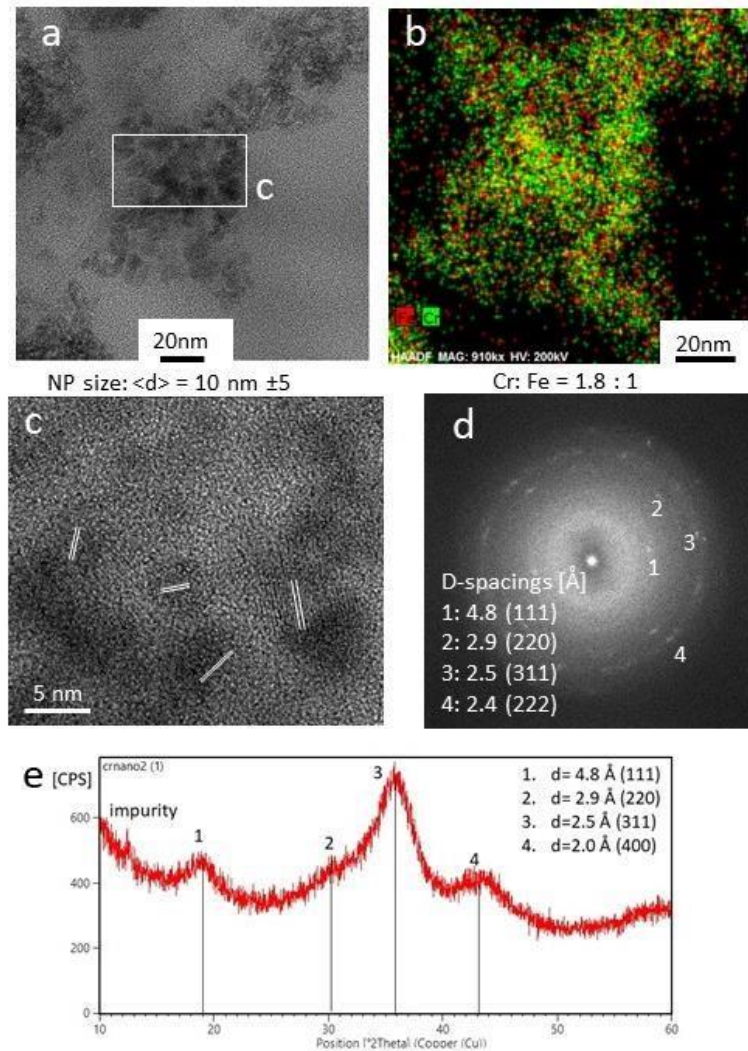


FIGURE 5. Synthesized chromite (chr) nanoparticles used in the batch experiments: (a) TEM image and (b) STEM-EDS chemical distribution map for Fe (red) and Cr (green) of an aggregate of synthesized chromite nanoparticles, the area shown in (c) is indicated with a rectangle; (c) high-resolution TEM image and (d) FFT pattern of a selected area within the aggregate; the FFT pattern indicate that the lattice fringes in (c) are parallel to $d=4.8$ (111), $d=2.9$ (220), $d=2.5$ (311), $d=2.0$ (400); (e) powder diffraction pattern of the synthesized chromite nanoparticles depicting broad peaks with d-spacing similar to those observed in the FFT pattern.

2.3.4 Chemical and mineralogical features of the colloidal fraction in the suspensions after 6 months of the long-term batch experiments

The pH values during all long-term batch experiments rose occasionally above pH = 5 and had to be re-adjusted mainly with a K-hydrogen phthalate solution (see above). The redox potential at this constant pH value varied only slightly in the range of Eh = 0.4 -0.43 V.

Different nanoparticle-adsorbed solute, nanoparticle-nanoparticle and nanoparticlemicroparticle interactions occur in the suspensions. The most notable interaction is the aggregation of chromite and hausmannite nanoparticles (Fig. 6a-b). STEM chemical distribution maps suggest that this aggregation process occurred in the presence of adsorbed phosphate species (in red in Fig. 6b), which originated (most likely) from the KH_2PO_4 buffer added to the solution.

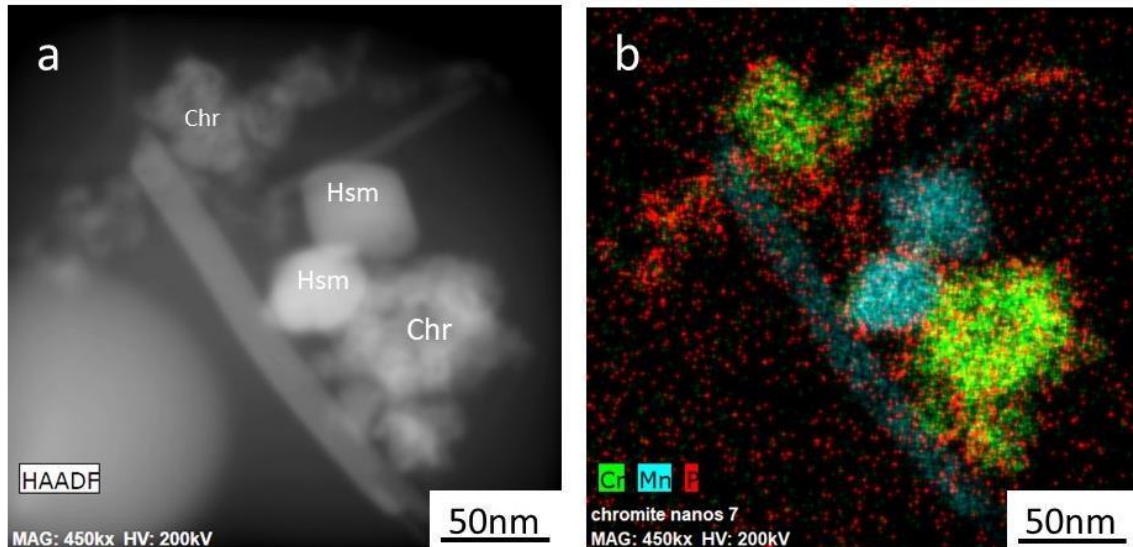


FIGURE 6. (a) STEM image and (b) STEM-EDS chemical distribution map for Cr (green), Mn (blue) and P (red) of an aggregate of hausmannite (Hsm), chromite (Chr) and manganite nanoparticles in a suspension without chamosite and organic matter.

2.3.5 Chemical trends among the nano- to micrometer-size particles

Scanning TEM-EDS chemical analyses of chromite nanoparticles or aggregates of chromite nanoparticles from the suspensions of all long-term batch experiments indicate that (altered) chromite nanoparticles are depleted in Fe and enriched in Mn relative to the synthesized chromite nanoparticles (Fig. 7a). Similarly, the majority of the (altered) hausmannite particles is now enriched in Fe and sometimes in Cr relative to the unaltered. Here, highly altered hausmannite nanoparticles can have Fe : Mn and Cr : Mn ratios up to 1 : 1 and 1 : 3, respectively (Fig 7b). Alterations also occur on the surfaces of the chamosite particles. These are commonly characterized by areas depleted in Mg and enriched in Al and Fe relative to the unaltered grains (Fig. 7c).

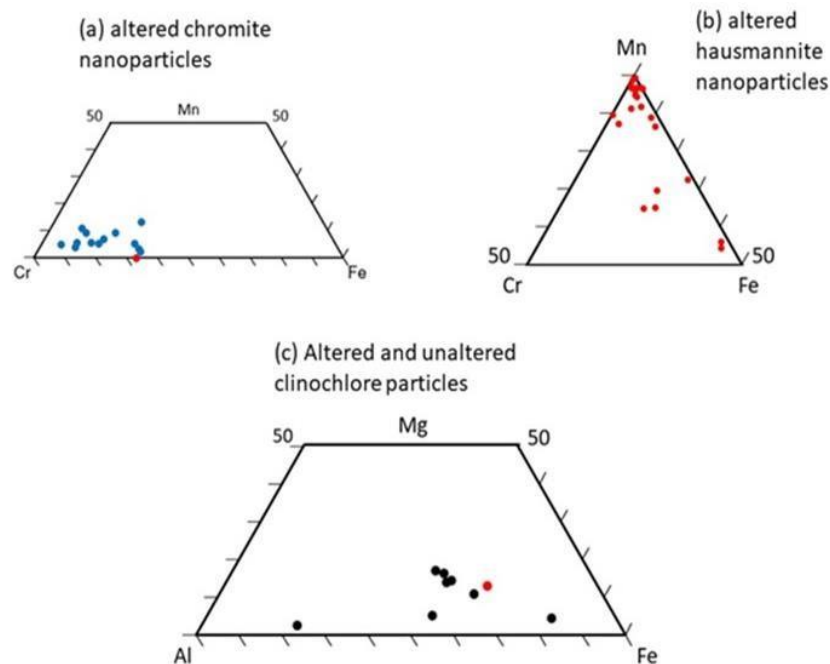


FIGURE 7. Chemical composition of chromite, hausmannite nanoparticles and chamosite particles after the longterm experiments: Ternary plots depicting (a)-(b) Cr : Mn : Fe ratios in (a) altered chromite nanoparticles (blue) in comparison to the ideal stoichiometry of an unaltered chromite (red); (b) altered hausmannite nanoparticles; (c) the Al : Mg : Fe ratio in altered chamosite grains (black) in comparison to the ideal stoichiometry of an unaltered chamosite (red).

2.3.6 Textural, chemical and mineralogical features of chromite-hausmannite nanoparticle aggregates

Figure 8 shows a small aggregate of two altered hausmannite nanoparticles (verified with selected electron diffraction pattern, Fig. S4) and the remains of a chromite nanoparticle from the suspension with the organic-rich soil (experiment 5). The hausmannite nanoparticles are rounded and elongated with dimensions of 60 nm x 40 nm and 40 nm x 30 nm. They are highly altered with etch features at the lower nanometer range (dark spots in Fig. 8a). The remains of a chromite nanoparticle occur below the plane of the hausmannite nanoparticles and can be only recognized in the STEM-EDS chemical distribution map for Fe and Cr (green in Fig. 8b).

The hausmannite nanoparticles are enriched in Fe with an average Mn : Fe ratio of circa 1 : 1. The distribution of Fe is heterogeneous with high abundances of Fe occurring in cracks and on the surface of the hausmannite nanoparticles (in red in Fig. 8c). The latter nanoparticles contain also pockets enriched in Si (in yellow in Fig. 8d) which often overlap or are adjacent to areas enriched in Fe. The remains of the chromite nanoparticles are depleted in Fe with an average Fe : Cr ratio of 1 : 5.

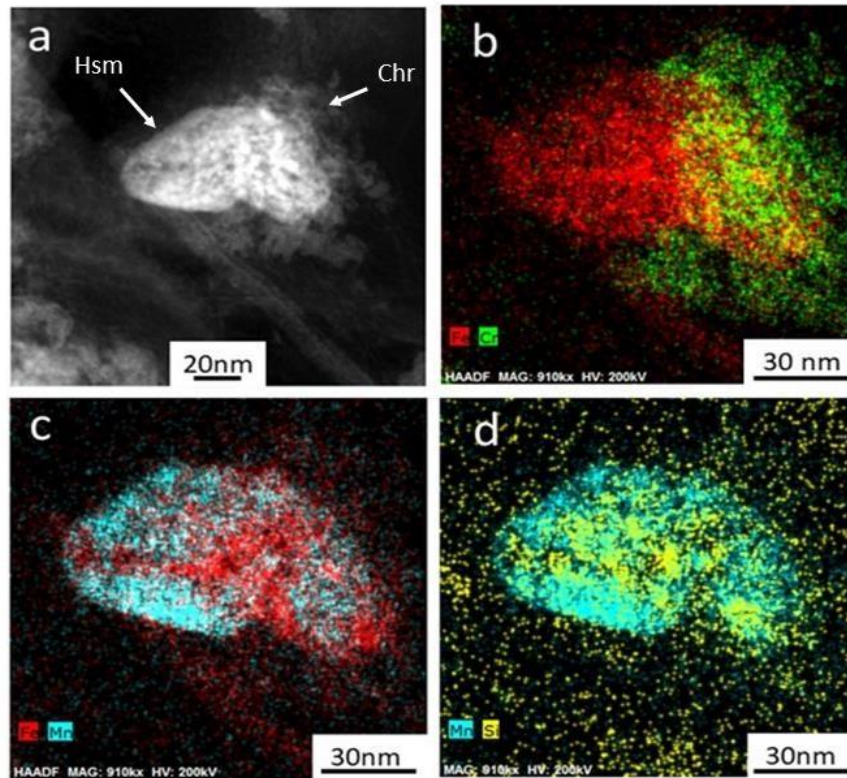


FIGURE 8. (a) STEM image and (b)-(d) STEM-EDS chemical maps for (b) Fe (red) and Cr (green), (c) Fe (red) and Mn (blue) and (d) Mn (blue) and Si (yellow) of an aggregate containing two hausmannite (Hsm) and the remains of a chromite (Chr) nanoparticle.

Large aggregates of hausmannite nanoparticles with attached chromite nanoparticles occur in all suspension. For example, Figure 9 a-d show a micrometer-size aggregate (1.2 μm x 1 μm) from the suspension with the chamosite powder (experiment 3). The aggregate contains highly altered hausmannite nanoparticles along its rim and relatively unaltered nanoparticles in its interior (Fig. 9a-b). The altered hausmannite nanoparticles are enriched in Fe with some reaching Fe : Mn ratios of 1 : 1 (Fig. 9c). They are highly etched with semi rounded pits ranging in size from $d = 10 - 30$ nm (Fig. 9c). The rims of the altered hausmannite nanoparticles are composed of an Fe(hydr)oxide precipitate with a thickness of circa $d = 3 - 5$ nm and without any apparent lattice fringes (Fig. 9c-d). Attached chromite nanoparticles range in size from $d = 20$ to 60 nm and are also rimmed by a thin Fe-(hydr)oxide precipitate (Fig. 9c)

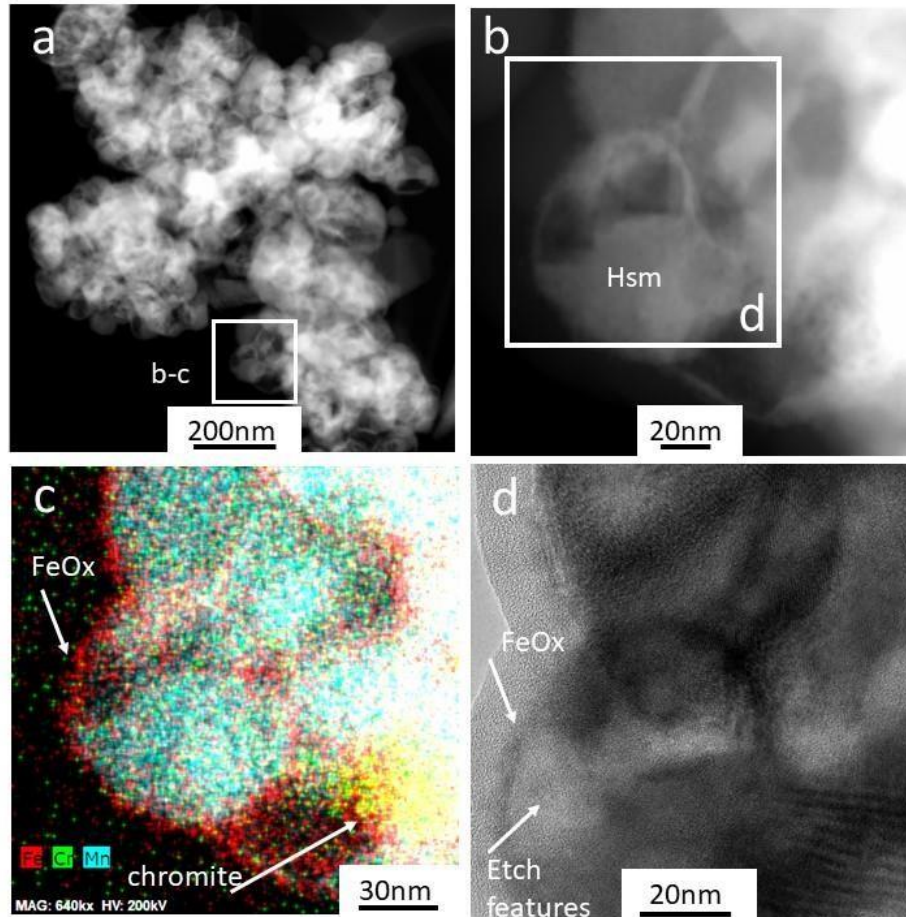


FIGURE 9. (a) STEM image of an aggregate of hausmannite (Hsm) nanoparticles, the area shown in (b)-(d) is indicated with a rectangle; (b) STEM image (c) STEM-EDS chemical map for Fe (red), Cr(green) and Mn (blue) and (d) high resolution TEM image of the area depicted in (a); etch features and a rim of a Fe-(hydr)oxide are indicated with arrows.

2.3.7 Textural, chemical and mineralogical features of secondary Cr-hydroxide phases

Chromium-rich secondary precipitates occur in all suspensions. Figures 10a-d show for example an aggregate of chromite nanoparticles and Cr-(hydr)oxides from the suspension with organic-rich soil (experiment 6). The Cr-(hydr)oxide precipitate is depleted in Fe with Fe : Cr ratios as low as 1 : 14. It depicts two distinct features: a highly porous 60 nm x 200 nm matrix and two parallel rods with 100 nm x 8 nm and 50 nm by 8 nm in size (Fig. 10a-d). Rods and

matrix contain similar amounts of Mn with an average Mn : Cr ratios of 1 : 7. Chemical composition, rod-like habit and d-spacings (Fig. 10a-d) indicate the occurrence of the mineral bracewellite (γ -CrO(OH)).

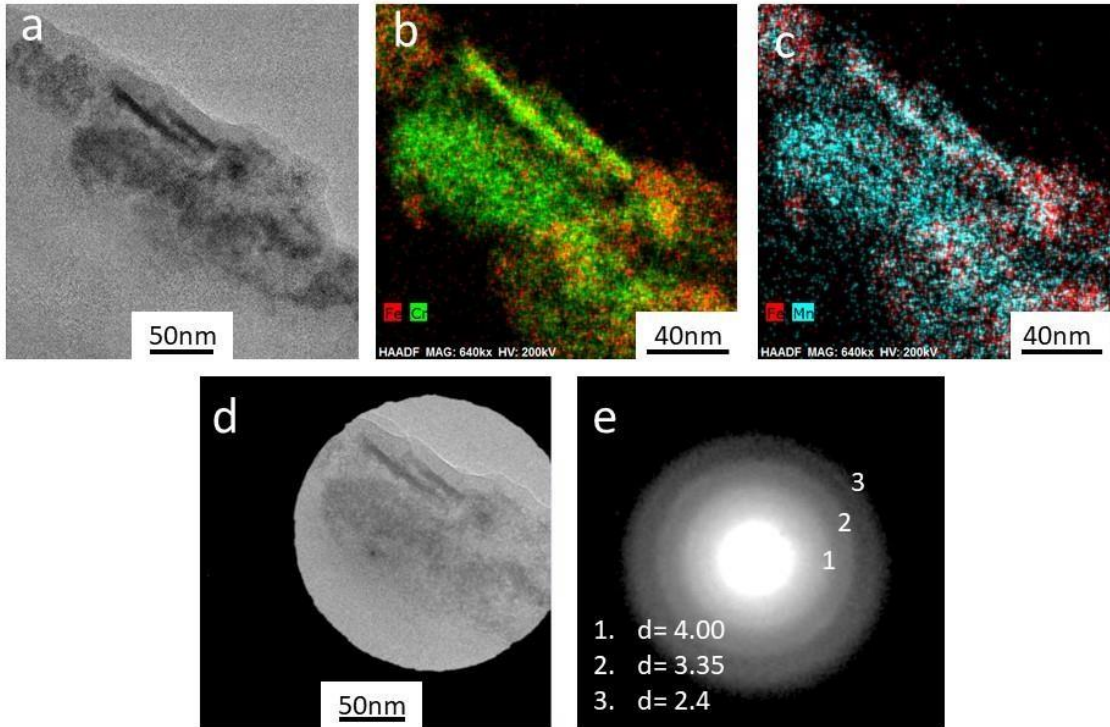


FIGURE 10. (a) TEM image and (b)-(c) STEM-EDS chemical maps for (b) Fe (red) and Cr (green) and (c) Fe (red) and Mn (blue) of an aggregate of chromite nanoparticles with a Cr-(hydr)oxide precipitate containing two parallel rods of bracewellite rods (γ -CrO(OH)); (d) Selected area diffraction pattern with characteristic d-spacings for bracewellite.

Figure 11a-d shows an amorphous Cr-hydroxide nanoparticle (green) formed in the suspension with the organic-rich soil (experiment 6). The nanoparticle is part of a larger aggregate containing hausmannite nanoparticles and an unidentified silicate (most likely a clay mineral with an Al : Si ratio of 1 : 1.5) (Fig. 11a, b). The Cr-hydroxide nanoparticle contains significant amounts of Mn with an average Mn : Cr ratios of 1 : 7. Although the nanoparticle is highly porous with etch pits of $d = 4 - 8$ nm, its outline resembles still those of a chromite cubooctahedron with almost equi-dimensions (120 nm x 100 nm). Along the [110] edge of the

(100) face of the former chromite nanoparticle occur two rods (60 nm x10 nm), which have grown parallel to the edge (Fig. 11a-c). High resolution TEM images and FFT pattern indicate the occurrence of lattice fringes with $d = 2.4 \text{ \AA}$ within the rods and in their surrounding matrix (Fig. 11d). The chemical distribution map for Cr (green), the rod-like habit and d-spacing suggest again the occurrence of bracewellite. The hausmannite nanoparticles in the aggregate are rounded and range from $d = 30$ to 100 nm . They are rimed by pockets of Fe-(hydr)oxide precipitates in which the Fe : Mn ratios can vary between 1 : 7 and 1 : 1 (in red in Fig. 11b).

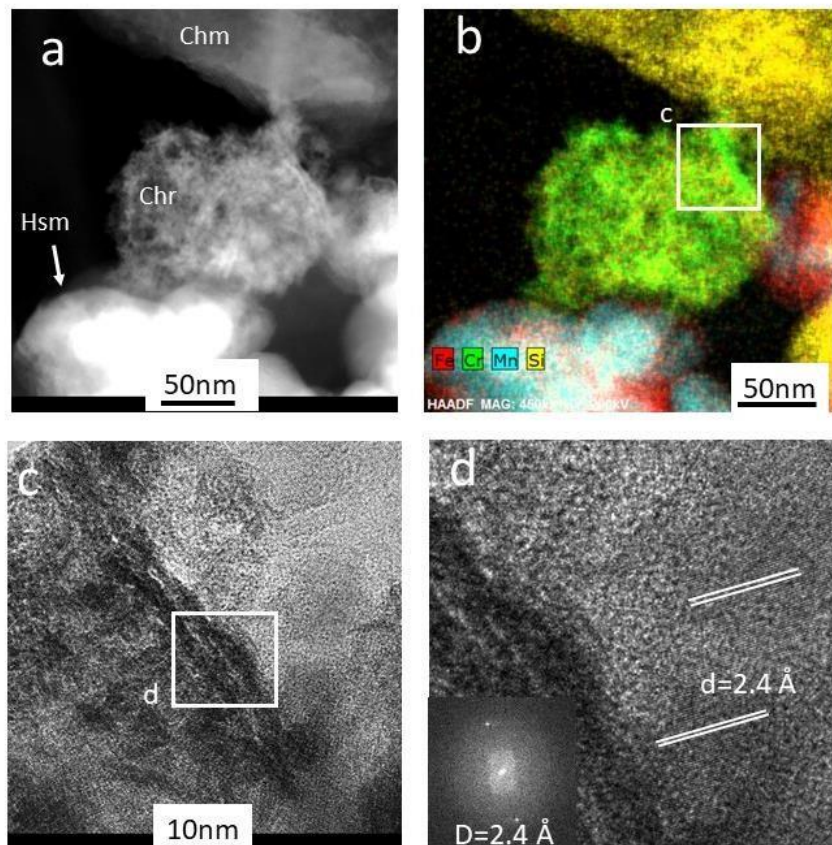


FIGURE 11. (a) STEM image and (b) STEM-EDS chemical distribution map for Fe (red), Cr (green), Mn (blue), Si (yellow) of a nanoparticle aggregate containing a Fe-depleted chromite nanoparticle and rods of bracewellite ($\gamma\text{-CrO(OH)}$); the area shown in (c) is indicated with a rectangle in (b); (c) TEM image of bracewellite rods, the area shown in (d) is indicated with a rectangle; (d) high resolution TEM image of bracewellite rods and FFT pattern indicating the occurrence of characteristic lattice fringes with d-spacings of $2.4 (111) \text{ \AA}$.

2.3.8 Interaction of chromite nanoparticles with chamosite and organic matter

One of the most prevalent interaction in the suspension containing chamosite particles is the attachment of chromite, Cr-(hydr)oxide and altered hausmannite nanoparticles on to surfaces of the chamosite particles (experiments 3 and 4). For example, Figures 12a-f depict the attachment of Cr-hydr(oxide)- and hausmannite nanoparticles on a highly altered chamosite particle, which is partially covered by Fe-(hydr)oxide precipitates (bright areas in Fig. 12a and indicated with the corresponding Fe : Mg ratios in Fig. 12b). Attached cubic and needle-like Mn-oxide nanoparticles (hausmannite and manganite, Fig. S2) and Fe-(hydr)oxides precipitates are in close association whereas the Cr-(hydr)oxide nanoparticles seem randomly distributed over the surface of chamosite grain (Fig. 12a-d.) High-resolution TEM studies and FFT-pattern indicate that parts of the attached Cr-(hydr)oxide nanoparticles are composed of grimaldiite (α -CrOOH).

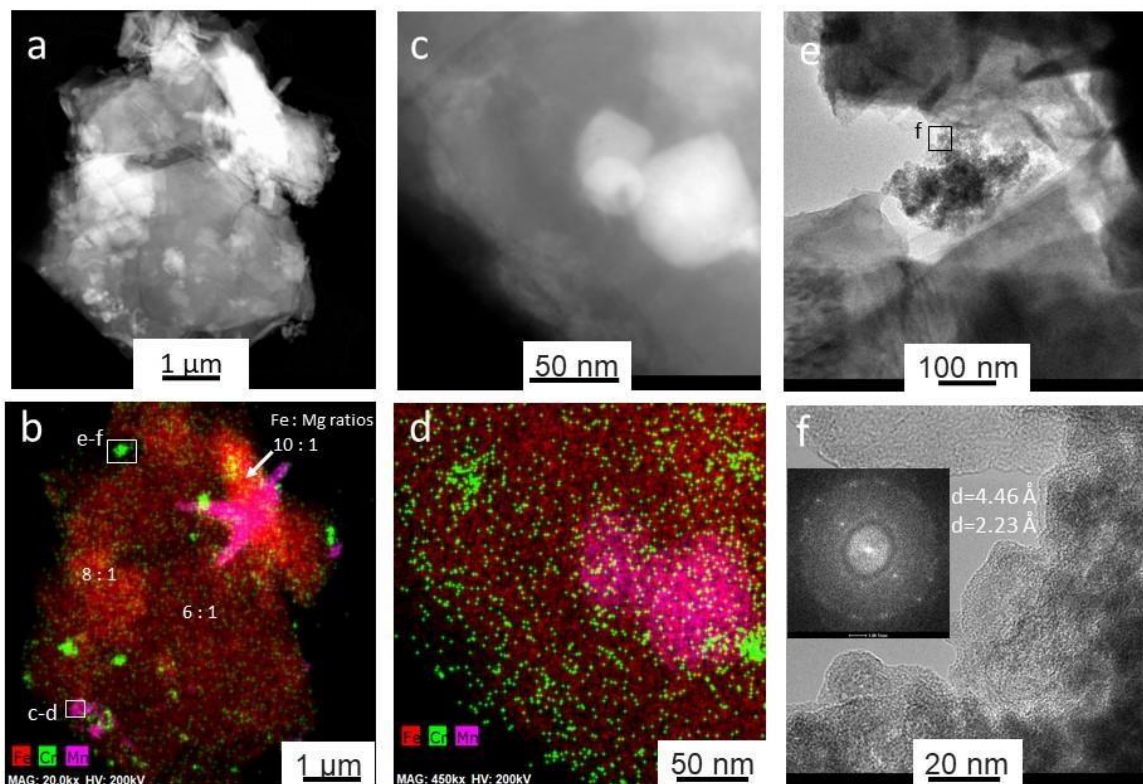


FIGURE 12. (a) STEM image and (b) STEM-EDS chemical map for Fe (green), Cr (red) and Mn (pink) of a chamosite grain from with attached Cr-(hydr)oxides and hausmannite nanoparticles; the areas shown in (c-d) and (e-f) are indicated with rectangles in (b); (c) High-resolution STEM image and STEM-EDS chemical map for Fe (green), Cr (red), Mn (pink) of the hausmannite nanoparticles attached to the chamosite grain; (e) TEM image and (f) high-resolution TEM image of a Cr-hydroxide grain attached to a chamosite grain, the area shown in (f) is indicated with a rectangle in (e); in inset of a FFT pattern indicates that the lattice fringes in (f) have characteristic d-spacings of grimaldiite (α -CrO(OH)).

One of the most prevalent interactions in the suspension with the organic-rich soils (experiment 5-6) is the interaction between chromite nanoparticles and organic colloids. Figure 13a-b shows for example an organic colloid with two attached or incorporated aggregates of chromite nanoparticle. Aggregate 1 is composed of small unaltered cubical nanoparticles of chromite (Fig. 13a). Aggregate 2 is highly altered and porous and contains only remains of a chromite nanoparticle. Large parts of the aggregate are enriched in Cr and Mn (i.e. depleted in Fe) whereby the distribution of Mn does not necessarily follow the outline of the aggregate.

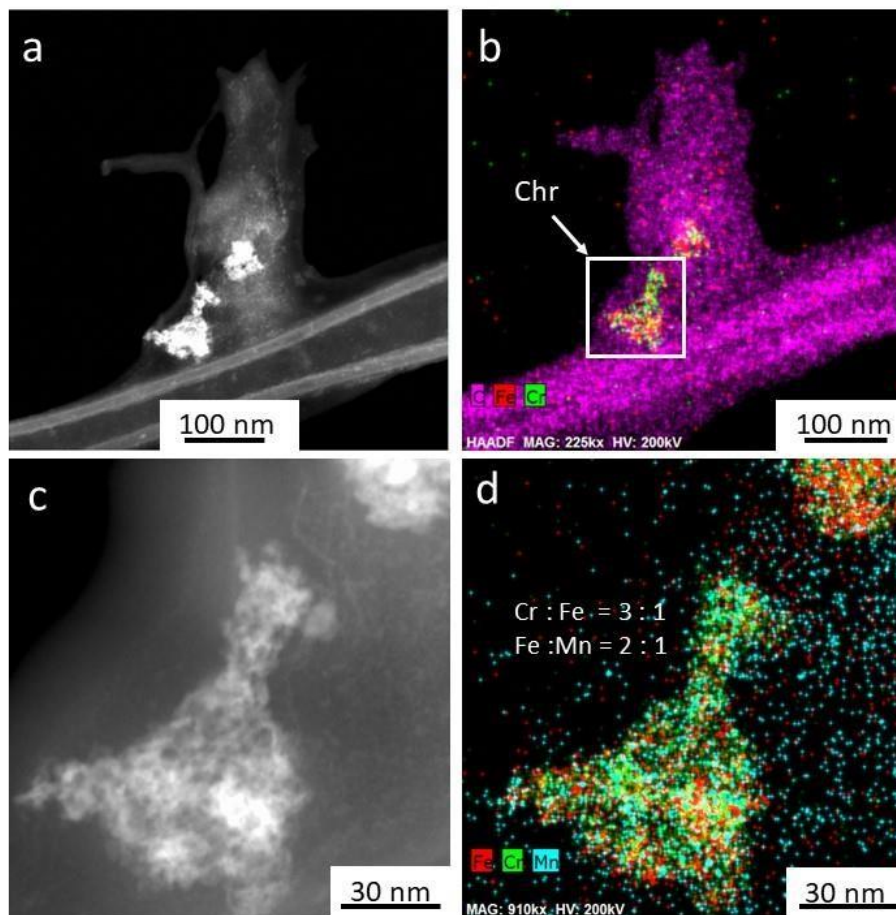


FIGURE 13. (a) and (c) STEM images and (b) and (d) STEM-EDS chemical distribution maps for (b) C (purple), Fe (red) and Cr (green) and (d) Fe (red), Cr (green), Mn (blue) of aggregates of chromite nanoparticles (chr) attached to larger organic matter (OM); the area shown in (c) and (d) is depicted by a rectangle in (b); aggregate 1 is composed of weakly-altered chromite cubes whereas aggregate 2 is highly altered and is depleted in Fe and enriched in Mn relative to aggregate 1.

2.3.9 Chemical composition of the suspensions after filtering

The Cr concentrations are in the $\mu\text{g kg}^{-1}$ range ($0.8\text{-}26.4 \mu\text{g kg}^{-1}$) and thus are much lower than the initial Cr concentration of $519.96 \text{ mg kg}^{-1}$ (Table 3). The Fe concentrations are below the detection limit in most of the suspensions due to the lower detection limit for the element. The concentrations for Mn are variable across the six experiments with the lowest and highest concentrations in the suspensions with the chamosite particles and organic-rich soils respectively

(Table 3). The concentrations of Cr³⁺ as well as Cr⁶⁺ in the solutions after adding NaCl (to promote aggregation and to desorb Cr-bearing aqueous species) and centrifugation are below the detection limit of 1 µgkg⁻¹ for the combination chromatography/Analytik Jena 820MS ICP-MS. The concentrations of Cr⁶⁺ in the solutions without any added NaCl were either below or slightly above the detection limit of 0.5 µg L⁻¹ for the combination chromatography/UV-VIS. The suspensions with the chamosite particles contained the highest concentrations of Cr⁶⁺ with 4.0 and 4.1 µg L⁻¹ (Table 3). The latter concentrations for Cr⁶⁺ and undetectable concentrations for Cr³⁺ (<1 [µgkg⁻¹]) indicate that the concentrations for Cr_{total} (Table 3) reflect predominantly the concentrations of Cr-bearing nanoparticles (< 450 nm) in each suspension.

TABLE 3. Chromium-, Fe- and Mn- concentrations in the suspensions (pH = 5) after the 9 months batch experiments (detection limits for Cr, Cr⁶⁺, Fe, Mn = 0.2, 0.5, 50, 50 and 1.0 [µgkg⁻¹]); the solutions were filtered (450 nm filter) but not centrifuged; Cr = chromite nanoparticles, Mn = hausmannite nanoparticles, Si = 10 gr chamosite, or = 10 gr organic rich soil; bdl = below detection limit

Experiment	Eh [V]	Cr [mgkg⁻¹]	Cr⁶⁺ [µgkg⁻¹]	Fe [mgkg⁻¹]	Mn [mgkg⁻¹]	P [mgkg⁻¹]
Cr-Mn = 1 : 1	0.43	0.0200	0.6	Bdl	19.11	2.903
Cr-Mn = 1 : 5	0.40	0.0028	<0.5	Bdl	15.66	4.681
Cr-Mn = 1 : 1, Si	0.41	0.0008	4.0	0.07	8.74	0.157
Cr-Mn = 1 : 5, Si	0.41	0.0014	4.1	Bdl	7.57	3.321
Cr-Mn = 1 : 1, Or	0.42	0.0300	0.6	0.01	25.40	0.125
Cr-Mn = 1 : 5, Or	0.43	0.0264	0.9	Bdl	38.32	0.040

2.4 Discussion

We will first develop a model for the formation of chromite nanoparticles during greenschist metamorphism of Cr-bearing silicates before addressing the stability of chromite nanoparticles in the leaching experiments, its interaction with hausmannite nanoparticles, clinocllore and organic matter and the potential formation of hexavalent Cr in Mn-rich soils of pH = 5.

2.4.1 Formation of chromite nanoparticles during greenschist metamorphism

The occurrence of chromite nanoparticles in clinocllore grains from the Mum and Alice June mine is in accord with the observations by Schindler et al. (2017) who identified chromite nanoparticles in Cr-rich silicates of chromitites from the Black Thor deposit and Mistake Mine. Additionally, Ruiz Cruz et al. (1999) show that submicron chromite particles can also form via exsolution processes (i.e. solid-state diffusional processes) during the replacement of olivine by talc during retrograde metamorphism.

Chromium (III) is commonly incorporated in the octahedral chains of pyroxenes, (Cameron and Papike; 1981; Huebner et al., 1976; Mével and Kienast, 1986; Roy and Roy, 1954). Similarly, single crystal X-ray diffraction data and polarized single crystal spectroscopy of Cr-rich clinocllore crystals with Cr \gg Fe indicate that Cr³⁺ is structurally incorporated into the octahedral layer of the layer silicate (Phillips et al. 1980; Platonov et al. 1996). However, electron microscopy and spectroscopy studies in combination with quantum mechanical calculations indicate that Cr³⁺ cannot substitute for Al³⁺ in the octahedral layers of boehmite, Al(OOH) (Chatterjee et al. 2016).

These contrary observations indicate that the speciation of Cr^{3+} (structurally incorporated versus nanoparticle) in clinocllore and other minerals with octahedral layers may depend on various environmental parameters such as the Cr / Fe ratio, the conditions during its formation and its paragenetic relationship with other minerals. Future spectroscopy studies in combination with TEM examinations may be able to quantify the proportions of Cr structurally incorporated in the octahedral layer of minerals of the chlorite group versus the presence of chromite nanoparticles in their interiors.

Chromite nanoparticles most likely form during the transformation of Mg-bearing pyroxenes and amphiboles into minerals of the chlorite and serpentinite group during greenschist metamorphism (Fyfe, 1959, Putnis 2009). During the metamorphic event, fluids infiltrate the pore space of the chromite-Mg-silicate rock and initiate the replacement of the Mg-silicate mineral by clinocllore and most likely chromite nanoparticles. A mineral replacement reaction is based on a coupled dissolution-reprecipitation process during which the porosity within the daughter mineral (clinocllore) promotes the mass exchange between the bulk fluid and the parent (pyroxene)-daughter interface (Putnis 2009). Hochella and Banfield (1995) show that pore spaces along the interfaces of clay minerals (daughters) and rock-forming silicates (parents) are commonly at the nanometer scale (nanopores). Nanoparticles have a higher surface energy than their micrometer-size counterparts and their formation in nanopores requires thus a higher degree of supersaturation in order to overcome their higher solubility (Pore Controlled Solubility (PCS) model, Emmanuel et al. 2010). A high degree of supersaturation with respect to the chromite nanoparticles occurs most likely during the release of Fe and Cr during dissolution of the pyroxene or amphibole (parent phases) and a possible influx of Cr^{3+} ions from the surrounding chromite into the nanopores of the clinocllore (daughter phase).

2.4.2 Release of chromite nanoparticles during the weathering of the Mg-silicates

TEM examinations of the colloidal fraction in the leachate could not unequivocally identify individual nanoparticles of chromite, most likely due to the centrifuge limited RPM and g-values. Chromite nanoparticles were instead identified in colloids composed of clinochlore and on the surface of an amorphous Al-hydroxide in the leachate of pH = 5 (Fig. 4b and c). The occurrence of attached and aggregated chromite nanoparticles on the surface of the Al-hydroxide colloid indicates the presence of nanoparticles in the colloidal fraction of the leachate. It seems unlikely that these nanoparticles originated from the breakdown of micrometer-sized chromite grains as they (1) have similar sizes as those observed in clinochlore and (2) contain only minor Mg whereas the latter grains have Fe : Mg ratios close to 1 : 1.

The Al-hydroxide colloid most likely formed during a coupled dissolution-reprecipitation processes during the alteration of the clinochlore as Al-hydroxides are common weathering products of Al-silicates at high-water rock ratios (Schellmann, 1994). The attachment of chromite nanoparticles on to the surface of the colloid can be explained with the point of zero charges for chromite ($\text{pH}_{\text{pzc}} = 6.1-6.8$) and $\text{Al}(\text{OH})_3$ ($\text{pH}_{\text{pzc}} = 8-9$) (Kosmulski, 2020; Sposito, 1995) and the fact that adsorbed silica species or Al-silicate surface coatings on oxides can reverse or neutralize their positive surface charge (Huang and Yang, 2020; Imae, 2017). Hence at the pH of the leachate (pH = 5), the surface of the Al-(hydroxide) colloid with adsorbed silica species/Al-silicate precipitates and the chromite nanoparticles had most likely neutral or opposite surface charges, which, according to the DLVO theory, promote the aggregation of nanoparticles (see below).

2.4.3 Aggregation of nanoparticles and their attachment onto mineral surfaces

The observed aggregation of chromite- and hausmannite- nanoparticles (Fig 6a-b) and their attachment to larger chlorite particles (Fig. 12a-f) can be explained with the Derjaguin-Landau-Verwey-Overbeek (DLVO) theory and extended Derjaguin-Landau-Verwey-Overbeek (XDLVO) theory. According to these theories, pH and activity of dissolved ions have a great influence on the surface charge and can either inhibit or promote aggregation. As the pH approaches the point of zero charge of a nanoparticle surface, electrostatic double layer repulsion decreases and aggregation is promoted by van der Waals attraction. Chromite and hausmannite have points of zero charge of around $pH_{pzc} = 6.0-6.5$ and $pH_{pzc} = 5.7$, respectively (Kosmulski, 2009; Rousseau, 1987) and their surface had thus slightly positive surface charges at $pH = 5$. This positive surface charge was neutralized in the suspension by the presence of negative counter ions such as phosphate and sulfate ions. STEM-EDS chemical distribution maps show indeed that negative charged phosphate counterions are attached to the surfaces of the chromite nanoparticles and hausmannite nanoparticles (Fig. 6a-b). These counter ions neutralised the slightly positive-charged EDL and van der Waals attractions became dominant and promoted the aggregation of the chromite and hausmannite nanoparticles (Fig. 6a-b).

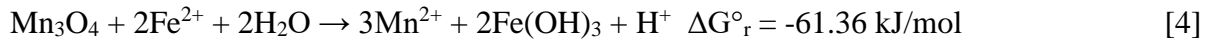
Chlorite has a point of zero charge of around $pH_{pzc} = 4.6$ and thus the chlorite grains had most likely a negatively charged surface at $pH = 5$. This allowed the attachment of the neutral to slightly positively charged chromite and hausmannite nanoparticles (Fig 12a-f). The typical point of zero charge for organic matter in soils is $pH_{pzc} = 2$ to 3 (Selinus and Alloway, 2005; Sparks, 2003) and their negatively charged surfaces at $pH = 5$ promoted also the attachment of the chromite nanoparticles (Fig. 13a-d).

2.4.4 Dissolution reprecipitation processes on the surface of hausmannite

The STEM/TEM studies indicate that the dissolution of chromite nanoparticles in the presence of hausmannite nanoparticle results in the formation of Cr- and Fe-hydroxide phases (Figs. 8-11). The corresponding dissolution reprecipitation reactions are most likely catalysed by the oxidation of Fe²⁺ by Mn³⁺ species which is thermodynamically favoured over the oxidation of Mn²⁺ by Fe³⁺ species:



Or in terms of (hydr)oxides:



The resulting Fe³⁺ (hydr)oxides (equation [4]) form a porous surface layer or fillings within the hausmannite nanoparticles (Figs. 8 and 9), which allowed the continuous oxidation of Fe²⁺ to Fe³⁺, the precipitation of Fe³⁺-phases and the reductive dissolution of the Mn-oxide. This continuous dissolution-reprecipitation process has been also observed by others (Schaefer et al., 2017), and can eventually result in the pseudomorphic replacement of a Mn- by Fe-oxide mineral (Golden et al. 1988). Similarly, the attachment of Mn-oxide nanoparticles on the surface of the chamosite crystals resulted in the formation Fe³⁺-(hydr)oxides most likely due to the oxidative dissolution of the underlying Fe²⁺-bearing sheet silicates (Fig. 12).

A mineral replacement requires that dissolution of the phase to be replaced (in this case a Mn oxide) and precipitation of the replacing phase (Fe-hydroxide) are closely coupled in space and time (Putnis 2009). The coupling of dissolution and precipitation may be recognized in Figure 9a-d, which show the formation of a Fe-hydroxide rim at the surfaces of highly etched hausmannite nanoparticles.

According to Putnis (2009), the coupling between the dissolution of the parent (hausmannite) and precipitation of the daughter (Fe-hydroxide) can be achieved when the controlling mechanism is the dissolution rate of the parent, and the activation energy barrier for the nucleation of the daughter is low. Although the type of Fe-(hydr)oxide was not unequivocally identified, the absence of diffraction spots in SAED pattern taken from Fe-rich precipitates suggests the occurrence of ferrihydrite, a nanocrystalline Fe^{3+} -hydroxide containing a high density of defects (vacancies, stacking faults), and variable amounts of H_2O and hydroxyl groups. The potential formation of ferrihydrite would be in accord with Ostwald's step rule which states that a metastable phase such as ferrihydrite forms prior to more crystalline phases such as hematite (Guo and Barnard, 2013, Aeppli et al, 2019). However, Navrotsky et al. (2008) showed that so-called metastable phases can be actually the thermodynamically most stable phases at the nanoscale as at this scale the surface energies of for example the Fe-hydroxide polymorphs goethite, lepidocrocite and akageneite are lower than those of hematite and maghemite (which are the most stable Fe-hydroxide phases at the bulk scale).

The formation of an Fe^{3+} -(hydr)oxide rim on the hausmannite nanoparticles most likely impacts the overall ability of Mn oxides to remain redox-active phases in environmental systems. Experimental studies showed for example that the production of Mn^{2+} during equations [3] and [4] decreases with time, suggesting that the Fe^{3+} -hydroxide layers partially passivate $\text{Mn}^{3+/4+}$ terminations on the surface of Mn oxides (Villinski et al., 2001).

The majority of the Cr-hydroxides nanoparticles formed during the long-term batch experiment lacks long-range (no diffraction spots in SAED pattern) (Figs. 8, 10-12). The initial formation of an amorphous $\text{CrO}(\text{OH})$ and subsequent transformation to the thermodynamically

more stable phases bracewellite and grimaldiite (which occur as nano-size crystals within the amorphous phase; Fig 10a-e, 11a-d) follows hereby again Ostwald's step rule.

There are three CrOOH polymorphs: α -CrOOH, grimaldiite, β -CrOOH, guyanaite and γ -CrOOH, bracewellite. These phases are rare and only occur in a few locations with merumite, a hydrated Cr-hydroxide ore discovered in Guyana, being the most prominent host of all three phases (Bracewell, 1946; Milton et al. 1976). Similar to this study, Shpachenko et al. (2006) identified bracewellite crystals grown in a matrix of an amorphous Cr-hydroxide.

2.4.5 Reaction pathways during the interaction of hausmannite and chromite nanoparticles

The observations above clearly indicate that the dissolution of chromite and hausmannite are triggered by the oxidation of Fe^{2+} to Fe^{3+} (and perhaps Cr^{3+} to Cr^{6+}) and reduction of Mn^{3+} to Mn^{2+} . The dissolution of these nanoparticles is accompanied by dissolution-precipitation processes which lead to the replacement of the Mn-oxide by a Fe-(hydr)oxide (Figs. 8 and 9) and the replacement of chromite by Cr-hydr(oxides) (Figs. 8, 10-12).

On the basis of changes in the oxidation rate of Cr^{3+} to Cr^{6+} in the presence of chromite and Mn-oxides, Oze (2007) proposed that the reaction pathway $\text{Cr}^{3+} \rightarrow \text{Cr}^{6+}$ involves dissolution of chromite and transport of Cr^{3+} to the Mn-oxide surface and its subsequent oxidation. The results above suggest that Fe^{2+} and Cr^{3+} adsorb to the surfaces of the Mn-oxides (some in form of attached chromite nanoparticles) and that a certain fraction of the adsorbed Cr^{3+} reprecipitates with the Fe^{3+} -hydroxides (Fig. 7b). They also suggest that a fraction of the Cr^{3+} remains on the surface of the chromite and reprecipitate in the form of a Cr-(hydr)oxide. Furthermore, minor amounts of Mn in the altered chromite suggest that Mn-species adsorb to the chromite surface

and coprecipitate with the Cr-hydroxides (Figs. 7b and 10c). These observations indicate that coupled adsorption-dissolution-precipitation processes on the surfaces of chromite and hausmannite nanoparticles promote their dissolution, the adsorption of Mn^{3+} and Fe^{2+} species and the subsequent reprecipitation of Mn-species with Cr^{3+} -hydroxides and Cr^{3+} -species with Fe^{3+} -hydroxides, respectively.

2.4.6 The composition of the suspensions after the long-term experiments

The concentrations of Cr, Fe and Mn in the leachate after the long-term batch experiment and filtering (450 nm pore size) are much lower than their initial concentrations (Table 3) and suggest that the majority of Cr, Fe and Mn occur in nanoparticle aggregates with $d > 450$ nm. This conclusion is in accord with the observed aggregates of chromite, hausmannite and chamosite nanoparticles (Figs. 6 and 8-13). However, the concentration of Cr and Mn in the leachates differ significantly between the six experiments: the lowest and the highest concentrations of Cr and Mn occur in the leachates with chamosite and organic rich soils, respectively. The higher concentrations of Cr and Mn in the solutions with organic matter can be either a result of (a) a lower degree of nanoparticles aggregation relative to the experiments without organic matter or (b) the enhanced complexation of Cr and Mn by dissolved organic matter (Dinu, 2013; Gustafsson et al., 2014). However, the latter scenario can be ruled out for Cr as its concentrations, after addition of a salt solution and centrifugation, were below the detection limit of the analytical technique ($1 \mu\text{gkg}^{-1}$).

A lower degree of nanoparticle aggregation in the suspension with organic matter may be explained with the presence of adsorbed dissolved organic matter (DOM) on the surfaces of the nanoparticles. Studies on the fate of natural colloids in the environment show that natural

colloids with a wide range of chemical compositions are often negatively charged due to adsorbed DOM species (Philippe and Schaumann, 2014). These DOM species are mainly humic substances which either neutralize positive-charged surfaces and thus induce aggregation or cause electrosteric stabilization and hinder aggregation of the colloids (Philippe and Schaumann, 2014). Hence, humic substances adsorbed on the positive charged surfaces of the hausmannite and chromite nanoparticles may have partially reversed their surface charges and subsequently lowered their degree of aggregation in the experiments with organic matter.

2.4.7 The formation of hexavalent Cr

Two distinct analytical approaches (chromatography + ICP-MS versus chromatography + UV-VIS) indicated that the concentrations of Cr^{6+} in all suspensions after the long-term batch experiments were very low with the highest concentration around $4 \mu\text{g kg}^{-1}$ (Table 3). At first sight, the low concentrations of Cr^{6+} seem to contradict observations that the highest oxidation rates for $\text{Cr}^{3+} \rightarrow \text{Cr}^{6+}$ occur in the presence of Mn^{3+} -bearing oxides (such as hausmannite) at $\text{pH} = 5$ (Weaver and Hochella, 2003). The low concentrations of Cr^{6+} also seem to contradict Oze et al. (2007) who conducted experiments demonstrating accelerated dissolution of chromite and subsequent oxidation of Cr^{3+} to Cr^{6+} in the presence of the Mn^{3+} bearing mineral birnessite. However, there are some key differences between this study and the previously mentioned studies:

- a) Contrary to the study conducted by Weaver and Hochella (2003), the experiments in this study contained reductants known to be capable of reducing Cr^{6+} to Cr^{3+} . These reductants were the Fe^{2+} -bearing minerals chamosite and chromite and oxidized functional surface terminations on organic matter.

- b) The micrometer-size chromites used by Oze et al. (2007) were actually magnesiochromites with the composition $(\text{Fe}_{0.46}\text{Mg}_{0.52}\text{Mn}_{0.02})(\text{Cr}_{0.61}\text{Al}_{0.29}\text{Fe}_{0.10})_2\text{O}_4$, whereas the synthesized chromite nanoparticles used in this study had the Fe-endmember composition FeCr_2O_4 (Fig. 5a, b). Although the total surface area of the chromite nanoparticles varied with the degree of aggregation of the chromite-hausmannitechamosite-organic matter particles, a higher number of Fe^{2+} surface sites were most likely present in the experiments of this study than those carried out by Oze et al. (2007). A high number of Fe^{2+} surface sites on the surface of the chromite nanoparticles in combination with Fe^{2+} - and organic-based reductive sites on the surfaces of the chamosite particles and organic material/DOM prevented the formation of significant concentrations of hexavalent Cr-species as
- a) The oxidation of Fe^{2+} to Fe^{3+} by Mn^{3+} ($E_0 = -1.069$ eV) is thermodynamically favoured over the oxidation of Cr^{3+} to Cr^{6+} ($E_0 = -0.0612\text{V}$) (see equation 3 and below)
- c) The oxidation of Fe^{2+} to Fe^{3+} resulted in the breakdown of the chromite structure and in the precipitation of (amorphous) Fe^{3+} - and Cr^{3+} -(hydr)oxides (Fig. 9a-d). The reprecipitation of an amorphous Cr^{3+} -hydroxide along the interface of the unaltered chromite nanoparticles may have been thermodynamically as well as kinetically favoured over the oxidation of Cr^{3+} to Cr^{6+} .
- d) Any Cr^{6+} formed through the reduction of Mn^{3+} to Mn^{2+} may have subsequently reduced by Fe^{2+} surface terminations on the surface of the chromite nanoparticles: $3\text{Mn}^{3+} + \text{Cr}^{3+} + 4\text{H}_2\text{O} \rightarrow 3\text{Mn}^{2+} + (\text{HCrO}_4)^- + 7\text{H}^+$; $\Delta G^\circ_r = -5.9$ kJ [5]
- $(\text{HCrO}_4)^- + 3\text{Fe}^{2+} + 7\text{H}^+ \rightarrow 3\text{Fe}^{3+} + \text{Cr}^{3+} + 4\text{H}_2\text{O}$; $\Delta G^\circ_r = -85.97$ kJ [6]

The higher concentrations of hexavalent Cr in the experiments with than without chamosite particles (experiments 3 + 4 versus 1 + 2) may be the result of the competitive adsorption of negative-charged chromate and silicate species (Zachara et al., 1987), which occur in higher concentrations in the former than latter experiments.

2.4.8 Recommendations for Future studies on chromite nanoparticles in the presence of Mn-oxides

The observations in this study show that the formation and occurrence of Cr^{6+} species in solutions containing chromite nanoparticles can be limited in complex mineralogical and geochemical systems, even in the presence of Mn^{3+} -oxides, due to the presence of adsorption sites on silicates, organic matter, Fe- and Cr^{3+} -hydroxides. A better understanding on the formation of Cr^{6+} species or their sequestration during the oxidative dissolution of chromite nanoparticles requires additional studies which should include:

1. Experiments containing chromite nanoparticles in simplified systems in the absence and presence of Mn-oxide particles at various pH values. Experiments without Mn-oxides are important for our understanding on the stability of chromite nanoparticles in soils of different pH value. TEM studies and chemical analyses for Cr^{6+} in solution should be carried out periodically over the course of the experiments in order to characterize particle interactions as well as the kinetics of the oxidative dissolution of chromite nanoparticles in the presence and absence of Mn-oxides. In addition to analysing for the concentration of Cr^{6+} , different Cr species in solution and adsorbed to mineral surface should be identified using chromatography, UV-VIS spectroscopy, X-ray Photoelectron Spectroscopy and EXAFS (Extended X-ray absorption fine

structure), respectively. These analytical techniques can unequivocally identify whether the oxidative dissolution of Fe-rich chromite leads indeed to the formation of Cr⁶⁺ species. Further studies can build upon these experiments by conducting similar experiments in more complex systems containing naturally occurring materials that occur in the environment surrounding Cr-rich rocks at the “Ring of Fire”.

2. Collection of soil and water samples from the surroundings at the “Ring of Fire” to identify the occurrence of chromite nanoparticles in an environmental setting. These samples should be collected in proximity to exposed weathered Cr-rich ultramafic rocks. In these samples, chromite nanoparticles most likely occur in weathering crusts on ultra-mafic rocks, such as dunite, peroxinite and peridotite found at the Black Thor chromite deposit at the “Ring of Fire”. In the case chromite nanoparticles are absent, studies should focus on the identification of Cr-bearing alteration products. The identity of these phases will allow the development of more robust chemical models for the environmental fate of Cr after weathering of Cr-rich ultramafic rocks.
3. Another study should focus on the occurrence of Mn-oxides in soils surrounding the “Ring of Fire”. Common Mn-oxide minerals in soils are lithiophorite, hollandite, and birnessite (Post, 1999)

2.5 Implications

The results of this study do not only confirm that chromite nanoparticles occur in Cr-rich silicates, but they also show that these nanoparticles persist through weathering of their host silicates at pH = 5 and can be released into the environment. These observations change our

understanding of the potential risks of Cr-bearing silicates in mine tailings and soils. The release of chromite nanoparticles as opposed to $\text{Cr}^{3+}_{(\text{aq})}$ species has a large impact on the fate of Cr in the environment as the behavior of nanoparticles is governed by surface reactions (Hochella et al., 2008).

This study gives for the first-time insight into mineralogical processes during the interaction of chromite and Mn-oxides nanoparticles. Common mineralogical features are

1. the aggregation of chromite and hausmannite nanoparticles, which is (a) promoted under near neutral pH conditions (slightly positive surface charges) and the presence of negatively-charged phosphate species and (b) partly inhibited by dissolved organic matter.
2. The dissolution of chromite and hausmannite nanoparticles and their (partial) replacement by Cr- and Fe-hydroxides is facilitated by adsorption-dissolution-precipitation processes. The latter processes involve the adsorption of Mn, Cr and Fe-species, the redox-controlled dissolution of the underlying mineral and the formation of porosity which allows a continuous mass exchange between the daughter-parent phases and the bulk solution.

The oxidation rate of Cr^{3+} to Cr^{6+} during dissolution of Cr-bearing silicates is in particular affected by the occurrence of chromite nanoparticles as they limit the availability of Cr^{3+} during the dissolution of the silicate (in comparison to structurally incorporated Cr^{3+}) and provide Fe^{2+} -surface sites as reductants for newly-formed hexavalent Cr-species. Additional soil constituents such as Fe-reducing bacteria, Fe^{2+} -bearing silicates (such as chamosite), Fe^{2+} -oxides (such as magnetite) and organic matter can also inhibit the oxidation of Cr^{3+} even in the presence of highly-reactive strong oxidants such as hausmannite nanoparticles (Hausladen and Fendorf,

2017 and this study). These observations indicate that chromite nanoparticles, *sensu stricto* FeCr_2O_4 , are less likely to contribute to the formation of environmental Cr^{6+} in their immediate surroundings. However, the detection of hexavalent Cr in natural waters in close proximity to serpentinite soils, its occurrence within micrometer-size soil pockets enriched in Mn (Fandeur et al., 2009) and its formation during the interaction of magnesiochromite and birnessite (Oze et al. 2007) indicates that its formation cannot be ruled out and requires most likely a lower abundance of Fe^{2+} in the system and the (partial) geochemical separation of Cr^{3+} from Fe^{2+} - and organicbearing soil and water components such as minerals and colloids.

References

- Aeppli, M., Kaegi, R., Kretzschmar, R., Voegelin, A., Hofstetter, T. B., and Sander, M. (2019) Electrochemical analysis of changes in iron oxide reducibility during abiotic ferrihydrite transformation into goethite and magnetite, *Environmental Science & Technology*, 53, 3568-3578.
- Aliofkhaezai, M., Ed. (2016) *Handbook of nanoparticles*, p.661-662. Springer, Switzerland.
- Ball, J. W., and Izbicki, J. A. (2004) Occurrence of hexavalent chromium in ground water in the western Mojave Desert, California. *Applied Geochemistry*, 19, 1123-1135.
- Barnhart, J. (1997) Occurrences, uses, and properties of chromium. *Regulatory toxicology and pharmacology*, 26, S3-S7.
- Bracewell, S. (1946) *The geology and mineral resources of British Guiana*. Daily Chronicle, Limited.
- Bulmer, C. E., and L. M. Lavkulich. (1994) Pedogenic and geochemical processes of ultramafic soils along a climatic gradient in southwestern British Columbia. *Canadian Journal of Soil Science*, 74, 165-177.
- Cameron, M., and Papike, J. J. (1981) Structural and chemical variations in pyroxenes. *American Mineralogist*, 66, 1-50.
- Cater, F.W., (1948) *Geological investigations of chromite in California, part III – Sierra Nevada* Chapter 1: Chromite deposits of Tulumne and Mariposa counties, California. U.S. Geological survey.
- Chatterjee, S., Conroy, M. A., Smith, F. N., Jung, H. J., Wang, Z., Peterson, R. A., Huq, A., Burt, D.G., Ilton, E.S., and Buck, E. C. (2016) Can Cr (III) substitute for Al (III) in the structure of boehmite? *RSC advances*, 6, 107628-107637.

- Dinu, M. I. (2013) Metals complexation with humic acids in surface water of different natural–climatic zones. *EDP Sciences*, 1, 32011.
- Edrissi, M., Hosseini, S. A., and Soleymani, M. (2011) Synthesis and characterisation of copper chromite nanoparticles using coprecipitation method. *Micro & Nano Letters*, 6, 836-839.
- Emmanuel, S., Ague, J.J., Walderhaug, O. (2010) Interfacial energy effects and the evolution of pore size distributions during quartz precipitation in sandstone. *Geochimica et Cosmochimica Acta*, 74, 3539–3552.
- Fandeur, D., Juillot, F., Morin, G., Olivi, L., Cognigni, A., Webb, S. M., Ambrosi, J., Fritsch, E. Guyot, F., and Brown, Jr, G. E. (2009) XANES evidence for oxidation of Cr (III) to Cr (VI) by Mn-oxides in a lateritic regolith developed on serpentized ultramafic rocks of New Caledonia. *Environmental Science & Technology*, 43, 7384-7390.
- Fendorf, S.E., and Zasoski, R.J. (1992) Chromium(III) oxidation by delta-MnO₂. I. Characterization. *Environmental Science & Technology*, 26, 79-85.
- Fendorf, S.E. (1995) Surface reactions of chromium in soils and waters. *Geoderma* 67, 55-71.
- Fendorf, S., Bird, D.K., and Coleman R.G. (2004) Chromium geochemistry in serpentized ultramafic rocks and serpentine soils from the Franciscan complex of California. *American Journal of Science*, 304, 67-101.
- Fulda, B., Voegelin, A., Maurer, F., Christl, I., and Kretzschmar, R. (2013) Copper redox transformation and complexation by reduced and oxidized soil humic acid. 1. X-ray absorption spectroscopy study. *Environmental Science & Technology*, 47, 10903-10911.
- Fyfe, W. S. (1959) *Metamorphic reactions and metamorphic facies* Vol. 73. Geological Society of America.

- Godgul, G., and Sahu, K.C. (1995) Chromium contamination from chromite mine. *Environmental Geology*, 25, 251-257.
- Golden, D. C., Chen, C. C., Dixon, J. B., and Tokashiki, Y. (1988) Pseudomorphic replacement of manganese oxides by iron oxide minerals. *Geoderma*, 42, 199-211.
- Guo, H., and Barnard, A. S. (2013) Naturally occurring iron oxide nanoparticles: morphology, surface chemistry and environmental stability. *Journal of Materials Chemistry A*, 1, 27-42.
- Gustafsson, J. P., Persson, I., Oromieh, A. G., van Schaik, J. W., Sjöstedt, C., and Kleja, D. B. (2014) Chromium (III) complexation to natural organic matter: mechanisms and modeling. *Environmental Science & Technology*, 48, 1753-1761.
- Hausladen, D. M., and Fendorf, S. (2017) Hexavalent chromium generation within naturally structured soils and sediments. *Environmental Science & Technology*, 51, 2058-2067.
- Hochella, M.F., and Banfield, J.F. (1995) Chemical weathering rates of silicate minerals- chapter 8. chemical weathering of silicates in nature: a microscopic perspective with theoretical considerations. *Reviews in Mineralogy and Geochemistry*, 31.
- Hochella, M. F., Moore, J. N., Putnis, C. V., Putnis, A., Kasama, T., and Eberl, D. D. (2005) Direct observation of heavy metal-mineral association from the Clark Fork River Superfund Complex: Implications for metal transport and bioavailability. *Geochimica et cosmochimica acta*, 69, 1651-1663.
- Hochella, M.F., Lower, K.S., Maurice, P.A., Penn, R.L., Sahai, N., Sparks, D.L., Twining, B.S. (2008) Nanominerals, mineral nanoparticles, and earths systems. *Science*, 319, 1631-1635.
- Hochella, M.F., Aruguete, D., Kim, B., and Madden, A.S. (2012) Naturally Occurring Inorganic Nanoparticles: General Assessment and a Global Budget for One of Earth's Last Unexplored Major Geochemical Components. *Nature's Nanostructures*, 1.

- Hotze, E. M., Phenrat, T., and Lowry, G. V. (2010) Nanoparticle aggregation: challenges to understanding transport and reactivity in the environment. *Journal of Environmental Quality*, 39, 1909-1924.
- Hseu, Z., Iizuka, Y. (2013) Pedogeochemical characteristics of chromite in a paddy soil derived from serpentinites. *Geoderma*, 202, 126-133.
- Huang, X., and Yang, G. (2020) Charge reversal and anion effects during adsorption of metal ions at clay surfaces: Mechanistic aspects and influence factors. *Chemical Physics*, 529, 110575.
- Huebner, J. S., Lipin, B. R., and Wiggins, L. B. (1976) Partitioning of chromium between silicate crystals and melts. *Lunar and Planetary Science Conference Proceedings*. 7, 1195-1220. Imae, T., Elsevier., Ed. (2017) *Nanolayer Research*. Elsevier Science.
- Jiang, W., Cai, Q., Xu, W., Yang, M., Cai, Y., Dionysiou, D.D., and O'Shea, K.E. (2014) Cr (VI) adsorption and reduction by humic acid coated on magnetite. *Environmental Science & Technology*, 48, 8078-8085.
- Kaptay, G. (2012) On the size and shape dependence of the solubility of nano-particles in solutions. *International Journal of Pharmaceutics*, 430, 253-257.
- Klein, F., Bach, W., and McCollom, T. M. (2013) Compositional controls on hydrogen generation during serpentinization of ultramafic rocks. *Lithos*, 178, 55-69.
- Kosmulski, M. (2009) *Surface charging and points of zero charge* (Vol. 145), 334 p. CRC press.
- Kosmulski, M. (2020) *The pH dependent surface charging and points of zero charge*. VIII. Update. *Advances in Colloid and Interface Science*, 275, 102064.
- Kumar, R., Rawat, K.S., and Mishra, A.K. (2012) Nanoparticles in the soil environment and their behaviour: An overview. *Journal of Applied and Natural Science*, 4, 310-324.

- Laarman, J. E. (2013) A detailed metallogenic study of the McFaulds Lake chromite deposits, northern Ontario. Ph.D. thesis, The University of Western Ontario, pp 494.
- Manning, A. H., Mills, C. T., Morrison, J. M., and Ball, L. B. (2015) Insights into controls on hexavalent chromium in groundwater provided by environmental tracers, Sacramento Valley, California, USA. *Applied Geochemistry*, 62, 186-199.
- Matulkova, I., Holec, P., Pacakova, B., Kubickova, S., Mantlikova, A., Plocek, J., Nemecek, I., Niznansky, D., and Vejpravova, J. (2015) On preparation of nanocrystalline chromites by co-precipitation and autocombustion methods. *Materials Science and Engineering: B*, 195, 66-73.
- Mével, C., & Kienast, J. R. (1986) Jadeite-kosmochlor solid solution and chromian sodic amphiboles in jadeitites and associated rocks from Tawmaw (Burma). *Bulletin de Minéralogie*, 109, 617-633.
- Milton, C., Appleman, D. E., Appleman, M. H., Chao, E.C., Cuttitta, F., Dinnin, J.I., Dwornik, E.J., Ingram, B.L., and Rose, H.J. (1976) Merumite- a Complex Assemblage of Chromium Minerals from Guyana. U.S. geological survey, Prof. Paper 887, 1–29
- Morrison, J. M., Goldhaber, M. B., Mills, C. T., Breit, G. N., Hooper, R. L., Holloway, J. M., Diehl, S.F., and Ranville, J. F. (2015) Weathering and transport of chromium and nickel from serpentinite in the Coast Range ophiolite to the Sacramento Valley, California, USA. *Applied Geochemistry*, 61, 72-86.
- Mosier, D.L., Singer, D.A., Moring, B.C., and Galloway, J.P. (2012) Podiform chromite deposits—database and grade and tonnage models. U.S. Geological Survey Scientific Investigations Report, 2012-5157.
- Navrotsky, A., Mazeina, L., and Majzlan, J. (2008) Size-driven structural and thermodynamic complexity in iron oxides. *Science*, 319, 1635-1638.

- Oliveira, H. (2012) Chromium as an environmental pollutant: insights on induced plant toxicity. *Journal of Botany*, vol. 2012
- Oze, C., Fendorf, S., Bird, D.K., and Coleman R.G. (2004) Chromium geochemistry in serpentinized ultramafic rocks and serpentine soils from the Franciscan complex of California. *American Journal of Science*, 304, 67-101.
- Oze, C., Bird, D. K., and Fendorf, S. (2007) Genesis of hexavalent chromium from natural sources in soil and groundwater. *Proceedings of the National Academy of Sciences*, 104, 6544-6549.
- Philippe, A., and Schaumann, G. E. (2014) Interactions of dissolved organic matter with natural and engineered inorganic colloids: a review. *Environmental Science & Technology*, 48, 8946-8962.
- Phillips, T. L., Loveless, J. K., and Bailey, S. W. (1980) Cr³⁺ coordination in chlorites: a structural study of ten chromian chlorites. *American Mineralogist*, 65, 112-122.
- Platonov, A. N., Langer, K., Andrut, M., and Calas, G. (1996) Cr³⁺ in phyllosilicates: influence of the nature of coordinating ligands and their next cationic neighbors on the crystal field parameters. *The Geochemical Society Special Publication*, 5, 41-48.
- Post, J. E. (1999) Manganese oxide minerals: Crystal structures and economic and environmental significance. *Proceedings of the National Academy of Sciences*, 96, 3447-3454.
- Putnis, A. (2009) Mineral replacement reactions. *Reviews in Mineralogy and Geochemistry*, 70, 87-124.
- Robles-Camacho, J., and Armienta, M. A. (2000) Natural chromium contamination of groundwater at Leon Valley, Mexico. *Journal of Geochemical Exploration*, 68, 167-181.
- Rousseau, R. W., Ed. (1987) *Handbook of Separation Process Technology*. John Wiley & Sons.

- Roy, D. M., and Roy, R. (1954) An experimental study of the formation and properties of synthetic serpentines and related layer silicate minerals. *American Mineralogist*, 39, 957-975.
- Ruiz Cruz, M. D., Puga, E., and Nieto, J. M. (1999) Silicate and oxide exsolution in pseudospinifex olivine from metaultramafic rocks of the Betic Ophiolitic Association; a TEM study. *American Mineralogist*, 84, 1915-1924.
- Schaefer, M. V., Handler, R. M., and Scherer, M. M. (2017) Fe (II) reduction of pyrolusite (β -MnO₂) and secondary mineral evolution. *Geochemical transactions*, 18, 7-18.
- Schellmann, W. (1994) Geochemical differentiation in laterite and bauxite formation. *Catena*, 21, 131-143.
- Schindler, M., Berti, D., and Hochella, M. F. (2017) Previously unknown mineral-nanomineral relationships with important environmental consequences: The case of chromium release from dissolving silicate minerals. *American Mineralogist*, 102, 2142-2145.
- Schindler, M., Lussier, A. J., Principe, E., and Mykytczuk, N. (2018) Dissolution mechanisms of chromitite: Understanding the release and fate of chromium in the environment. *American Mineralogist*, 103, 271-283.
- Schulte, R.F., Taylor, R.D., Piatak, N.M., and Seal, R.R. (2012) Stratiform chromite deposit model, chap. E of Mineral deposit models for resource assessment. U.S. Geological Survey Scientific Investigations Report, 2010–5070–E, 131 p.
- Scott, D. T., McKnight, D. M., Blunt-Harris, E. L., Kolesar, S. E., and Lovley, D. R. (1998) Quinone moieties act as electron acceptors in the reduction of humic substances by humics-reducing microorganisms. *Environmental Science & Technology*, 32, 2984-2989.
- Selinus O., and Alloway B. J. (2005) *Essentials of Medical Geology: Impacts of the Natural Environment on Public Health*, Elsevier Academic Press.

- Shpachenko, A. K., Sorokhtina, N. V., Chukanov, N. V., Gorshkov, A. N., and Sivtsov, A. V. (2006) Genesis and compositional characteristics of natural γ -CrOOH. *Geochemistry International*, 44, 681-689.
- Siebecker, M. G., Chaney, R. L., and Sparks, D. L. (2018) Natural speciation of nickel at the micrometer scale in serpentine (ultramafic) topsoils using microfocused X-ray fluorescence, diffraction, and absorption. *Geochemical Transactions*, 19, 14.
- Smith, C. A. S., Webb, K. T., Kenney, E., Anderson, A., and Kroetsch, D. (2011) Brunisolic soils of Canada: Genesis, distribution, and classification. *Canadian Journal of Soil Science*, 91, 695-717.
- Sparks, D. L. (2003) *Environmental soil chemistry*, 2nd ed., Elsevier Science & Technology Books.
- Sposito, G. (1995) *The environmental chemistry of aluminum*. CRC Press.
- Theng, B.K., and Yuan, G. (2008) Nanoparticles in the soil environment. *Elements*, 4, 395-399.
- U.S Geological Survey, (2020) *Mineral commodity summaries 2020*. U.S Geological survey, 200.
- Villinski, J. E., O'Day, P. A., Corley, T. L., and Conklin, M. H. (2001) In situ spectroscopic and solution analyses of the reductive dissolution of MnO₂ by Fe (II). *Environmental Science & Technology*, 35, 1157-1163.
- Weaver, R.M., and Hochella, M.F. (2003) The reactivity of seven Mn-oxides with Cr³⁺aq: A comparative analysis of a complex, environmentally important redox reaction. *American Mineralogist*, 88, 2016-2027
- Weston, R., and Shinkle, D. A. (2013) *Geology and stratigraphy of the Black Thor and Black Label chromite deposits, James Bay Lowlands, Ontario, Canada*. 12th SGA Biennial Meeting Proceedings.

Zachara, J. M., Girvin, D. C., Schmidt, R. L., and Resch, C. T. (1987) Chromate adsorption on amorphous iron oxyhydroxide in the presence of major groundwater ions. *Environmental Science & Technology*, 21, 589-594.

Appendix A. The following are tables and figures considered to be supplementary information.

Table S1: XRF analysis of the organic rich soil and chamosite powder used in the long-term batch experiments.

Oxide	Chamosite powder (wt%)	Organic rich soil (wt%)
Al ₂ O ₃	18.28	10.3
BaO	<0.004	0.049
CaO	0.536	1.33
Cr ₂ O ₃	0.023	0.006
Fe ₂ O ₃	44.95	3.12
K ₂ O	0.56	1.91
MgO	3.63	0.8
MnO	0.918	0.032
Na ₂ O	0.02	2.36
Nitrogen 105	0.07	1.9
P ₂ O ₅	0.011	0.108
SiO ₂	24.96	60.18
TiO ₂	1.91	0.43
Total	99.45	99.22
Total LOI	3.65	18.6

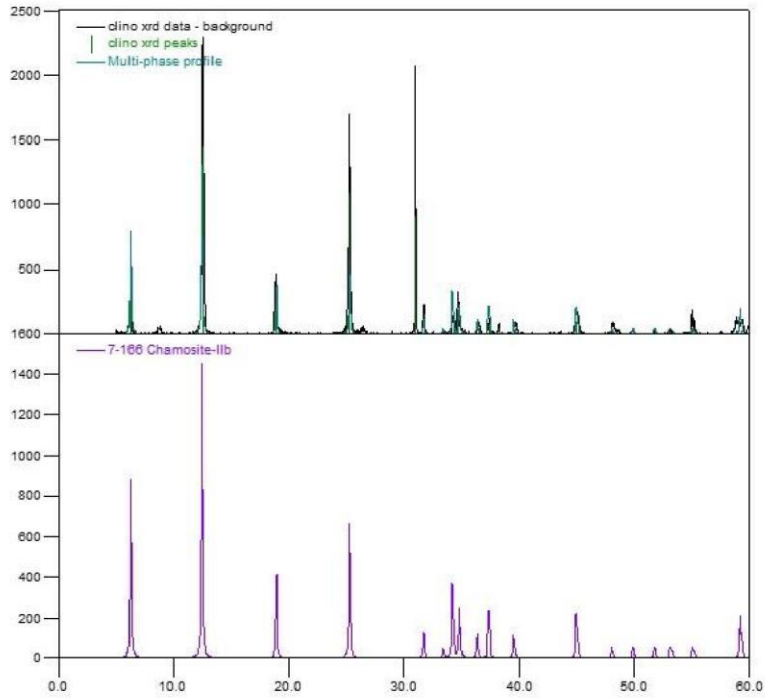


Fig. S1. X-ray diffraction pattern of the chamosite powder used in the long term batch experiments. The top pattern shows the observed diffraction pattern (black) and the pattern for chamosite (green) which is also shown on the bottom (violet).

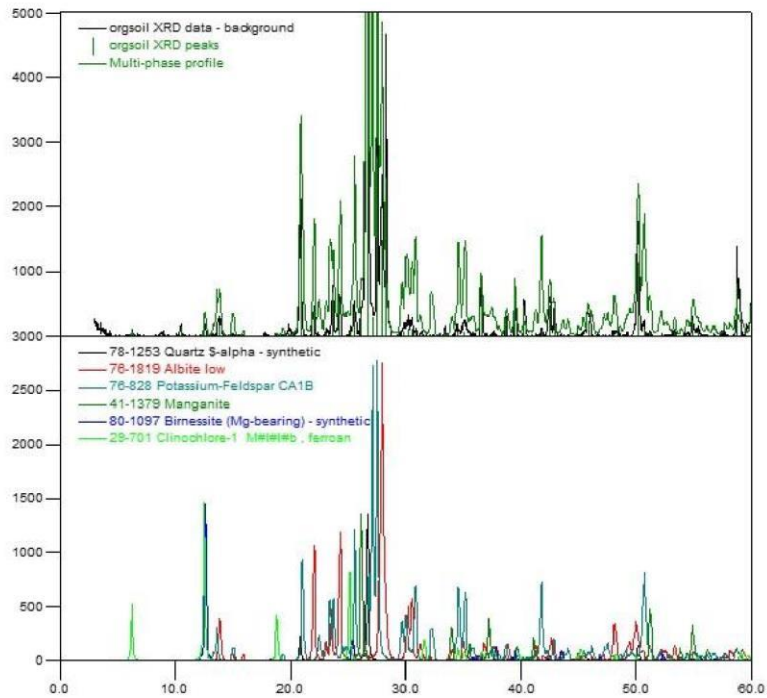


Fig. S3. X-ray diffraction pattern of the organic rich soils used in the long term batch experiments (black) and the sum of pattern of all identified phases (green). The individual pattern of all identified phases are shown at the bottom

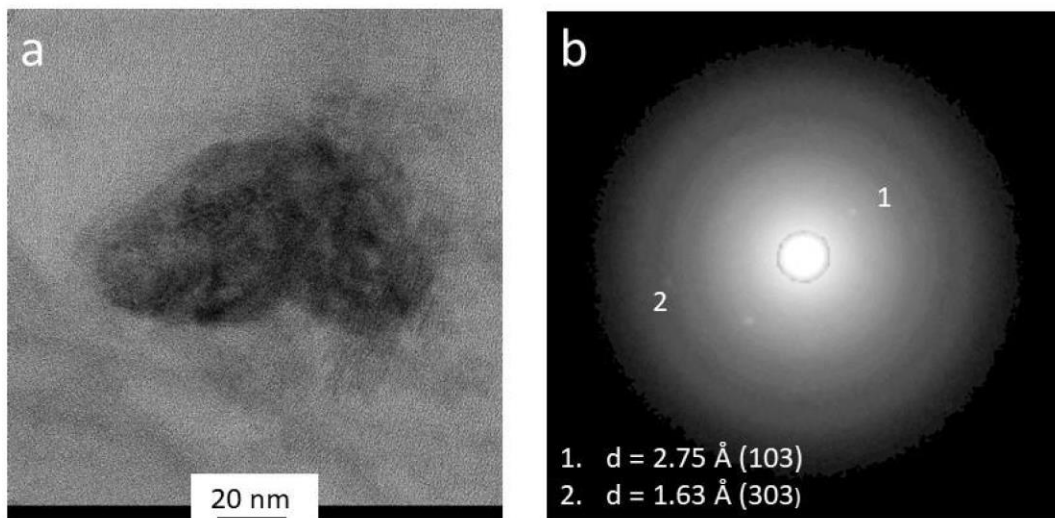


Fig. S4 (a) TEM image of two hausmannite nanoparticles and a highly altered chromite nanoparticle; (b) SAED pattern of the aggregate depicting diffraction spots corresponding to d-spacings characteristic of hausmannite

Appendix B. The following is a shorter version of the thesis that has been submitted to American Mineralogist.

Occurrence, release and alteration of chromite nanoparticles

Neal W. McClenaghan¹ and Michael Schindler^{2*}

1. Harquail School of Earth Sciences, Laurentian University, Sudbury, ON, P3E2C6,
Canada, e-mail: nmcclenaghan@laurentian.ca

2. Department of Geological Sciences, University of Manitoba, Winnipeg, MB, R3T2N2,
Canada

*Corresponding author: Michael.schindler@umanitoba.ca

Abstract

The discovery of chromite nanoparticles in silicates of ultramafic rocks may change our approach on the environmental risk assessment of mine waste associated with chromitite mining. This study shows for the first time that the alteration of Cr-rich silicates results in the release of chromite nanoparticles and that their interaction with oxidizing Mn-oxide nanoparticles causes the dissolution of chromite and Mn-oxide nanoparticles and the precipitation of Fe^{3+} - and Cr^{3+} hydroxides. During these processes, the formation of hexavalent Cr is suppressed by reductive Fe^{2+} -surface sites on chromite nanoparticles and Fe^{2+} -bearing silicates and by functional groups on organic matter. Transmission electron microscopy (TEM) in combination with ultramicrotomy, centrifugation, chromatography, ICP-MS and UV-VIS is used to characterize the occurrence of chromite nanoparticles, their release and alteration and the formation of hexavalent Cr aqueous species. TEM analysis of clinocllore grains from a chromitite sample of the Mum and Alice June claims ore deposits, California reconfirms the occurrence of chromite nanoparticles in Cr-rich silicates with chromitite. The chromite nanoparticles form in minerals of the chlorite and serpentinite group most likely during greenschist metamorphism via a coupled dissolution-reprecipitation process. Alteration of clinocllore grains containing chromite nanoparticles results in the release of the nanoparticles and their attachment to Al-silicate colloids. Chromite nanoparticles with the endmember composition FeCr_2O_4 are synthesized and their interaction with Mn-oxide nanoparticles (hausmannite, Mn_3O_4), Fe^{2+} -silicates (chamosite, $[(\text{Fe}_{3.9}\text{Mg}_{0.62}\text{Al}_{0.48})\text{Al}(\text{Si}_3\text{Al})\text{O}_{10}(\text{OH})_8]$) and organic matter is studied over a period of six to nine months in suspensions of $\text{pH} = 5$. The interaction of chromite and hausmannite nanoparticles is

facilitated by the aggregation of the nanoparticles and adsorption-dissolution-precipitation processes. Processes on the surfaces of the hausmannite nanoparticles involve the adsorption of Cr^{3+} and Fe^{2+} -species, the reductive dissolution of the substrate (reduction of Mn^{3+} to Mn^{2+} by Fe^{2+} species) and its replacement by amorphous or nanocrystalline Cr^{3+} -bearing Fe^{3+} -hydroxides. Processes on the surfaces of the chromite nanoparticles include the adsorption of Mn-species, the oxidative dissolution of the substrate (oxidation of Fe^{2+} and perhaps Cr^{3+} by Mn^{3+} species), its replacement by an amorphous or nanocrystalline Mn-bearing Cr^{3+} -hydroxide matrix and the formation of the Cr^{3+} -hydroxides bracewellite and grimaldite within the latter matrix. Analyses of the suspensions indicate only minor amounts of hexavalent Cr in the suspensions ($< 5 \mu\text{g kg}^{-1}$) suggesting that the majority of the released Cr species adsorb to mineral surfaces or reprecipitate with Cr- and Fe-hydroxide phases.

Introduction

The environmental fate and toxicity of Cr strongly depends on local redox and pH conditions as Cr³⁺-bearing minerals and aqueous species have commonly a lower solubility and mobility than their hexavalent toxic counterparts (Fendorf and Zasoski, 1992; Oliveira, 2012). The only known naturally occurring oxidizing agents of Cr³⁺ are Mn-oxides (Fendorf and Zasoski, 1992; Weaver and Hochella, 2003). Studies on the oxidation and reduction of Cr³⁺ and Cr⁶⁺ species in the presence and absence of Mn-oxides indicate that (1) Cr³⁺ oxidation to Cr⁶⁺ in the presence of Mn-oxides is rapid around pH = 5, but as Cr³⁺ concentration and pH increase the reaction become limited; (2) products of the oxidation of Cr³⁺ are commonly Mn²⁺ and Cr⁶⁺ which both do not limit the oxidation of Cr³⁺ through a shift in the redox potential or equilibrium; (3) Mn-oxides with the greatest and longest lasting oxidizing ability are those that contain both Mn³⁺ and Mn²⁺; (4) a higher proportion of Cr⁶⁺ forms in chromite-bearing serpentinite soils in the presence of birnessite, MnO₂; (5) Cr⁶⁺ can be reduced by various substances including organic matter, Fe²⁺ and sulfides and (6) the formation of Cr⁶⁺ can be suppressed by organic matter, even in the presence of Mn-oxides (Fendorf and Zasoski, 1992; Weaver and Hochella, 2003; Oze et al. 2007; Jiang et al., 2014; Hausladen and Fendorf 2017).

Serpentinite soils and laterites derived from ultramafic rocks are typically enriched in Cr (up to 80 600 mg/kg Cr) (Fendorf and Zasoski, 1992; Godgul and Sahu, 1995; Oze et al., 2004; Oze et al., 2007) and can contain hexavalent Cr⁶⁺ -species in the presence of Mn-oxides (Fandeur et al. 2009). Hexavalent Cr has been also detected in natural solutions in proximity to ophiolite complexes (Robles-Camacho and Armienta, 2000; Ball and Izbicki, 2004; Manning et al., 2015; Morrison et al., 2015).

The discovery of chromite nanoparticles within clinocllore and lizardite grains in chromitite ore from the Black Thor chromium deposit in central Canada and the Mistake mine, part of the Franciscan ophiolite complex, California, USA adds an unforeseen complexity to the mineralogy and geochemistry of Cr in serpentinite soils (Schindler et al. 2017, 2018) as the release of Cr during the weathering of the silicate minerals may occur in the form of chromite nanoparticles rather than Cr³⁺-aqueous species. In this case, the environmental fate of the element will be governed by the specific properties of the nanoparticles such as their reactivity, solubility and their abilities to aggregate or to adhere to mineral surfaces (Hochella et al., 2008; Teng and Yuan 2008; Hotze et al. 2010; Kumar, et al. 2012; Kaptay, 2012; Aliofkhazraei et al., 2016). The chromite nanoparticles in the silicates are 3-5 nm in diameter, occur in random orientations throughout the host silicates, are released during the weathering of their host silicates and most likely adhere to other nanoparticles present in solution (Schindler et al. 2017, 2018)

Objectives

An understanding of the fate of chromite nanoparticles in the environment requires knowledge about their interactions with other nanoparticles, mineral surfaces and redox-sensitive components in the soil environment such as Mn-oxides and organic matter. This interaction includes the pathways for the potential oxidation of Cr³⁺ and Fe²⁺ by Mn-oxides; *i.e.* do the corresponding redox processes require the aggregation of chromite and Mn-oxide nanoparticles or the adsorption of Mn- and Cr- aqueous species on the surfaces of the chromite and Mn-oxide nanoparticles, respectively?

Hence, the objectives of this study are to examine the occurrence and release of chromite nanoparticles and their interaction with Mn-oxides and other constituents most likely present in serpentinite soils. These goals will be achieved through conducting three distinct analytical and experimental approaches:

- IV. Scanning electron microscopy and a combination of ultra-microtoming, transmission electron microscopy (TEM) and Scanning TEM (STEM)-energy dispersive spectroscopy (EDS) in order to examine the abundance and distribution of Cr and chromite nanoparticles within silicates of chromitites from the Mum and Alice June claims in California (Fig. 1) and from locations other than those studied by Schindler et al. (2017, 2018) (Table 1).
- V. Leaching of a silicate-enriched fraction of a chromitite ore sample in solutions of pH = 2 and 5 in combination with TEM-STEM-EDS analyses in order to determine whether chromite nanoparticles are released upon the weathering of their silicate hosts;
- VI. Long-term (six to nine months) batch experiments in combination with TEM-STEM-EDS in order to characterize the alteration of synthesized chromite nanoparticles (endmember composition FeCr_2O_4) in the presence of other components most likely present in serpentinite soils such as hausmannite, Mn_3O_4 nanoparticles, chamosite (an Fe^{2+} -rich mineral of the chlorite group) and organic matter. These batch experiments will be conducted under pH conditions (pH = 5) similar to those in the eutric brunisolic soils surrounding the Black Thor chromium deposit which have contact pH-values of pH = 4.5 to 5.0 on the surface and pH > 5.5 at greater depth (Smith et al. 2011). The concentrations of Cr_{total} , Cr^{3+} , Cr^{6+} , Mn and Fe will be determined with ICP-MS and combinations of chromatography/ICP-MS and chromatography/UV-VIS.

Materials and Methods

The materials and method section can be found in the Supplementary data.

RESULTS

The results of the nano-mineralogical study on the Cr-rich clinochlore grains from the Mum and Alice June claims will be addressed first followed by those on the colloidal fractions in the suspension after (a) the leaching experiment of the silicate-enriched chromite ore sample and (b) six to nine months long-term batch experiments.

Silicate hosted chromite nanoparticles in the chromite ore from the Mum and Alice June claims

The Cr concentrations in the silicates of the chromitites ranges from < 0.2 to 4 at% (Table 1). The highest Cr concentrations occur in brucite and clinochlore grains in the sample from the Mum and Alice June claims, California, with Cr-concentrations ranging from 1-4 at% and 0.5-2 at%, respectively. In the latter sample, Cr is heterogeneously distributed within areas composed of brucite and clinochlore with the highest concentrations of Cr occurring along grain boundaries such as the boundary between brucite and quartz (Fig. 2a, b). Ultra-microtome sections cut from the clinochlore-brucite-quartz-chromite mineral assemblage resulted in the extraction of areas composed of clinochlore and chromite (Fig. 3a). These areas are characterized by long thin needles of clinchlore containing Mg-depleted chromite nanoparticles ($d = 3$ to 10 nm) along the boundaries of the clinochlore grains (Fig 3a-e).

Mineralogical studies of the silicate-enriched fraction of the chromitite ore sample and the colloidal fraction in the solution after the leaching experiment

After three months of leaching a silicate-enriched fraction of a chromitite ore sample at pH = 2 and 5, chromite grains are slightly chemically altered whereas the majority of the clinocllore grains is extensively etched (Fig. 4a). TEM examinations of the colloidal fraction in the leachates of pH = 2 and 5 did not unequivocally identify individual chromite nanoparticles on the TEM grids. Chromite nanoparticles were identified in clinocllore fragments and on the surface of an Al-rich colloid with an elemental Al : Si : Cr : Fe ratio of 10 : 2 : 1 : 1 and no detectable concentrations of Mg (Fig 4b-d).

Size and chemical composition of the synthesized chromite nanoparticles

TEM images of the synthesized chromite nanoparticles show the occurrence of individual nanoparticles and aggregates of nanoparticles (Fig. 5a). The chromite nanoparticles have diameters between 5 and 15 nm (Fig 5a, c) and are thus similar in size as the chromite nanoparticles in the Cr-rich silicates of the chromitites (Fig. 3d, Schindler et al. 2017). STEMEDS chemical distribution maps for Fe (red) and Cr (green) (Fig 5b) indicate a homogeneous distribution of both elements (average Cr : Fe atomic ratio: 1.8 : 1). High resolution TEM images and X-ray powder diffraction confirm the occurrence of predominantly chromite nanoparticles (Fig. 5c-e).

Chemical and mineralogical features of the colloidal fraction in the suspensions after 6 months of the long-term batch experiments

Different nanoparticle-adsorbed solute, nanoparticle-nanoparticle and nanoparticle-microparticle interactions occur in the suspensions. The most notable interaction is the aggregation of chromite and hausmannite nanoparticles (Fig. 6a-b). STEM chemical distribution maps suggest that this aggregation process occurred in the presence of adsorbed phosphate species (in red in Fig. 6b), which originated (most likely) from the KH_2PO_4 buffer added to the solution (see supplementary data).

Chemical trends among the nano- to micrometer-size particles

Scanning TEM-EDS chemical analyses of chromite nanoparticles or aggregates of chromite nanoparticles from the suspensions of all long-term batch experiments indicate that (altered) chromite nanoparticles are depleted in Fe and enriched in Mn relative to the synthesized chromite nanoparticles (Fig. 7a). Similarly, altered hausmannite nanoparticles are enriched in Fe and sometimes in Cr with maximum Fe : Mn and Cr : Mn ratios of 1 : 1 and 1 : 3, respectively (Fig 7b). Alterations also occur on the surfaces of the chamosite particles. These are commonly characterized by areas depleted in Mg and enriched in Al and Fe relative to the unaltered grains (Fig. 7c).

Textural, chemical and mineralogical features of chromite-hausmannite nanoparticle aggregates
Figure 8 shows a small aggregate of two altered hausmannite nanoparticles (see also Fig.

S4) and the remains of a chromite nanoparticle from the suspension with the organic-rich soil (experiment 5). The hausmannite nanoparticles are enriched in Fe (Mn : Fe ratio ~ 1 , Fig. 8b) and are highly altered with etch features at the lower nanometer range (dark spots in Fig. 8a). The

distribution of Fe is heterogeneous with high abundances of Fe occurring in cracks and on the surface of the hausmannite nanoparticles (in red in Fig. 8c). The latter nanoparticles contain also pockets enriched in Si (in yellow in Fig. 8d) which often overlap or are adjacent to areas enriched in Fe. The remains of a chromite nanoparticle occur below the plane of the hausmannite nanoparticles (Fig. 8a and in green in Fig. 8b) and are depleted in Fe relative to an unaltered chromite nanoparticle (Fe : Cr ratio = 1 : 5).

Large aggregates of hausmannite nanoparticles with attached chromite nanoparticles occur in all suspension. For example, a micrometer-size aggregate from the suspension with the chamosite powder (experiment 3) contains highly altered hausmannite nanoparticles enriched in Fe (max. Fe : Mn ratios of 1 : 1) along its surface and relatively unaltered nanoparticles in its interior (Fig. 9a-b). The altered hausmannite nanoparticles are rimmed by a nanometer-thick Fe(hydr)oxide precipitate without any apparent lattice fringes (Fig. 9c-d). Chromite nanoparticles attached to the aggregate are also rimmed by Fe-(hydr)oxides precipitates (Fig. 9c)

Textural, chemical and mineralogical features of secondary Cr-hydroxide phases

Chromium (hydr)oxide precipitates occur in all suspensions. For example, precipitates in the suspension with organic rich soil (experiment 6) are depleted in Fe and enriched in Mn relative to chromite (min. Fe : Cr ratios ~ 1 : 14; max. Mn : Cr ratios of 1 : 7; Fig. 10). The precipitates lack any apparent long- or short-range ordering (i.e. no diffraction spots in SAED pattern and lattice fringes) but their matrices contain rods of bracewellite (γ -CrO(OH)) (Fig. 10 and S5). In some cases, the morphology of the Cr-hydroxide precipitate resembles those of a chromite cubo-octahedron with almost equi-dimensions (120 nm x 100 nm) (Fig.10d, e).

Hausmannite nanoparticles associated with the Cr-hydroxides precipitates are commonly rimmed by pockets of Mn-bearing Fe-(hydr)oxide precipitates (Fe : Mn ratios vary from 1 : 7 to 1 : 1; in red in Fig. 10e).

Interaction of chromite nanoparticles with chamosite and organic matter

One of the most prevalent interaction in the suspension containing chamosite particles is the attachment of chromite, Cr-(hydr)oxide and altered hausmannite nanoparticles on surfaces of the chamosite particles (experiments 3 and 4). For example, Figures 11a-e depict the attachment of Cr-hydr(oxide)- and hausmannite nanoparticles on a highly altered chamosite particle, which is partially covered by Fe-(hydr)oxide precipitates (bright areas in Fig. 11a and indicated with the corresponding Fe : Mg ratios in Fig. 11b). Attached cubic and needle-like Mn-oxide nanoparticles (hausmannite and manganite, Fig. S2) and Fe-(hydr)oxides precipitates are in close association whereas the Cr-(hydr)oxide nanoparticles seem randomly distributed over the surface of chamosite grain (Fig. 11a-d). High-resolution TEM studies and FFT-pattern indicate that parts of the attached Cr-(hydr)oxide nanoparticles are composed of grimaldiite (α -CrOOH) (Fig. 11d, e).

One of the most prevalent interactions in the suspension with the organic-rich soils (experiments 5 and 6) is the interaction between chromite nanoparticles and organic colloids. Figure 11f shows for example an organic colloid with two attached or incorporated aggregates of (altered) chromite nanoparticle (labelled “1” and “2” in Fig. 11f). Aggregate 1 is composed of chemically unaltered nanoparticles of chromite (Fig. S6) whereas the nanoparticles in aggregate 2 are enriched in Cr and Mn and depleted in Fe with respect to the synthesized chromite nanoparticles (Fig. S6).

Chemical composition of the suspensions after 9 months of the long-term batch experiments

The pH values during all long-term batch experiments rose occasionally above pH = 5 and had to be re-adjusted mainly with a K-hydrogen phthalate solution (see above). The redox potential at this constant pH value varied only slightly in the range of Eh = 0.4 -0.43 V.

The Cr concentrations are in the $\mu\text{g kg}^{-1}$ range (0.8-26.4 μkg^{-1}) and thus are much lower than the initial Cr concentration of 519.96 mg kg^{-1} (Table 2). The Fe concentrations are below the detection limit in most of the suspensions due to the lower detection limit for the element. The concentrations for Mn are variable across the six experiments with the lowest and highest concentrations in the suspensions with the chamosite particles and organic-rich soils, respectively (Table 2). The concentrations of Cr^{3+} and Cr^{6+} in the suspensions are below the detection limit of 1 μgkg^{-1} when analysed with the combination chromatography/ICP-MS. The concentrations of Cr^{6+} in the suspensions are either below or slightly above the detection limit of 0.5 μgL^{-1} when analysed with the combination of chromatography/UV-VIS (Table 2). Here, the suspensions with the chamosite particles contain the highest concentrations of Cr^{6+} with 4.0 and 4.1 $\mu\text{g L}^{-1}$ (Table 2).

DISCUSSION

We will first develop a model for the formation of chromite nanoparticles during greenschist metamorphism of Cr-bearing silicates before addressing the stability of chromite nanoparticles in the leaching experiments, its interaction with hausmannite nanoparticles, clinocllore and organic matter and the potential formation of hexavalent Cr in Mn-rich soils of pH = 5.

Formation of chromite nanoparticles during greenschist metamorphism

The occurrence of chromite nanoparticles in clinocllore grains from the Mum and Alice June mine is in accord with the observations by Schindler et al. (2017) who identified chromite nanoparticles in Cr-rich silicates of chromitites from the Black Thor deposit and Mistake Mine. Additionally, Ruiz Cruz et al. (1999) show that submicron chromite particles can also form via exsolution processes (i.e. solid-state diffusional processes) during the replacement of olivine by talc during retrograde metamorphism.

Chromium (III) is commonly incorporated in the octahedral chains of pyroxenes, (Roy and Roy, 1954; Huebner et al., 1976; Cameron and Papike 1981; Mével and Kienast, 1986). Similarly, single crystal X-ray diffraction data and polarized single crystal spectroscopy of Cr-rich clinocllore crystals with $\text{Cr} \gg \text{Fe}$ indicate that Cr^{3+} is structurally incorporated into the octahedral layer of the layer silicate (Phillips et al. 1980; Platonov et al. 1996). Contrary, electron microscopy and spectroscopy studies in combination with quantum mechanical calculations indicate that Cr^{3+} does not substitute for Al^{3+} in the octahedral layers of boehmite, $\text{Al}(\text{OOH})$ (Chatterjee et al. 2016).

These contrary observations indicate that the speciation of Cr^{3+} (structurally incorporated versus nanoparticle) in clinocllore and other minerals with octahedral layers may depend on various environmental parameters such as the Cr / Fe ratio, the conditions during its formation and its paragenetic relationship with other minerals. Future spectroscopy studies in combination with TEM examinations may be able to quantify the proportions of Cr structurally incorporated in the octahedral layer of minerals of the chlorite group versus the presence of chromite nanoparticles in their interiors.

Chromite nanoparticles most likely form during the transformation of Mg-bearing pyroxenes and amphiboles into minerals of the chlorite and serpentinite group during greenschist metamorphism (Fyfe, 1959; Putnis 2009). During the metamorphic event, fluids infiltrate the pore space of the host rock and initiate the replacement of the former by the latter minerals. A mineral replacement reaction is based on a coupled dissolution-precipitation process during which the porosity within the daughter mineral (minerals of the chlorite and serpentinite group) promotes the mass exchange between the bulk fluid and the parent (pyroxene/amphibole)daughter interface (Putnis 2009). Porosity and the release of Fe and Cr during the dissolution of the parent phase facilitated most likely the formation of the chromite nanoparticles.

Release of chromite nanoparticles during the weathering of the Mg-silicates

TEM examinations of the colloidal fraction in the leachate could not unequivocally identify individual nanoparticles of chromite, most likely due to their particle size (max. $d = 15$ nm) and the centrifuge limited RPM and g-values (supplementary data). Chromite nanoparticles were instead identified in colloids composed of clinocllore and on the surface of an amorphous Al-hydroxide in the leachate of pH = 5 (Fig. 4b and c). The occurrence of attached and aggregated chromite nanoparticles on the surface of the Al-hydroxide colloid indicates the presence of nanoparticles in the colloidal fraction of the leachate. It seems unlikely that these nanoparticles originated from the breakdown of micrometer-sized chromite grains as they (1) have similar sizes as those observed in clinocllore and (2) contain only minor Mg whereas the micrometer-size chromite grains in the chromitite sample have Fe : Mg ratios close to 1 : 1.

The Al-hydroxide colloid formed most likely during the alteration of the clinocllore as Al-hydroxides are common weathering products of Al-silicates at high-water rock ratios (Schellmann, 1994).

Aggregation of nanoparticles and their attachment onto mineral surfaces

The observed aggregation of chromite- and hausmannite- nanoparticles (Fig 6a-b) and their attachment to larger chamosite and organic matter particles (Fig. 11) can be explained with the Derjaguin-Landau-Verwey-Overbeek (DLVO) theory and extended Derjaguin-Landau-Verwey-Overbeek (XDLVO) theory. According to these theories, pH and activity of dissolved ions have a great influence on the surface charge and can either inhibit or promote aggregation. As the pH approaches the point of zero charge of a nanoparticle surface, electrostatic double layer repulsion decreases and aggregation is promoted by van der Waals attraction. Chromite and hausmannite have points of zero charge of around $\text{pH}_{\text{pzc}} = 6.0-6.5$ and $\text{pH}_{\text{pzc}} = 5.7$, respectively (Rousseau, 1987; Kosmulski, 2009) and their surface had thus slightly positive surface charges at $\text{pH} = 5$. This positive surface charge was neutralized in the suspension by the presence of negative counter ions such as phosphate and sulfate ions (Fig. 6a-b). These counter ions neutralised the slightly positive-charged EDL and van der Waals attractions became dominant and promoted the aggregation of the chromite and hausmannite nanoparticles (Fig. 6a-b).

Chlorite has a point of zero charge of around $\text{pH}_{\text{pzc}} = 4.6$ and thus the chamosite grains had most likely a negative surface charge at $\text{pH} = 5$. This allowed the attachment of the positive-charged chromite and hausmannite nanoparticles (Fig 11a-e). The typical point of zero charge for organic matter in soils is $\text{pH}_{\text{pzc}} = 2$ to 3 (Selinus and Alloway, 2005; Sparks, 2003)

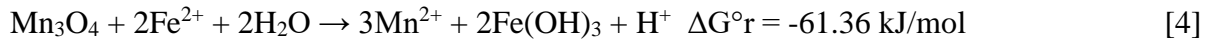
and the negative-charged surfaces of organic colloids at pH = 5 promoted also the attachment of the chromite nanoparticles (Fig. 11f).

Dissolution reprecipitation processes on the surface of hausmannite

The STEM/TEM studies indicate that the dissolution of chromite nanoparticles in the presence of hausmannite nanoparticle results in the formation of Cr- and Fe-hydroxide phases (Figs. 8-11). The corresponding dissolution-reprecipitation reactions are most likely catalysed by the oxidation of Fe²⁺ by Mn³⁺ species which is thermodynamically favoured over the oxidation of Mn²⁺ by Fe³⁺ species:



Or in terms of (hydr)oxides:



The resulting Fe³⁺ (hydr)oxides (equation [4]) form a porous surface layer or fillings within the hausmannite nanoparticles (Figs. 8 and 9), which allowed the continuous oxidation of Fe²⁺ to Fe³⁺, the precipitation of Fe³⁺-phases and the reductive dissolution of the Mn-oxide. This continuous dissolution-reprecipitation process has been also observed by others (Schaefer et al., 2017), and can eventually result in the pseudomorphic replacement of a Mn- by Fe-oxide mineral (Golden et al. 1988). Similarly, the attachment of Mn-oxide nanoparticles on the surface of the chamosite crystals resulted in the formation Fe³⁺-(hydr)oxides most likely due to the oxidative dissolution of the underlying Fe²⁺-bearing sheet silicates (Fig. 11a-c).

The mineralogical composition of the Fe-hydroxide rim on the surfaces of the hausmannite nanoparticles could not be unequivocally identified due to the absence of diffraction spots and lattice fringes. The precipitation of ferrihydrite seems however likely as it is commonly the first Fe-(hydr)oxide phase to precipitate from aqueous solution (Navrotsky et al. 2008; Guo and Barnard, 2013; Aeppli et al, 2019).

The formation of an Fe³⁺-(hydr)oxide rim on the surface of hausmannite nanoparticles most likely impacts the overall ability of Mn oxides to remain redox-active phases in environmental systems. Experimental studies showed for example that the production of Mn²⁺ during equations [3] and [4] decreases with time, suggesting that the Fe³⁺ -hydroxide layers partially passivate Mn^{3+/4+} terminations on the surface of Mn oxides (Villinski et al., 2001).

Large parts of the Cr-(hydr)oxides nanoparticles formed during the long-term batch experiment lack long-range (no diffraction spots in SAED pattern) (Fig. 10). The initial formation of an amorphous (or nanocrystalline) Cr-(hydr)oxide and its subsequent transformation to the thermodynamically more stable phases bracewellite and grimaldiite (which occur as nano-size crystals within the amorphous phase; Fig 10a-e, 11a-d) follows hereby Ostwald's step rule.

There are three CrOOH polymorphs: α -CrOOH, grimaldiite, β -CrOOH, guyanaite and γ CrOOH, bracewellite. These phases are rare and only occur in a few locations with merumite, a hydrated Cr-hydroxide ore discovered in Guyana, being the most prominent host of all three phases (Bracewell, 1946; Milton et al. 1976). Similar to this study, Shpachenko et al. (2006) identified bracewellite crystals grown in a matrix of an amorphous Cr-(hydr)oxide.

Reaction pathways during the interaction of hausmannite and chromite nanoparticles

The observations above clearly indicate that the dissolution of chromite and hausmannite are triggered by the oxidation of Fe^{2+} to Fe^{3+} (and perhaps Cr^{3+} to Cr^{6+}) and reduction of Mn^{3+} to Mn^{2+} . The dissolution of these nanoparticles is accompanied by dissolution-reprecipitation processes which can lead to the replacement of the Mn-oxide by a Fe-(hydr)oxide (Figs. 8 and 9) and the replacement of chromite by Cr-hydr(oxides) (Fig. 10d-e).

On the basis of changes in the oxidation rate of Cr^{3+} to Cr^{6+} in the presence of chromite and Mn-oxides, Oze (2007) proposed that the reaction pathway $\text{Cr}^{3+} \rightarrow \text{Cr}^{6+}$ involves dissolution of chromite and transport of Cr^{3+} to the Mn-oxide surface and its subsequent oxidation to Cr^{6+} .

The occurrence of Cr-rich Fe-(hydr)oxides (Figs.8 and 10-11) on the surface of the hausmannite nanoparticles suggest that Fe^{2+} and Cr^{3+} adsorb to the surfaces of the hausmannite nanoparticles (some in form of attached chromite nanoparticles) and that a fraction of the adsorbed Cr^{3+} reprecipitates with the Fe^{3+} -hydroxides during the reductive dissolution of the Mn-oxide substrate (Fig. 7b). The presence of Mn in altered chromite nanoparticles or Cr(hydr)oxide precipitates (Fig. 7a and 10c) suggests the co-precipitation of Mn species with Cr(hydr)oxides during the oxidative dissolution of the chromite nanoparticles. It also suggests that adsorbed Mn-species are actively involved in the dissolution process of chromite, perhaps in the form of adsorbed Mn^{3+} species promoting the oxidation of Fe^{2+} to Fe^{3+} and perhaps Cr^{3+} to Cr^{6+} on the surface of the chromite nanoparticles. Hence, adsorption-dissolution-reprecipitation processes may occur on the surfaces of both, chromite and hausmannite nanoparticles, and involve the adsorption of Mn^{3+} and Fe^{2+} species, the dissolution of their substrates and the subsequent reprecipitation of Mn- and Cr-species with Cr^{3+} - and Fe^{3+} -(hydr)oxides, respectively.

The composition of the suspensions after the long-term experiments

The concentrations of Cr, Fe and Mn in the leachate after the long-term batch experiment and filtering (450 nm pore size) are much lower (Table 2) than their initial concentrations (519.96 mg kg⁻¹, Table S1) and suggest that the majority of Cr, Fe and Mn occur in nanoparticle aggregates with $d > 450$ nm. This conclusion is in accord with the observed aggregates of chromite, hausmannite and chamosite nanoparticles (Figs. 6 and 8-11). However, the concentration of Cr and Mn in the leachates differ significantly between the six experiments with the lowest and the highest concentrations of Cr and Mn in the leachates with chamosite and organic rich soils, respectively (Table 2). The higher concentrations of Cr and Mn in the solutions with organic matter can be either a result of (a) a lower degree of nanoparticles aggregation relative to the experiments without organic matter or (b) the enhanced complexation of Cr and Mn by dissolved organic matter (Dinu, 2013; Gustafsson et al., 2014). However, the latter scenario can be ruled out for Cr as the concentrations for Cr³⁺aq and Cr⁶⁺aq after their chromatographic separation from the chromite nanoparticles were below or close to the detection limits of the ICP-MS and UV-VIS (1 µgkg⁻¹ and 0.5 µgkg⁻¹).

A lower degree of nanoparticle aggregation in the suspension with organic matter may be explained with the presence of adsorbed dissolved organic matter (DOM) on the surfaces of the nanoparticles. Studies on the fate of natural colloids in the environment show that natural colloids with a wide range of chemical compositions are often negative-charged due to adsorbed DOM species (Philippe and Schaumann, 2014). These DOM species are mainly humic substances which either neutralize positive-charged surfaces and thus induce aggregation or cause electrosteric stabilization and hinder aggregation of the colloids (Philippe and Schaumann, 2014). Hence, humic substances adsorbed on the positive-charged surfaces of the hausmannite

and chromite nanoparticles may have partially reversed their surface charges and subsequently lowered their degree of aggregation in the experiments with organic matter.

The formation of hexavalent Cr

Two distinct analytical approaches (chromatography + ICP-MS versus chromatography + UV-VIS) indicated that the concentrations of Cr^{6+} in all suspensions after the long-term batch experiments were very low with the highest concentration around $4 \mu\text{g kg}^{-1}$ (Table 2). At first sight, the low concentrations of Cr^{6+} seem to contradict observations that the highest oxidation rates for $\text{Cr}^{3+} \rightarrow \text{Cr}^{6+}$ occur in the presence of Mn^{3+} -bearing oxides (such as hausmannite) at $\text{pH} = 5$ (Weaver and Hochella, 2003). They also seem to contradict the results by Oze et al. (2007) which indicated accelerated dissolution of chromite and subsequent oxidation of Cr^{3+} to Cr^{6+} in the presence of the Mn^{3+} -bearing mineral birnessite. However, there are some key differences between this study and the latter studies:

- e) Contrary to the study conducted by Weaver and Hochella (2003), the experiments in this study contained reductants known to be capable of reducing Cr^{6+} to Cr^{3+} . These reductants were the Fe^{2+} -bearing minerals chamosite and chromite and oxidized surfaceterminations on organic matter.
- f) The micrometer-size chromites used by Oze et al. (2007) were actually magnesiochromites with the composition $(\text{Fe}_{0.46}\text{Mg}_{0.52}\text{Mn}_{0.02})(\text{Cr}_{0.61}\text{Al}_{0.29}\text{Fe}_{0.10})_2\text{O}_4$, whereas the synthesized chromite nanoparticles used in this study had the Fe-endmember composition FeCr_2O_4 (Fig. 5). Although the total surface area of the chromite nanoparticles varied with the degree of aggregation of the chromite-hausmannitechamosite-organic matter particles, a higher number of Fe^{2+} surface sites

were most likely present in the experiments of this study than those carried out by Oze et al. (2007).

Hence, a higher number of Fe^{2+} surface sites on the surface of the chromite nanoparticles in combination with Fe^{2+} - and organic-based reductive sites on the surfaces of the chamosite particles and organic material/DOM prevented most likely the formation of significant concentrations of hexavalent Cr-species. The higher concentrations of hexavalent Cr in the suspensions with than without chamosite particles (Table 2) were most likely the result of the presence of negative-charged silicate species in the suspensions with the chamosite particles. These silicate species competed with the negative-charged chromate species for adsorption sites on mineral surfaces (Zachara et al., 1987), which subsequently resulted in a higher amount of chromate species in solution.

IMPLICATIONS

The results of this study do not only confirm that chromite nanoparticles occur in Cr-rich silicates, but they also show that these nanoparticles persist through weathering of their host silicates at $\text{pH} = 5$ and can be thus released into the environment. These observations change our understanding of the potential risks of Cr-bearing silicates in mine tailings and soils. The release of chromite nanoparticles as opposed to $\text{Cr}^{3+}(\text{aq})$ species has a large impact on the fate of Cr in the environment as the behavior of nanoparticles is governed by surface reactions and nanoparticle-nanoparticle interactions (Hochella et al., 2008).

This study gives for the first-time insight into mineralogical processes during the interaction of chromite and Mn-oxides nanoparticles. Common mineralogical features are

3. the aggregation of chromite and hausmannite nanoparticles, which is (a) promoted under near neutral pH conditions and the presence of negative-charged phosphate species and (b) partly inhibited by dissolved organic matter.
4. The dissolution of chromite and hausmannite nanoparticles and their (partial) replacement by Cr- and Fe-hydroxides is facilitated by adsorption-dissolution-precipitation processes. The latter processes involve the adsorption of Mn, Cr and Fe-species, the redox-controlled dissolution of the underlying mineral and the formation of porosity which allows a continuous mass exchange between the daughter-parent phases and the bulk solution.

The oxidation rate of Cr^{3+} to Cr^{6+} during dissolution of Cr-bearing silicates is in particular affected by the occurrence of chromite nanoparticles as they limit the availability of Cr^{3+} during the dissolution of the silicate (in comparison to structurally incorporated Cr^{3+}) and provide Fe^{2+} -surface sites as reductants for newly-formed hexavalent Cr-species. Additional soil constituents such as Fe-reducing bacteria, Fe^{2+} -bearing silicates (such as chamosite), Fe^{2+} -oxides (such as magnetite) and organic matter can also inhibit the oxidation of Cr^{3+} even in the presence of strong oxidants such as hausmannite nanoparticles (in accord with the study by Hausladen and Fendorf, 2017). These observations indicate that chromite nanoparticles, *sensu stricto* FeCr_2O_4 , are less likely to contribute to the formation of environmental Cr^{6+} in their immediate surroundings. However, the detection of hexavalent Cr in natural waters in close proximity to serpentinite soils, its occurrence within micrometer-size soil pockets enriched in Mn (Fandeur et al., 2009) and its formation during the interaction of magnesiochromite and birnessite (Oze et al. 2007) indicates that its formation cannot be ruled out and requires most likely a lower abundance

of Fe²⁺ in the system and the (partial) geochemical separation of Cr³⁺ from Fe²⁺- and organicbearing soil and water components such as minerals and colloids.

ACKNOWLEDGEMENTS

This project was supported by the Best of Science award # ESSD-BIS201617-15 of the Ministry of the Environment, Conservation and Parks, Ontario, Canada to MS. We would like to thank Graeme Spiers for his continuous support of the project, Joy Gray Munroe and Pedro Jugo for their assistance with the synthesis of the chromite nanoparticles, M.B. McClenaghan for her comments of an earlier version of the MS, Abdul Khan at the Manitoba Institute of Materials for his assistance with the TEM studies and the MECP laboratories in Etobicoke and especially Teresa Switzer and Taddese Godeto for their assistance with the chemical analyses.

References

- Aeppli, M., Kaegi, R., Kretzschmar, R., Voegelin, A., Hofstetter, T. B., and Sander, M. (2019) Electrochemical analysis of changes in iron oxide reducibility during abiotic ferrihydrite transformation into goethite and magnetite, *Environmental Science & Technology*, 53, 3568-3578.
- Aliofkhazraei, M., Ed. (2016) *Handbook of nanoparticles*, p.661-662. Springer, Switzerland.
- Ball, J. W., and Izbicki, J. A. (2004) Occurrence of hexavalent chromium in ground water in the western Mojave Desert, California. *Applied Geochemistry*, 19, 1123-1135.
- Bracewell, S. (1946). *The geology and mineral resources of British Guiana*. Daily Chronicle, Limited.
- Cameron, M., and Papike, J. J. (1981) Structural and chemical variations in pyroxenes. *American*

- Mineralogist, 66, 1-50.
- Chatterjee, S., Conroy, M. A., Smith, F. N., Jung, H. J., Wang, Z., Peterson, R. A., Huq, A., Burt, D.G., Ilton, E.S., and Buck, E. C. (2016) Can Cr (III) substitute for Al (III) in the structure of boehmite? RSC advances, 6, 107628-107637.
- Dinu, M. I. (2013) Metals complexation with humic acids in surface water of different natural-climatic zones. EDP Sciences, 1, 32011.
- Fandeur, D., Juillot, F., Morin, G., Olivi, L., Cognigni, A., Webb, S. M., Ambrosi, J., Fritsch, E. Guyot, F., and Brown, Jr, G. E. (2009). XANES evidence for oxidation of Cr (III) to Cr (VI) by Mn-oxides in a lateritic regolith developed on serpentinized ultramafic rocks of New Caledonia. Environmental Science & Technology, 43, 7384-7390.
- 10903-10911.
- Fyfe, W. S. (1959) Metamorphic reactions and metamorphic facies Vol. 73. Geological Society of America.
- Godgul, G., and Sahu, K.C. (1995) Chromium contamination from chromite mine. Environmental Geology, 25, 251-257.
- Golden, D. C., Chen, C. C., Dixon, J. B., and Tokashiki, Y. (1988) Pseudomorphic replacement of manganese oxides by iron oxide minerals. Geoderma, 42, 199-211.
- Guo, H., and Barnard, A. S. (2013) Naturally occurring iron oxide nanoparticles: morphology, surface chemistry and environmental stability. Journal of Materials Chemistry A, 1, 27-42.
- Gustafsson, J. P., Persson, I., Oromieh, A. G., van Schaik, J. W., Sjöstedt, C., and Kleja, D. B. (2014) Chromium (III) complexation to natural organic matter: mechanisms and modeling. Environmental Science & Technology, 48, 1753-1761.
- Hausladen, D. M., and Fendorf, S. (2017) Hexavalent chromium generation within naturally structured soils and sediments. Environmental Science & Technology, 51, 2058-2067.

- Hochella, M.F., Lower, K.S., Maurice, P.A., Penn, R.L., Sahai, N., Sparks, D.L., Twining, B.S. (2008) Nanominerals, mineral nanoparticles, and earths systems. *Science*, 319, 1631-1635.
- Hotze, E. M., Phenrat, T., and Lowry, G. V. (2010) Nanoparticle aggregation: challenges to understanding transport and reactivity in the environment. *Journal of Environmental Quality*, 39, 1909-1924.
- Huebner, J. S., Lipin, B. R., and Wiggins, L. B. (1976) Partitioning of chromium between silicate crystals and melts. *Lunar and Planetary Science Conference Proceedings*. 7, 1195-1220.
- Jiang, W., Cai, Q., Xu, W., Yang, M., Cai, Y., Dionysiou, D.D., and O'Shea, K.E. (2014) Cr (VI) adsorption and reduction by humic acid coated on magnetite. *Environmental Science & Technology*, 48, 8078-8085.
- Kaptay, G. (2012) On the size and shape dependence of the solubility of nano-particles in solutions. *International Journal of Pharmaceutics*, 430, 253-257.
- Kumar, R., Rawat, K.S., and Mishra, A.K. (2012) Nanoparticles in the soil environment and their behaviour: An overview. *Journal of Applied and Natural Science*, 4, 310-324.
- Manning, A. H., Mills, C. T., Morrison, J. M., and Ball, L. B. (2015) Insights into controls on hexavalent chromium in groundwater provided by environmental tracers, Sacramento Valley, California, USA. *Applied Geochemistry*, 62, 186-199.
- Mével, C., & Kienast, J. R. (1986) Jadeite-kosmochlor solid solution and chromian sodic amphiboles in jadeitites and associated rocks from Tawmaw (Burma). *Bulletin de Minéralogie*, 109, 617-633.
- Milton, C., Appleman, D. E., Appleman, M. H., Chao, E.C., Cuttitta, F., Dinnin, J.I., Dwornik, E.J., Ingram, B.L., and Rose, H.J. (1976) Merumite- a Complex Assemblage of Chromium Minerals from Guyana. U.S. geological survey, Prof. Paper 887, 1-29
- Morrison, J. M., Goldhaber, M. B., Mills, C. T., Breit, G. N., Hooper, R. L., Holloway, J. M.,

- Diehl, S.F., and Ranville, J. F. (2015) Weathering and transport of chromium and nickel from serpentinite in the Coast Range ophiolite to the Sacramento Valley, California, USA. *Applied Geochemistry*, 61, 72-86.
- Navrotsky, A., Mazeina, L., and Majzlan, J. (2008). Size-driven structural and thermodynamic complexity in iron oxides. *Science*, 319, 1635-1638.
- Oliveira, H. (2012) Chromium as an environmental pollutant: insights on induced plant toxicity. *Journal of Botany*, vol. 2012
- Oze, C., Fendorf, S., Bird, D.K., and Coleman R.G. (2004) Chromium geochemistry in serpentinitized ultramafic rocks and serpentine soils from the Franciscan complex of California. *American Journal of Science*, 304, 67-101.
- Oze, C., Bird, D. K., and Fendorf, S. (2007) Genesis of hexavalent chromium from natural sources in soil and groundwater. *Proceedings of the National Academy of Sciences*, 104, 6544-6549.
- Philippe, A., and Schaumann, G. E. (2014) Interactions of dissolved organic matter with natural and engineered inorganic colloids: a review. *Environmental Science & Technology*, 48, 8946-8962.
- Phillips, T. L., Loveless, J. K., and Bailey, S. W. (1980). Cr³⁺ coordination in chlorites: a structural study of ten chromian chlorites. *American Mineralogist*, 65, 112-122.
- Platonov, A. N., Langer, K., Andrut, M., and Calas, G. (1996). Cr³⁺ in phyllosilicates: influence of the nature of coordinating ligands and their next cationic neighbors on the crystal field parameters. *The Geochemical Society Special Publication*, 5, 41-48.
- Putnis, A. (2009). Mineral replacement reactions. *Reviews in Mineralogy and Geochemistry*, 70, 87-124.

- Robles-Camacho, J., and Armienta, M. A. (2000) Natural chromium contamination of groundwater at Leon Valley, Mexico. *Journal of Geochemical Exploration*, 68, 167-181.
- Rousseau, R. W., Ed. (1987). *Handbook of Separation Process Technology*. John Wiley & Sons.
- Roy, D. M., and Roy, R. (1954). An experimental study of the formation and properties of synthetic serpentines and related layer silicate minerals. *American Mineralogist*, 39, 957-975.
- Ruiz Cruz, M. D., Puga, E., and Nieto, J. M. (1999) Silicate and oxide exsolution in pseudospinifex olivine from metaultramafic rocks of the Betic Ophiolitic Association; a TEM study. *American Mineralogist*, 84, 1915-1924.
- Schaefer, M. V., Handler, R. M., and Scherer, M. M. (2017) Fe (II) reduction of pyrolusite (βMnO_2) and secondary mineral evolution. *Geochemical transactions*, 18, 7-18.
- Schellmann, W. (1994) Geochemical differentiation in laterite and bauxite formation. *Catena*, 21, 131-143.
- Schindler, M., Berti, D., and Hochella, M. F. (2017). Previously unknown mineral-nanomineral relationships with important environmental consequences: The case of chromium release from dissolving silicate minerals. *American Mineralogist*, 102, 2142-2145.
- Schindler, M., Lussier, A. J., Principe, E., and Mykytczuk, N. (2018) Dissolution mechanisms of chromitite: Understanding the release and fate of chromium in the environment. *American Mineralogist*, 103, 271-283.
- Selinus O., and Alloway B. J. (2005) *Essentials of Medical Geology: Impacts of the Natural Environment on Public Health*, Elsevier Academic Press.
- Shpachenko, A. K., Sorokhtina, N. V., Chukanov, N. V., Gorshkov, A. N., and Sivtsov, A. V. (2006) Genesis and compositional characteristics of natural $\gamma\text{-CrOOH}$. *Geochemistry International*, 44, 681-689.

- Smith, C. A. S., Webb, K. T., Kenney, E., Anderson, A., and Kroetsch, D. (2011) Brunisolic soils of Canada: Genesis, distribution, and classification. *Canadian Journal of Soil Science*, 91, 695-717.
- Sparks, D. L. (2003) *Environmental soil chemistry*, 2nd ed., Elsevier Science & Technology Books.
- Theng, B.K., and Yuan, G. (2008) Nanoparticles in the soil environment. *Elements*, 4, 395-399.
- Villinski, J. E., O'Day, P. A., Corley, T. L., and Conklin, M. H. (2001) In situ spectroscopic and solution analyses of the reductive dissolution of MnO₂ by Fe (II). *Environmental Science & Technology*, 35, 1157-1163.
- Weaver, R.M., and Hochella, M.F. (2003) The reactivity of seven Mn-oxides with Cr³⁺aq: A comparative analysis of a complex, environmentally important redox reaction. *American Mineralogist*, 88, 2016-2027
- Zachara, J. M., Girvin, D. C., Schmidt, R. L., and Resch, C. T. (1987) Chromate adsorption on amorphous iron oxyhydroxide in the presence of major groundwater ions. *Environmental Science & Technology*, 21, 589-594.

FIGURE CAPTIONS

FIGURE 1. Topographic map of California with the location of the Mum and Alice June claims indicated with a red dot.

FIGURE 2. (a) SEM-BSE and (b) SEM-EDS chemical distribution map for Si (blue), Cr (green) and Mg (red) of an intergrowth between brucite and quartz in the sample from the Mum and Alice June claims (M31456).

FIGURE 3. (a) TEM image of clinocllore fibers (chl) in a microtome section cut from a clinocllore-brucite-quartz-chromite assemblage; the location of the thinner area shown in (b) and (c) is indicated with a white square; (b) TEM and (c) STEM-EDS chemical distribution map for Mg (red) and Cr (green) of an area within a clinocllore fiber containing chromite nanoparticles; (d) high-resolution TEM image and (e) FFT pattern of a selected area within the area shown in (b) and (c); the FFT pattern indicates characteristic lattice fringes for chromite with d-spacings of 2.1 Å (400).

FIGURE 4. (a) SEM-BSE image of an etched clinocllore grain (chl) after leaching of a silicateenriched chromitite powder with a solution of pH = 5; (b) STEM and (c) STEM-EDS chemical distribution maps for Cr (green), Fe (red) of an Al-rich colloid in the leachate of pH = 5, for clarity reason, a chemical distribution map for only Si (red) and Al (blue) is shown as an inset; (d) high resolution TEM image of the chromite nanoparticles on the surface of the Al-rich colloid with characteristic lattice fringes of chromite with d-spacings of 2.1 Å (400) and 2.9 Å (220).

FIGURE 5. Synthesized chromite (chr) nanoparticles used in the batch experiments: (a) TEM image and (b) STEM-EDS chemical distribution map for Fe (red) and Cr (green) of an aggregate of synthesized chromite nanoparticles, the area shown in (c) is indicated with a rectangle; (c) high-resolution TEM image and (d) FFT pattern of a selected area within the aggregate; the FFT pattern indicate that the lattice fringes in (c) have characteristic d-spacings for chromite; (e) powder-diffraction pattern of the synthesized chromite nanoparticles depicting broad peaks with d-spacings similar to those observed in the FFT pattern.

FIGURE 6. (a) STEM image and b) STEM-EDS chemical distribution map for Cr (green), Mn (blue) and P (red) of an aggregate of hausmannite (Hsm), chromite (Chr) and manganite nanoparticles in a suspension without chamosite and organic matter.

FIGURE 7. Chemical composition of chromite, hausmannite nanoparticles and chamosite particles after the long-term experiments: Ternary plots depicting (a)-(b) Cr : Mn : Fe ratios in (a) altered chromite nanoparticles (blue) in comparison to the ideal stoichiometry of an unaltered chromite (red); (b) altered hausmannite nanoparticles; (c) the Al : Mg : Fe ratio in altered chamosite grains (black) in comparison to the ideal stoichiometry of an unaltered chamosite (red).

FIGURE 8. (a) STEM image and (b)-(d) STEM-EDS chemical maps for (b) Fe (red) and Cr (green), (c) Fe (red) and Mn (blue) and (d) Mn (blue) and Si (yellow) of an aggregate containing two hausmannite (Hsm) and the remains of a chromite (Chr) nanoparticle.

FIGURE 9. (a) STEM image of an aggregate of hausmannite (Hsm) and chromite (chr) nanoparticles, the area shown in (b)-(d) is indicated with a rectangle; (b) STEM image (c) STEM-EDS chemical map for Fe (red), Cr(green) and Mn (blue) and (d) high resolution TEM image of the area depicted in (a); etch features and a rim of a Fe-(hydr)oxide are indicated with arrows.

FIGURE 10. (a) TEM image and (b)-(c) STEM-EDS chemical maps for (b) Fe (red) and Cr (green) and (c) Fe (red) and Mn (blue) of an aggregate of chromite nanoparticles (chr) with an Cr-(hydr)oxide precipitate containing two parallel rods of bracewellite rods (γ -CrO(OH)); (d) STEM image and (e) STEM-EDS chemical distribution map for Fe (red), Cr (green), Mn (blue), Si (yellow) of an aggregate containing hausmannite nanoparticles (hsm), an unidentified clay mineral and the remains of a chromite nanoparticle with two rods of bracewellite (γ -CrO(OH)); the area shown in (f) is indicated with a rectangle in (e); (c) TEM image of two rods of bracewellite.

FIGURE 11. (a) STEM image and (b) STEM-EDS chemical map for Fe (green), Cr (red) and Mn (pink) of a chamosite grain from with attached Cr-(hydr)oxides and hausmannite

nanoparticles; the areas shown in (c) and (d-e) are indicated with rectangles in (b); (c) STEM image of hausmannite nanoparticles attached to the chamosite grain; (d) TEM image and (e) high-resolution TEM image of a Cr-(hydr)oxide grain attached to a chamosite grain, the area shown in (e) is indicated with a rectangle in (d); a FFT pattern (inlet) indicates that the lattice fringes in (e) have characteristic d-spacings of grimaldiite (α -CrO(OH)); (f) STEM image of chromite nanoparticle aggregates (chr) attached to a larger organic matter colloid (OM); aggregate 1 is composed of weakly-altered chromite nanoparticles whereas aggregate 2 is highly altered and is depleted in Fe and enriched in Mn relative to aggregate 1 (see supplementary data).

TABLE 1. Characterized chromitite ore samples, the location and type of their respective ore deposit and the hosts and concentrations of Cr in the ore (excluding chromite)

Sample ID	Location of ore deposit	Type of chromite ore deposit	Host of Cr/chromite nanoparticles	Range of Cr concentrations in hosts
M31456	Mum and Alice June claim, California	Ophiolite	Brucite, $Mg(OH)_2$	1-4 at%
M31456	Mum and Alice June claim, California	Ophiolite	Clinochlore $Mg_5Al(AlSi_3O_{10})(OH)_8$	0.5-2 at%
M29852	Asbestos, Quebec	Ultramafic intrusion	Lizardite, $Mg_3Si_2O_5(OH)_4$	< 0.5 at%
M7560	Black lake, Quebec	Ultramafic intrusion	Lizardite, $Mg_3Si_2O_5(OH)_4$	< 0.5 at%
M41446	Crushed Stone Newfoundland	Ophiolite	Lizardite, $Mg_3Si_2O_5(OH)_4$	<0.9 at%
M9431	Lewis Hill, Newfoundland	Ophiolite	Lizardite, $Mg_0.3Si_2O_5(OH)_4$	<0.2 at%
Sample from Schindler et al. 2017	Black Thor deposit “Ring of Fire”	Ultramafic intrusion	Clinochlore, $Mg_5Al(AlSi_3O_{10})(OH)_8$	1-3 at%
Sample from Schindler et al. 2017	Mistake Mine, Fresno, California	Ophiolite	Lizardite $Mg_3Si_2O_5(OH)_4$	1 at%
		Ophiolite	Clinochlore $Mg_5Al(AlSi_3O_{10})(OH)_8$	3 at%
Sample from Schindler et al. 2017	Mistake Mine, Fresno, California		$Mg_5Al(AlSi_3O_{10})(OH)_8$	

TABLE 2. Chromium-, Fe- and Mn- concentrations in the suspensions (pH = 5) after the 9 months batch experiments (detection limits for Cr, Cr⁶⁺, Fe, Mn = 0.2, 0.5, 50, 50 and 1.0 [μgkg⁻¹]); the solutions were filtered (450 nm filter) but not centrifuged; Cr = chromite nanoparticles, Mn = hausmannite nanoparticles, Si = 10 gr chamosite, or = 10 gr organic rich soil; bdl = below detection limit

Experiment	Eh [V]	Cr [mgkg⁻¹]	Cr⁶⁺ [μgkg⁻¹]	Fe [mgkg⁻¹]	Mn [mgkg⁻¹]	P [mgkg⁻¹]
1: Cr-Mn = 1 : 1	0.43	0.0200	0.6	Bdl	19.11	2.903
2: Cr-Mn = 1 : 5	0.40	0.0028	<0.5	Bdl	15.66	4.681
3: Cr-Mn = 1 : 1, Si	0.41	0.0008	4.0	0.07	8.74	0.157
4: Cr-Mn = 1 : 5, Si	0.41	0.0014	4.1	Bdl	7.57	3.321
5: Cr-Mn = 1 : 1, Or	0.42	0.0300	0.6	0.01	25.40	0.125
6: Cr-Mn = 1 : 5, Or	0.43	0.0264	0.9	Bdl	38.32	0.040